ELECTRICAL CHARACTERIZATION OF ION-IMPLANTED 4H-SILICON CARBIDE

THESIS

Christian P. Morath, 2nd Lieutenant, USAF
AFIT/GAP/ENP/99M-05

DEPARTMENT OF THE AIR FORCE
AIR UNIVERSITY
AIR FORCE INSTITUTE OF TECHNOLOGY

Wright-Patterson Air Force Base, Ohio

DISTRIBUTION STATEMENT

DISTRIBUTION STATEMENT A
Approved for Public Release
Distribution Unlimited

AFIT/GAP/ENP/99M-05

ELECTRICAL CHARACTERIZATION OF ION-IMPLANTED 4H-SILICON CARBIDE

THESIS

Presented to the Faculty of the Graduate School of Engineering
of the Air Force Institute of Technology
Air University
In Partial Fulfillment of the Requirements for the
Degree of Master of Science in Engineering Physics

Christian P. Morath, B.S.
2nd Lieutenant, USAF

March 1999

AFIT/GAP/ENP/99M-05

ELECTRICAL CHARACTERIZATION OF ION-IMPLANTED 4H-SILICON CARBIDE

Christian P. Morath, B.S.
2nd Lieutenant, USAF

Approved:

Yung Kee Yeo — 10 March 1999

Yung Kee Yeo — date
Professor of Physics
Chairman, Advisory Committee

R L Hengehold — 10 Mar 99

Robert L. Hengehold — date
Professor of Physics
Member, Advisory Committee

10 March 1999

David E. Weeks — date
Assistant Professor of Physics
Member, Advisory Committee

Acknowledgments

I would like to express my sincere appreciation to my faculty advisor, Dr. Yung Kee Yeo, for his guidance and support throughout the course of this thesis effort. His insight, experience, and keen sense of humor were certainly appreciated, and his enjoyment of solid state physics served as a source of inspiration for me choosing this research. I would also like to thank my committee members Dr. Robert L. Hengehold and Dr. David E. Weeks.

I must also thank Dr. Mohamed Ahoujja. Without him, the research would not have been possible. His persistence, methodology, and love for doing "haree-research" have touched me. I consider him the source of my inspiration for continuing my studies in physics.

The AFIT laboratory staff deserves my thanks as well. Special thanks goes to Belinda Johnson, who was of great help to me, fixing this and that, and showing me the correct way to do things in a clean room. Her patience with my clumsiness is deeply appreciated. Greg Smith gets my thanks for always being available to find things.

Some thanks must be passed along to Pepsi-Cola Inc. whose fine products I have subsisted on during this research, no doubt at the expense of a significant increase in the duration of my next visit to the dentist.

Above all, I would like to thank my family and friends whose support has kept my spirit from drying up during these past several months. All the phone calls reporting imminent snowfalls were greatly appreciated. Moreover, special thanks to my girlfriend, Stephanie, whom I will always respect and admire, and who always goes out of her way to be nice.

And lastly, I guess I should say thank you to my first high school physics teacher, Mrs. Lisa Martone, who peaked my curiosity in physics early on and whom I generally consider to be a great human being.

Christian P. Morath

Table of Contents

List of Tables

List of Figures

Abstract

Electrical characterization has been performed on p-type 4H-SiC implanted with Al or B to assess the activation efficiency and implantation-related damage recrystallization. The electrical technique of Temperature Dependent Hall Effect (TDHE) indicated that Al and B act as shallow acceptors in 4H-SiC with ionization energies of ~ 252 and ~ 285 meV, respectively. However, the deeper B level (600 meV) was not observed. Measurements of the electrically active concentration of most samples indicated electrical activation efficiency much greater than 100% for anneal temperatures of 1550 °C, 1650 °C, and 1750 °C. The samples used were low doped ($N_A - N_D = 5x10^{15}$ cm^{-3}) epitaxial p-type layers grown by MOCVD. They were implanted at room and high temperature (500 °C). The p-layer was grown on low doped epitaxial n-type material to electrically isolate it. The n-type layer was in turn grown on heavily doped n-type substrate material. To help in forming good ohmic contacts, the samples had a high fluence shallow implantation (Al 50 keV) done on the samples' corners. The shallow implantation was not as successful in this capacity as it was hoped, because good ohmic contacts could not be easily formed on the samples. The shallow implantation was also done over a significant portion of the sample surface area (~ 67%), which may be the reason for measuring such high activation efficiency. The other measurement problem was that because of shorting the p-n junction formed by the two epitaxial layers may not have fully isolated the p-layer from the n-layer. On three samples it was observed that after contact annealing at 1150 °C for 5 min Al contact metal penetrated through the1.3 μm p-layer by diffusion, allowing n-type conduction to occur. Room temperature Hall measurements were also done at several currents to characterize the effects of the poor contacts, and it was found that the average percent errors in the concentration measurements for Al and B implanted samples were ~26% and ~ 24%, respectively. The optimum anneal temperature for Al and B implanted samples was found to be ~ 1650 °C and ~ 1550°C, respectively. The implantation dose resulting in the highest concentration for Al and B implantation was found to be $3x10^{13}$ cm^{-2}. Increased annealing temperatures were demonstrated to increase mobility and the primary scattering mechanism was ionized impurity scattering. A peak mobility

of ~ 200 cm^2 / V s was measured for an Al implanted sample; this is considerably higher than the peak mobility for the B implanted samples, ~ 100 cm^2 / V s. No significant gains in transport properties were evident with high temperature implantation (500 °C) compared to the room temperature implantation. Overall, Al implantation of 4H-SiC appears superior with regard to these properties compared to B implantation.

I. Introduction

I-1. Background

The present state of technology and electronics has been fostered by years of research in the field of semiconductors. In recent years the need for high temperature electronics has driven the economic forces to shift the aim of research towards semiconductor material with wide bandgaps like silicon carbide (SiC). SiC can operate at higher temperature, higher frequency, and higher power than conventional semiconductors. With these capabilities SiC will direct electronic technology down new paths and into new domains. A full understanding of the fundamental electronic properties of SiC and semiconductors in general is required, however, before this journey begins, and that begins back in the early 1800s.

Early Semiconductor Research

The study of semiconductors is marked by several important discoveries, all of which have occurred in the last 200 years. In 1833, Michael Faraday discovered the semiconducting properties of silver sulfide (Ag_2S) when he observed it had a negative temperature coefficient of resistance [1:122]. Working independently, Braun and Schuster first observed rectification or non-linear junction behavior in galena (PbS), and pyrites and copper oxides, respectively [2:556,3:251]. This material capability is now fundamental to modern solid state devices.

Further major discoveries in solid state electronic devices would have to wait until after substantial progress in the field of quantum mechanics, which provided some theoretical foundation for understanding semiconductor phenomenon, was made. This work would lead to the most famous discovery in solid state electronics, the point contact transistor, by Brattain, Bardeen, Shockley, and others at Bell Laboratories in 1948 [4:230,5:232,6:233].

Theoretical Framework

The theoretical foundation of semiconductor physics itself resides on the use of quantum mechanics. In 1930, Wilson answered the question of conduction in a

semiconductor [7:458]. He showed that while both the tightly bound core electrons and the bonding valence electrons are free to move unimpeded through the crystal and cannot be associated with a single lattice atom, only certain electrons take part in conduction. Wilson introduced the concepts of unoccupied and filled or partially filled bands. Bands of quantum states separated by a bandgap, a region with no energy states, result by application of a periodic potential to the free electron states in the Sommerfield model. Wilson is also attributed with the idea for doping, introducing of a small concentration of a specific chemical species into a semiconductor, so electron states form within the bandgap and precise control of the conductivity is possible. This idea is the basis for all modern electronic devices.

Modern Solid State Devices

Although several semiconducting materials had already been discovered, silicon (Si) became the dominant material for the infant device industry because early on successful growth and purification techniques were developed. Further refinement has led to an industry where electronics can be produced with high reproducible yields and excellent reliability at low cost. Practically all integrated circuit (IC) and discrete device technology is now based on silicon.

The market for other semiconducting materials began growing after it was realized that Si was a limited material technology. For instance, Si's electrical properties prohibited an efficient Si-based light emitting diode (LED) from being realized. Failures for Si technology led to the development of compound semiconductor materials like GaAs and GaP. Spreading economic interest led to new semiconductors being developed for use in LED's, solid state lasers, photovoltaic arrays, and sensors and emitters at different wavelengths. Now, a growing interest exists in building electronic devices that function at high temperature, high frequency, and high power and unlike existing semiconductors, are not easily susceptible to chemical damage. This has focused research on to wide-bandgap semiconducting materials such as SiC.

SiC Development

SiC was one of the first semiconductors to be discovered. Berzelius first theorized chemical bonding between silicon and carbon in a paper he published in 1824. Despite this, it was not until 1891 that SiC growth was first accomplished and verified by Eugen Acheson [8:25]. Acheson was melting carbon and aluminum silicate, when he discovered blue crystals forming near the carbon rod. Thinking the crystals to be a compound of carbon and aluminum, he named the new compound Carborundum, a name that has remained synonymous with SiC.

In 1907, a SiC LED was realized by Round [8:25]. Additional early success with SiC led Shockley himself, the inventor of the bipolar junction transistor, to prophesize at the First International Conference on SiC in 1959 that it would be the material of choice for high temperature operation [8:25]. It was not until 1990 that high-quality SiC substrates finally became commercially available. Since then SiC technology and device processing has rapidly advanced, and demonstrations of complex digital and analog integrated circuits, random-access-memories, and charge-coupled devices have all been realized [9:42].

I-2. High Temperature High Power Electronics

Conventional semiconductors like Si and Ge cannot adequately perform in high-temperature, high-power, and/or high-radiation conditions, and they have low resistance to caustic chemicals. A need for electronic devices that can operate in such environments has arisen and created a surge of activity in wide bandgap semiconductors. High temperature circuit operation ranging from 350 °C to 500 °C is desired for use in aerospace applications (turbine engines and the more electric aircraft initiative), nuclear power instrumentation, satellites, space exploration, and geothermal wells [10:1409]. A majority of DOD/DOE space and terrestrial military applications have requirements for electronic systems to operate at temperatures up to 500 °C and beyond [11]. The real motivation for studying this material comes from the hope that SiC electronic devices can replace more costly and complex systems in use today in commercial and military capacities.

Commercial Interest

It is expected that significant improvements in a wide-ranging variety of capacities are possible with the use of SiC electronic devices [12]. Significant energy savings in public electric power distribution and electric vehicles could be achieved using SiC devices for high-voltage switching. SiC devices would also make for more powerful microwave electronics for radar and communications sensors and controls for cleaner-burning more fuel-efficient jet aircraft and automobile engines [13:598]. SiC's properties could also be exploited on space vehicles, where high temperature rated and radiation resistant electronics would allow for less space shielding and heat radiators. This could reduce system sizes and liftoff weights. These examples show that an investment in research on wide bandgap semiconductors could lead to an enormous commercial and military return.

Air Force Interest

Modern electronics have given the United States Air Force the most sophisticated and functional avionics systems in the world; thus, the Air Force has an interest in advancing semiconductor technology [14:6]. As part of their More Electric Aircraft (MEA), initiative the U.S. Air Force and Navy envision replacing bulky aircraft hydraulics and mechanical control systems with heat tolerant *in situ* control electronics. The statistics from fighter aircraft studies have shown that a conversion to the electric power concept would result in higher reliability, maintainability and supportability, and would substantially reduce overall costs [15,16].

The MEA initiative would include powering subsystems such as hydraulic-driven flight control actuators, engine-gearbox driven fuel pumps, and air-driven environmental control systems electrically via electric motors. Additional elements being considered in this initiative are shown in Figure I-1 [17:I-11].

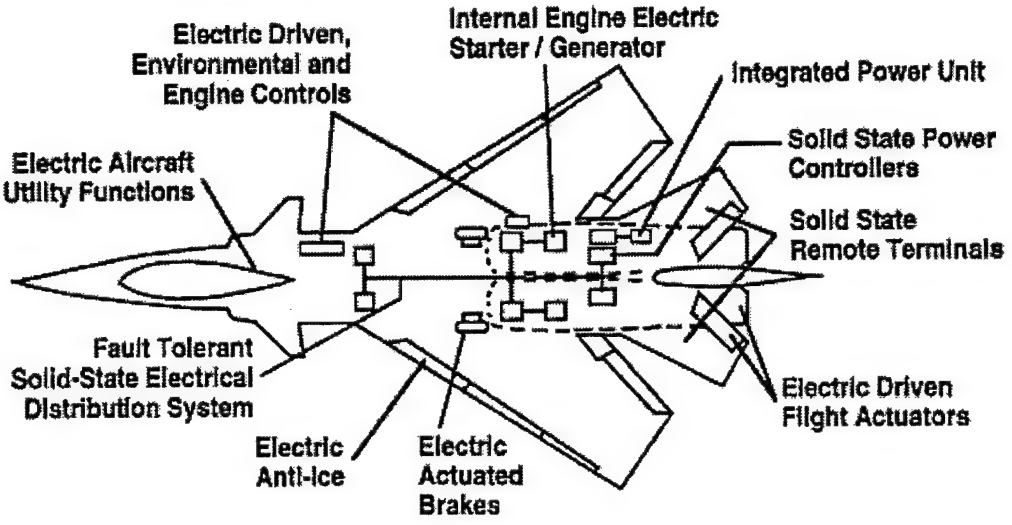

Figure I-1. Visionary concept for the configuration of the more electric aircraft, showing the hydraulic driven subsystems being considered for conversion to electric motor driven actuation.

A major concern with the MEA approach and the removal of the hydraulic systems is the concurrent removal of the active cooling system. The current military standard rating for the junction temperature of conventional Si-based electronic devices is to operate over a range from –55 °C to 125 °C; removing the hydraulic systems from aircraft will increase operating temperatures to 350 °C. The best solution to this problem is the use of higher temperature rated electronics. The Propulsion and Power Directorate at the Wright Laboratory, WPAFB, considers SiC to be the best candidate for use in this capacity [14:6].

Problem Statement

SiC technology has been advancing for the past thirty years, but for progress to continue an efficient means for selective p-type doping is required for the fabrication of planar electronic devices. Ion-implantation is an attractive means for doping SiC because it has small diffusion coefficients and SiC's physical hardness lends itself well to implantation and the subsequent high temperature thermal annealing which is required for activating the implanted ions. 4H-SiC is just one of an infinite number of SiC polytypes, but its properties, current state of device processing technology, and widespread commercial availability make it the most attractive candidate, of all the SiC

polytypes, for use in high temperature electronics. 4H-SiC's crystal structure is in actuality 50% hexagonal, 50% cubic, and this gives 4H-SiC a much less anisotropic mobility compared to 6H-SiC. 3C-SiC is the only pure cubic SiC polytype, but it is significantly behind 4H-SiC in terms of processing technology and availability.

This study is an electrical characterization of ion-implanted p-type 4H-SiC to find the optimum parameters for an ion-implantation and thermal annealing scheme. The electrical characterization will be done using temperature dependent resistivity and Hall effect measurements. The characterization is intended to show the activation efficiency and transport properties' dependence on the implanted ion, Al or B, implantation dose, implantation temperature, and annealing temperature.

Scope

Through this study, the optimum ion implantation/annealing parameters will be found. The main questions this research seeks to answer are:

1) Does the implantation and annealing scheme used for these samples work to produce quality p-type 4H-SiC?

2) What are the optimum implantation/annealing procedure parameters, given that the scheme works?

3) What is the doping concentration and mobility that can be achieved for Al and B implantation?

4) What metals/procedure formed the best ohmic contacts for low doped 4H-SiC p-type epilayers?

Thesis Organization

This thesis is divided in to five chapters. This chapter serves to introduce the reader to the present state of conventional semiconductor and SiC technology. The problem studied in this research is also introduced. In the second chapter, the relevant

theory for the research is developed, and the results of a thorough literature review are listed. The experimental equipment and the test procedures used to take data are discussed in the third chapter. The fourth chapter examines the experimental results, and also contains the data analysis. Chapter five summarizes the results and gives some recommendations for future research.

II. Theory

II-1. Wide Bandgap Semiconductors

Wide bandgap semiconductors are given that distinction because they have relatively much larger bandgaps (~ 2.2 to 6 eV). Some of the premier or more widely researched wide bandgap semiconductors include silicon carbide (SiC), aluminum nitride (AlN), gallium nitride (GaN), boron nitride (BN), diamond, and zinc selenium (ZnSe). In general, wide bandgap semiconductors have excellent thermal conductivities, large breakdown fields, and good resistance to chemical attacks. This resistance is partly attributable to the large cohesive energy of the compound. The other material properties are mainly attributed to the electronic band structure of the material.

A semiconductor's band structure is critically dependent on the valency of the atom or molecule and the interatomic spacing of the crystal lattice, as shown in Figure II-1 [18:377]. As the diagram shows, when the distance between atoms is on the order of the radii of the atom's outer shell, the discrete electron levels of the outer shell are broadened into groups or bands; the effect on the inner levels is minimal. Whether the material acts a conductor or insulator depends on the occupancy of the highest occupied band at $T = 0\ K$. If the highest occupied band is completely filled, the material will act as an insulator or a semiconductor; if it is partially filled, it will act like a conductor. The empty region between the highest occupied and lowest unoccupied bands is called a bandgap. A material's overall band structure is reflected in the material's electrical and optical properties, and by measuring these properties, it can be determined.

The occupancy of the bands will depend on the semiconductor's constituent atoms or molecules. Solids having four valence electrons will have their highest occupied band completely filled. A completely filled highest band also occurs in several compound materials. There is no clear measure to distinguishing between semiconductors and insulators because in some temperature regions a semiconductor will act like a very good insulator and in others, it may act like a good conductor. For practical purposes semiconductors have smaller bandgaps, and this allows for electrons to be thermally excited in to the next higher band where conduction can occur.

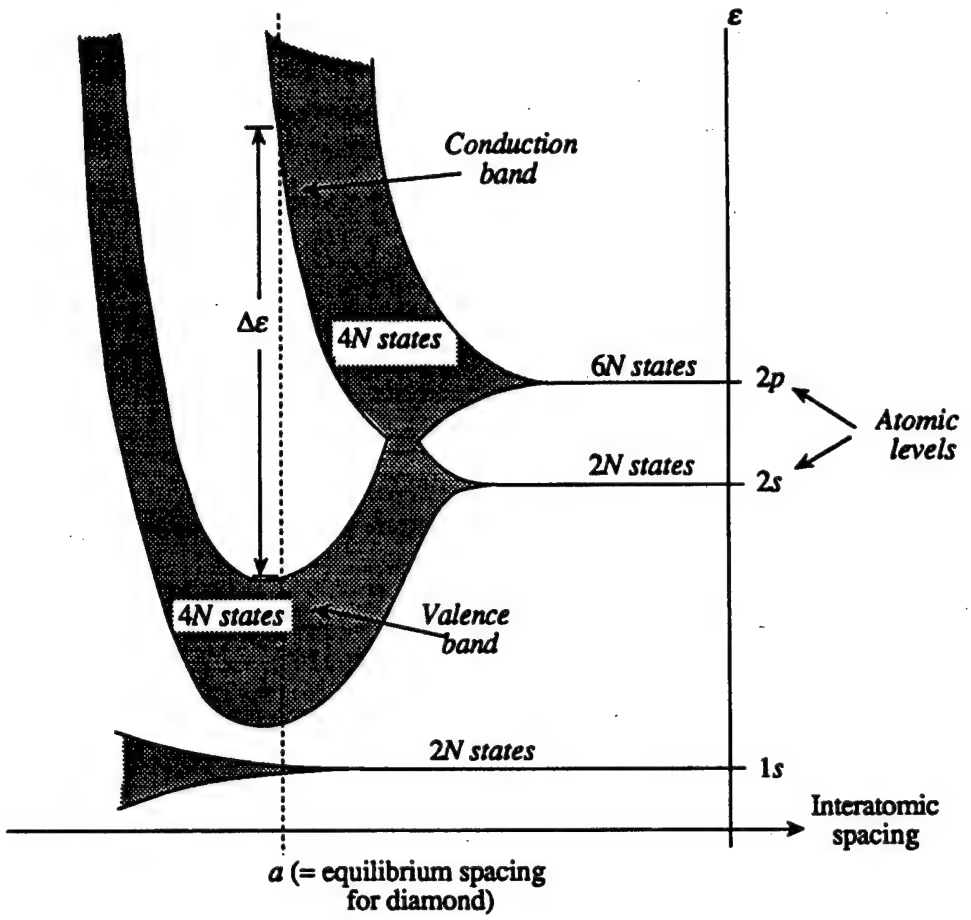

Figure II-1. Diagram showing the relation between the interatomic spacing and the spreading of the energy levels for a lattice atom. Levels become discrete in the limit of infinite interatomic spacing.

Intrinsic Conduction

Two types of conduction are possible, intrinsic and extrinsic. Intrinsic conduction occurs when electrons in the highest filled band, the valence band, are thermally excited across the bandgap in to the empty band, the conduction band. The "holes," empty electron states, left by the excited electrons will also conduct, but have properties similar to positive charges. Thermal statistics, impurities, and the bandgap or activation energy, E_G, dictate the number of available carriers. In agreement with Faraday's discovery, the carrier concentration increases with temperature, as does conduction.

The carrier concentrations are strictly determined using Fermi statistics from the number of available states and the Fermi energy, which is dependent on the impurity

concentration in the material. The Boltzmann approximation can be used to simplify the Fermi relations for the hole and electron concentrations when the following conditions on the Fermi energy are satisfied

$$E_c - E_f >> kT \tag{1}$$

$$E_f - E_v >> kT. \tag{2}$$

Materials obeying conditions (1) and (2) are described as "non-degenerate" semiconductors; for these cases, we may approximate the Fermi relations for hole and electron carrier concentrations by the following expressions respectively

$$p = N_v \exp\left(\frac{E_v - E_f}{kT}\right) \tag{3}$$

$$n = N_c \exp\left(\frac{E_f - E_c}{kT}\right), \tag{4}$$

where E_f is the Fermi energy, T is the temperature, k is Boltzmann's constant, and N_c and N_v are the density of states in the conduction and valence band, respectively. N_c and N_v are calculated from the electron and hole effective masses, m_n^* and m_p^*, respectively, and temperature by the following expressions

$$N_c = 2M_c\left(\frac{2\pi m_n^* kT}{h^2}\right)^{3/2} \tag{5}$$

$$N_v = 2\left(\frac{2\pi m_h^* kT}{h^2}\right)^{3/2}. \tag{6}$$

In Eq.(5), M_c refers to the number of conduction band minima in the first Brillouin zone and h is Planck's constant. The effective mass are found by cyclotron resonance measurements or calculated by theoretical means. For 4H-SiC, the density of states hole effective mass, $m_{p,ds}(T)$, has been calculated to be ~ 3.52 m_o in the high temperature limit, where m_o is the rest mass of an electron [19:122]. The full temperature dependence is shown in Figure II-2.

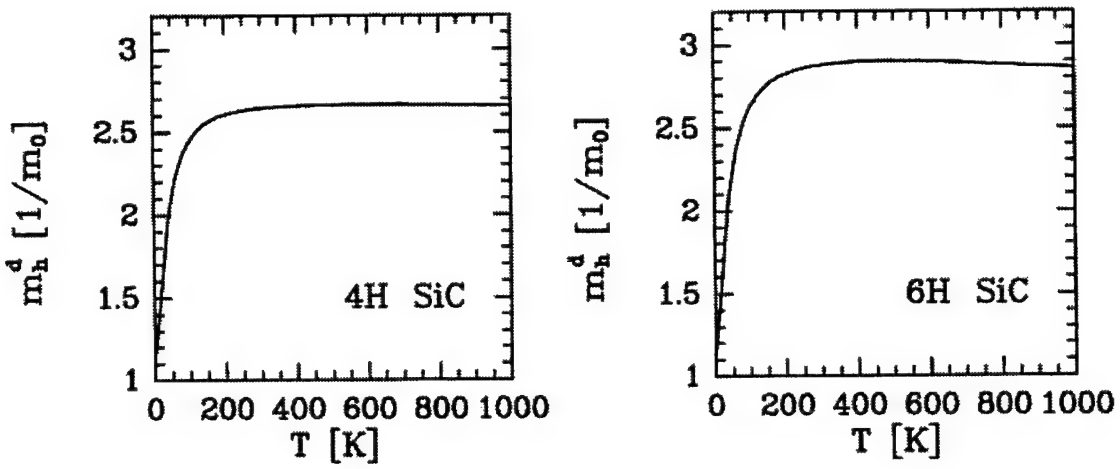

Figure II-2. Calculated hole effective mass in 4H- and 6H-SiC by Rossler and Wellenhofer [19:107].

In the case of pure semiconductors, the conduction is primarily intrinsic. In intrinsic conduction, the number of conduction electrons equals the number of valence holes. Applying this fact, an analytic expression for the ideal intrinsic free-carrier concentration, $n_i^2 = (p\ n)$, can be found from equations (3) and (4) to give

$$n_i^2 = (N_c N_v) \exp\left(\frac{-E_G}{k T}\right). \tag{7}$$

Using Eq.(7)the Fermi energy for intrinsic conduction can be expressed as

$$E_{fi} = E_v + \frac{1}{2} E_g + \frac{1}{2} k T \ln\left[\frac{m_h^*}{m_n^*}\right], \tag{8}$$

which asserts that at $T = 0$ the Fermi energy is in the middle of the bandgap, and does not wander far from it as temperature increases. Thus, when kT is small compared to E_g, and it generally is for semiconductors at room temperature and below, the Fermi energy is far from the boundaries of the bandgap, E_c and E_v, and so conditions (1) and (2) are usually satisfied.

Extrinsic Conduction

Extrinsic conduction occurs in semiconductor materials doped with impurities, either intentionally or unintentionally. Doping the material allows for some control of conduction and for the conduction to occur at much lower temperatures than by intrinsic

means. Dopant atoms have different structure than the lattice atoms, and thus spoil the periodicity of the lattice. These "defects" in the lattice are reflected in the band structure by electronic levels forming within the bandgap. Where the levels occur within the bandgap depends on the atomic structure of the dopant and the lattice. When the impurity levels form close to either of the band edges, only small activation energies are required for conduction to occur. These shallow impurities will either "donate" or "accept" electrons depending on whether they are close to the conduction band or the valence band.

For a type IV semiconductor like Si, type III materials, aluminum and boron for instance, have one less electron and act as acceptors when they occupy Si lattice sites. Nitrogen and phosphorous, both type V materials with one extra electron, act as donors, when they occupy Si lattice sites. In SiC, the situation is more complicated because of the lattice polytypic arrangement and the lattice constituents' molecular structure.

Although only a full quantum mechanical treatment will suffice for finding exact solutions, the question of why the dopants have levels within the bandgap can be partly answered by understanding the following a simple example [20:579]. Consider the donor atom to be just a lattice atom with an additional fixed positive charge, along with an additional electron. If this atom were in empty space, the binding energy of the electron would just be the first ionization energy of the impurity atom, but since the atom is surrounded by the lattice, the binding energy is significantly reduced. This occurs because of two reasons: (1) the impurity atom's field of charge is altered by the static dielectric constant, ε, of the semiconductor which is rather large, and (2) electrons moving in a semiconductor are not described by a free space energy-momentum relation, but by a conduction band energy-momentum relation. This difference is accounted for by replacing the electron mass in the expressions for electron motion with an effective mass, m^*. Thus, an electron in the presence of a donor impurity with charge e, within the medium of the semiconductor, is represented by as a particle of charge $-e$ and mass m^*, moving in free space in the presence of an attractive center of charge e / ε.

The impurity atom problem is now reduced to a simple hydrogen atom, but with binding energy that accounts for the presence of the lattice. Calculating the new binding energy requires replacing the product of the nuclear and electronic charges, e^2, by e^2 / ε,

and the electron's mass, m by m^*. These impurities form levels beneath the conduction or above the valence band because the impurities' binding energies are measured relative to the bottom and top of those bands, respectively. This situation of just two opposite charges is an ideal scenario; any number of different kinds of charge centers can form in a semiconductor. Each charge center will also have excited levels associated with it. Look has derived an expression for the occupancy, $n_{k\,l\,m}$, of the mth excited level of the lth charge state of kth center as

$$n_{klm} = \frac{N_k}{1 + \sum_{l,m' \neq l,m} \left(\frac{g_{k\,l'\,m'}}{g_{k\,l\,m}}\right) \exp\left(\frac{(E_{k\,l'\,m'} - E_{k\,l\,m} - (l - l')\,E_f)}{kT}\right)}, \tag{9}$$

where N_k is the total concentration of the type k centers, $g_{k\,l\,m}$ and E_{klm} are the degeneracy and energy of the (klm) state, respectively [21:244]. The unknown in this expression, E_f, is determined by the requirement for charge neutrality. The total positive and negative charges are given by

$$\text{positive charge} = p + \sum_{k,l=0,m}^{l=l_{D\,k}} (l_{Dk} - l)\, n_{klm} \tag{10}$$

$$\text{negative charge} = n + \sum_{k,l=l_{D\,k},m}^{l=l_{D\,k}+l_{A\,k}} (l - l_{Dk})\, n_{klm}, \tag{11}$$

where the kth center has $l_{D\,k}$ donor levels and $l_{A\,k}$ acceptor levels, and p and n are the free hole and electron concentrations respectively. Equating the total positive and negative charges gives

$$n = p + \sum_{k,l=0,m}^{l=l_{D\,k}+l_{A\,k}} (l_{Dk} - l)\, n_{klm}. \tag{12}$$

This expression simplifies in the typical case of a dominant donor or acceptor species with a single charge state and no excited states in the band gap. What is implied by "dominant" center is that the position of the Fermi level, E_f, is controlled by this center, and remains near the dominant center and a few kT away from every other center at all temperatures. For a dominant donor, if the center's energy level is a few kT below E_f,

this dominant center is occupied with electrons and centers above E_f are not occupied. Equation (12) reduces for the case of a dominant donor of concentration N_D to

$$n + N_A^{\text{net}} = \frac{N_D}{1 + \frac{n}{\Phi_D}}, \tag{13}$$

where

$$\Phi_D = \frac{g_{D0}}{g_{D1}} N_C \exp\left(\frac{-E_D}{kT}\right) \tag{14}$$

$$= \frac{g_{D0}}{g_{D1}} N_c' \exp\left(\frac{-\alpha_D}{k}\right) T^{3/2} \exp\left(\frac{-E_{D0}}{kT}\right). \tag{15}$$

In Eq. (15), g_{D0} and g_{D1} are the degeneracy of the occupied and unoccupied states respectively. The donor activation energy has a linear dependence on the temperature of the form $E_D = E_{D0} - \alpha_D T$, where E_{D0} is the donor energy as $T \rightarrow 0$. N_a^{net} is a term representing the charge of all other centers, donor or acceptor centers either above or below E_F, that are temperature-independent. Thus, it is given by

$$N_A^{\text{net}} = \sum_{k, E_{Ak} < E_F} N_{Ak} - \sum_{k, E_{Dk} > E_F} N_{Dk}. \tag{16}$$

For p-type samples, a similar expression for dominant acceptor center is found from equation (12), which in this limit reduces to

$$p + N_D^{\text{net}} = \frac{N_A}{1 + \frac{p}{\Phi_A}}, \tag{17}$$

where

$$\Phi_A = \frac{g_{A1}}{g_{A0}} N_V' \exp\left(\frac{-\alpha_A}{k}\right) T^{3/2} \exp\left(\frac{-E_{A0}}{kT}\right) \tag{18}$$

and N_D^{net} is given by

$$N_D^{\text{net}} = \sum_{k, E_{Dk} < E_F} N_{Dk} - \sum_{k, E_{Ak} > E_F} N_{Ak}. \tag{19}$$

In this case, g_{A1} and g_{A0} are the degeneracy of the occupied and unoccupied states, respectively. N_D^{net} is the total concentration of other charge centers, similar to (16). The

acceptor activation energy is also assumed to have linear temperature dependence. It is given by $E_A = E_{A0} - \alpha_A T$, where E_{A0} is the acceptor energy as $T \rightarrow 0$. Examining equations (13) and (17), one can see that by measuring the temperature-dependent carrier concentration, the donor or acceptor activation energy can be determined by a fitting the proper equation to the data.

Wide Bandgap Semiconductors

Materials are generally classified as insulators or semiconductors according to the magnitude of their bandgap energy, E_g. For pure materials, the range of activation energies for classification is roughly taken as $0 < E_g < 2$ electron volts (eV) for semiconductors and 2 eV $< E_g$ for insulators. Wide bandgap semiconductors form a third material classification. They have bandgap energies ranging from 2.2 eV to over 6 eV.

The magnitude of the bandgap is understood to be critically dependent on the interatomic spacing and the valency of the material. All wide-bandgap semiconductors are molecular structures, with the exception of the diamond crystal structure of carbon (C). The cohesive energy of the molecular structures are responsible for several intrinsic properties; these include physical hardness, radiation hardness, large heterojunction offsets, high charge carrier velocity, low dielectric constants, and high thermal conductivity.

It is these properties that make wide bandgap semiconductors attractive for use in electronic devices. The large bandgap does, however, add several complications. The fabrication of bulk volume perfect crystals has the additional constraints of lattice ordering and phase equilibria control of a binary system undergoing transitions between gaseous, liquid and solid phases. Additional complications arise with contact metal adhesion, device processing/fabrication, and doping of these materials.

II-2. SiC

SiC for high-power, high-temperature electronics

SiC has physical, electrical and optical properties which make it attractive for use in high-temperature and high-power applications. These include a high electron saturation velocity, wide bandgap, and high thermal conductivity. Table II-1 is a

comparison of the properties of SiC and other popular semiconductor device technologies [22:1365]. The large thermal conductivity, breakdown voltages, and saturation velocities of SiC, GaN, and diamond should be noted. The maximum operating temperature is arbitrarily chosen to be the temperature at which the intrinsic carrier concentration equals $5x10^{15}$ cm^{-3}.

Table II-1. Comparison of important properties for selected semiconductors.

Property	*Si*	*GaAs*	*GaP*	*4H-SiC*	*GaN*	*Diamond*
E_g (eV) at 300 K	1.12	1.42	2.3	3.26	3.39	5.5
Maximum Operating Temperature (°C)	327	487	977	1200	-	1150
Melting Point (°C)	1417	1237	1467	Sublimes T>1827	-	Phase Change
Physical Stability	Good	Fair	Fair	Excellent	Good	Very Good
Electron Mobility at 300 K (cm^2 / V s)	1400	8500	350	800	900	1600
Hole Mobility at 300 K (cm^2 / V s)	600	400	100	40	1600	150
Breakdown Voltage, E_b, (10^6 V / cm)	.25	.3	-	2.2	5	10
Thermal Conductivity, σ_T, (W / cm)	1.5	.5	.8	3.4	1.3	20
Saturated e^- Drift Velocity, v_s, (10^7 cm / sec)	1	1	-	2	2.7	2.7
Dielectric Constant, κ	11.8	12.8	11.1	9.7	9	5.5

Crystal Structure and Nomenclature

SiC exhibits a 1-D polymorphism called polytypism. Polymorphism is the ability of a chemical compound to exist in more than one crystalline form. Polytypism is a specific kind of polymorphism where the substance crystallizes so two dimensions of the unit cells of the numerous modifications are equivalent, but they differ in the a third variable dimension. The variation in the third unit cell dimension is an integral multiple of the spacing between successive layers, and depends on the number of layers in the structure.

In the case of SiC, modifications are created by bilayers of Si and C bonded tetrahedrally and being stacked upon each other in different orders. The individual bond lengths and local atomic environments are nearly identical. The differences between modifications are only noticeable in the third or higher nearest neighbor arrangements. The bonding between adjacent layers is either of a zinc-blende (cubic) or wurtzite (hexagonal) nature. As shown in Figure II-3 the zinc-blende bonds are rotated 60° with respect to nearest neighbors [22:1366].

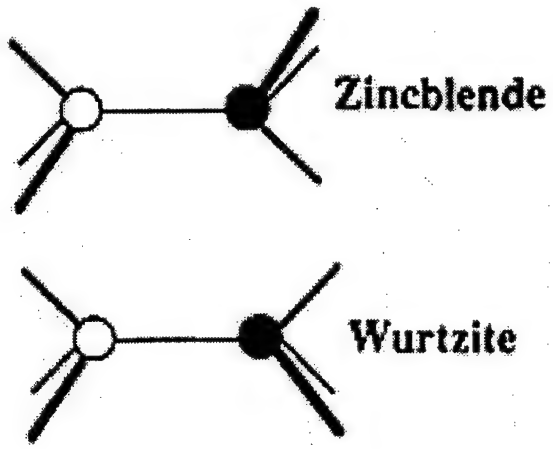

Figure II-3. Diagram of the zinc-blende and wurtzite crystal bonding structure. The zinc-blende bonds are rotated 60° with respect to nearest neighbors.

Because the zinc-blende bonds differ from the wurtzite bonds, some lattice sites in polytypes with mixed bonding schemes are inequivalent. These issues become important when considering the substitutional impurity incorporation and the electronic transport properties. The stacking sequence of the 4H-SiC polytype is shown in Figure II-4 [23:25]. The diagrams show two different approaches to understanding how the stacking occurs. The close packing of the atomic layers is given in diagram (a), where each sphere represents a Si-C pair. Taking the ground layer to be A-type, the next layer will have spheres occupying the three C or B positions surrounding each A sphere. Stacking continues in this manner, and by alternating the relative positions of successive layers periodically, each polytype is defined. Diagram (b) shows the actual atomic positions for an arbitrary SiC polytype. The polytype is arbitrary because another layer is needed to define it. If the stacking pattern defined here, AB, is continued the 2H polytype would be defined.

There are three systems of nomenclature used for SiC. The ABC notation describes the stacking modifications by giving the labels A, B, and C arbitrarily to the three SiC bilayer positions with respect to the lattice. Jagodzinski notation labels all the atomic sites in close packings with either cubic (k) or hexagonal (h) point symmetry. The system replaces the A, B, or C layer with h or k. The third system is the Ramsdell notation, *4H-SiC*. This label includes the compound of interest, SiC, the number of layers in the stacking sequence, four, and the symmetry of the space group characterizing the crystal, hexagonal [24:64]. 4H-SiC is in actuality 50% hexagonal, 50% cubic. Figure II-5 shows a schematic illustration of the crystal structure of four SiC polytypes using the Ramsdell zigzag notation. The usefulness of the Ramsdell notation is apparent because it incorporates the data of the other notation systems as well. The schematic also shows that the SiC polytypes can have inequivalent lattice sites; therefore, in 4H-SiC the possibility exists for two different donor sites and two different acceptor sites for a particular substitutional impurity to form.

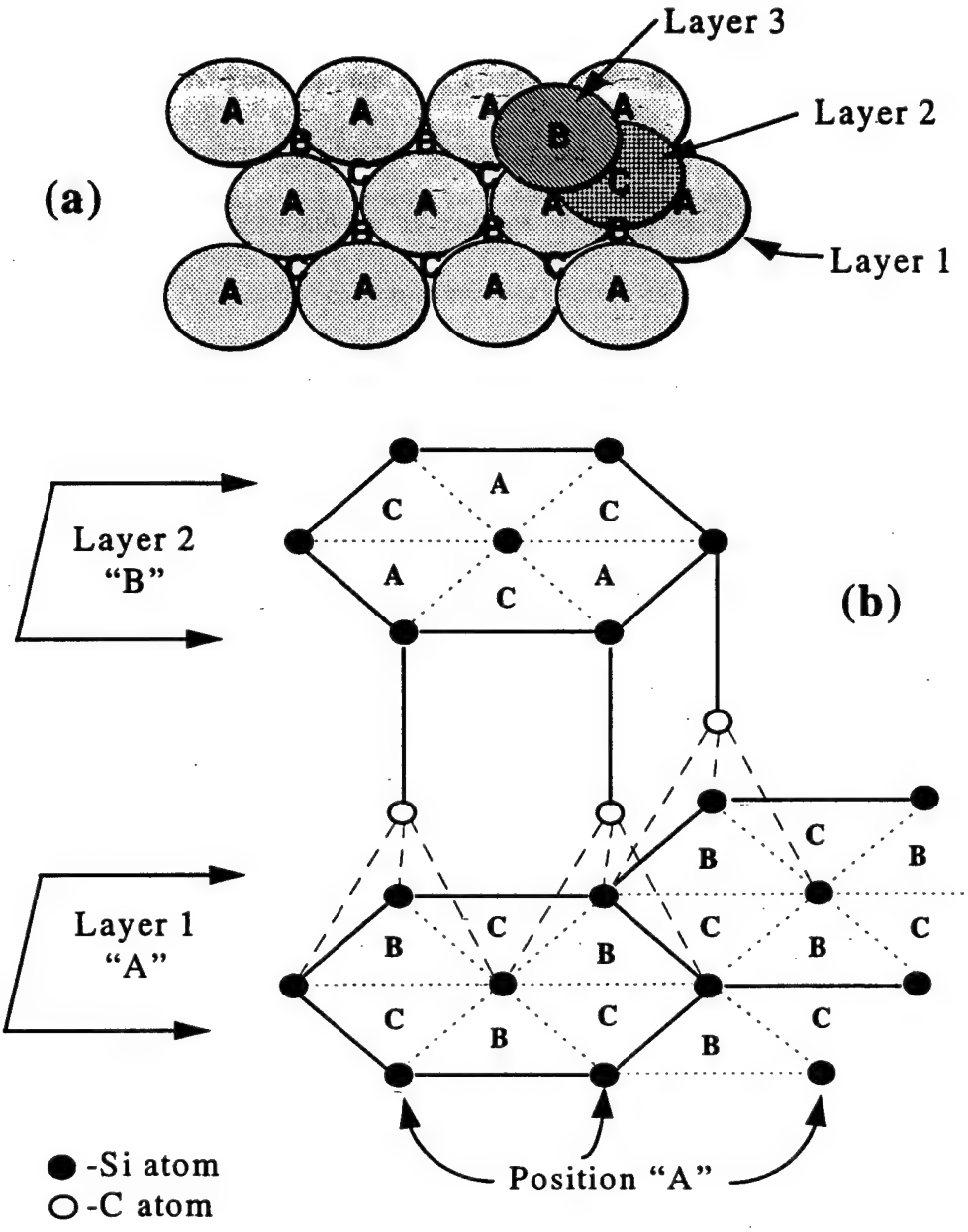

Figure II-4. Diagrams of the stacking sequence of SiC. Diagram (a) is spherical representation of the close packing positions. Ground layer, A-type, spheres have six voids, three of which are filled by next layer, B-type or C-type. In (b), the actual atomic positions are shown for an arbitrary SiC polytype.

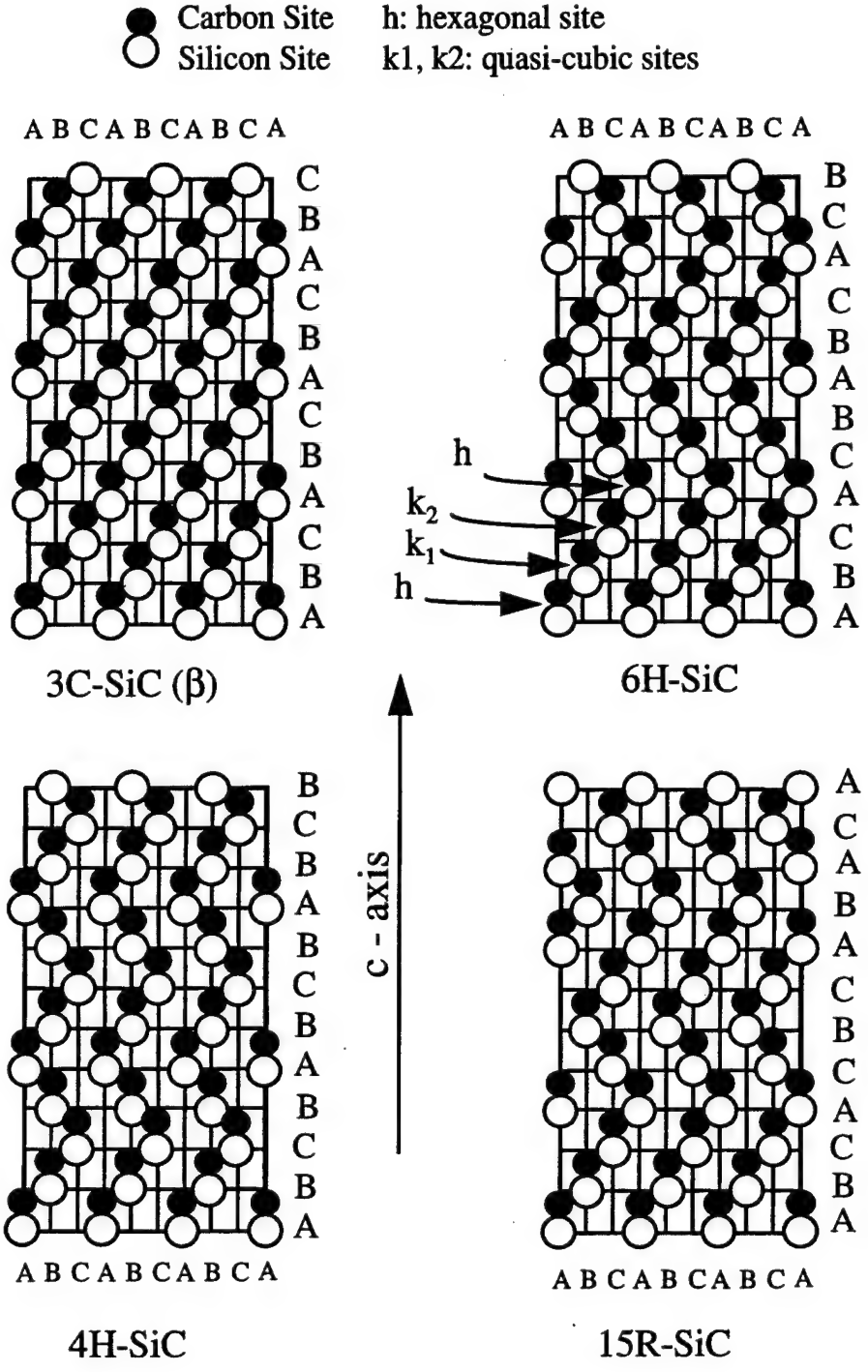

Figure II-5. Crystal structures of 4 SiC polytypes (3C-SiC, 4H-SiC, 6H-SiC, and 15R-SiC) in the Ramsdell zigzag notation. The ABC notational stacking sequence and the Jagodzinski labels are also depicted. The sites labeled *k* and *h* are the cubic and hexagonal sites, respectively. In the 6H-SiC diagram, k_1 and k_2 label the two inequivalent cubic positions.

SiC Growth

SiC substrate growth has recently been improved to the point where an established, commercialized process for the growth of high-quality substrate material exists. The 4H-SiC samples used in this research are epitaxial layers grown by molecular beam epitaxy (MBE) on substrate material grown by modified sublimation. The samples were purchased from Cree Research.

Molecular beam epitaxial growth is a technique where molecular beams are employed to deposit different atomic species in a well-controlled manner on a substrate material. Evaporation or the sublimation of heated solid or liquid sources in crucibles produces the molecular beams. The flux is governed by the vapor pressure of the material in the cell, which typically has an Arrhenius-type dependence on temperature, $\phi = \phi_o \exp (-E_A / k T)$ [25:58]. This simple behavior is what allows for the growth control and the extremely ordered layers. Epitaxial layers have much higher Hall mobility than bulk material. Figure II-6 shows a typical molecular beam epitaxy setup. The crucibles in which source material is placed are known a Knudsen cells. The crucibles have small recessed orifices where sources are maintained at a desired temperature using a temperature controller and a thermocouple sensor.

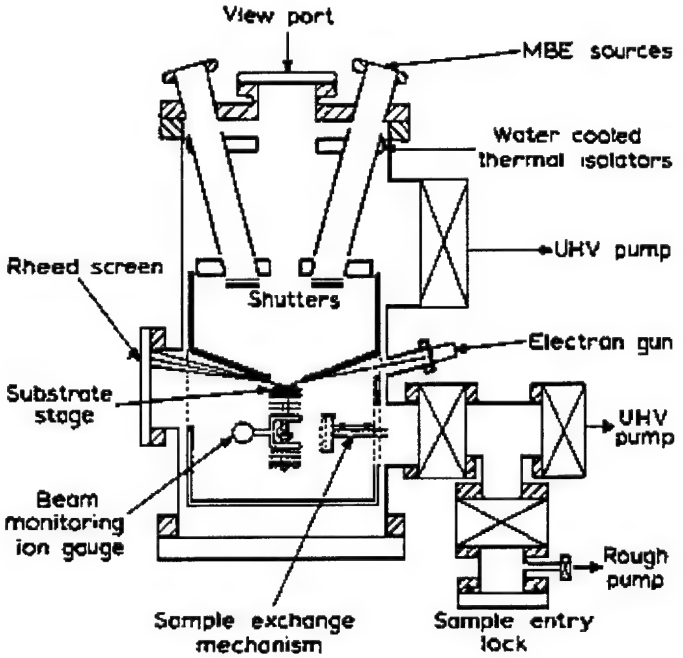

Figure II-6. A typical molecular beam epitaxy apparatus.

The samples' substrate material is grown by modified sublimation. In sublimation growth, SiC is evaporated beneath a SiC seed crystal held at a lower temperature. The growth rate is proportional to, and the crystallization process is facilitated by, supersaturation of the vapor phase [26:30]. A crystal's quality is a function of the seed surface quality, absorption variations due to seed doping, SiC-source material properties including source structure, polytype, and particle strain. Figure II-7 demonstrates the modified sublimation growth technique. The figure depicts the temperature gradient within the chamber.

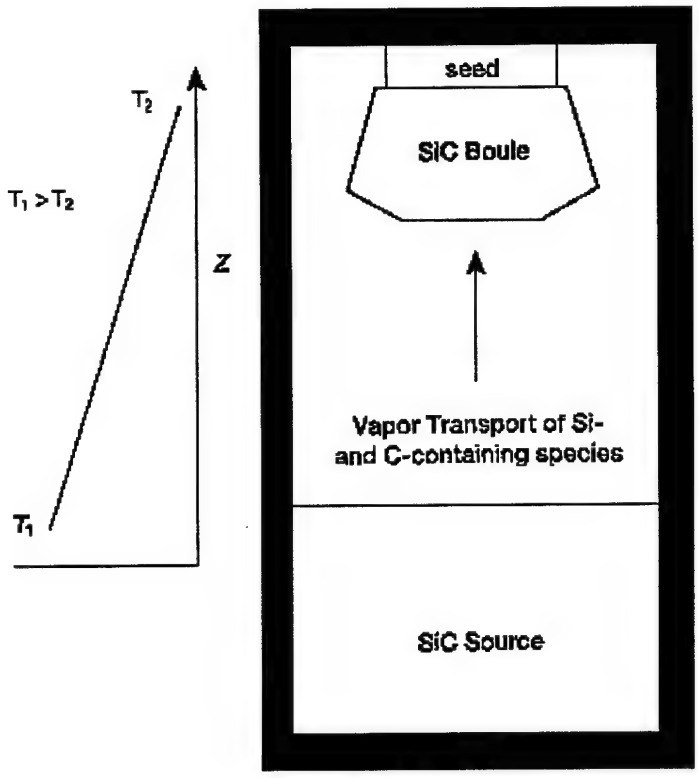

Figure II-7. Diagram of the modified sublimation growth technique. Note that the temperature gradient within the chamber is being depicted.

The primary growth defects for SiC are micropipes, small-diameter (~ .1 – 5 μm) hole that may extend through the entire boule along the growth direction, with typical densities ranging from 10 - 10^3 cm^{-2}. Neudeck and Powell have confirmed that micropipes inhibit high voltage operation for SiC devices by observing the failure of high-voltage diodes in reverse bias caused by microplasmas generated in the micropipes [27:63]. In addition to formation during growth, there is also micropipe dissociation,

migration, transformation, and recombination, which reduce micropipe concentration. Other growth defects that occur in modified sublimation are mosaic structural variations, dislocations, inclusions and striations. It has been proposed that mosaic structural variations are related to micropipe formation.

II-3. Ohmic Contacts

The formation of ohmic contacts on the semiconductor surface is required for Hall effect measurements. Ohmic contacts are defined as electrical connections between a semiconductor and a metal, which have a linear current – voltage (I - V) relationships [28:581]. In general, metal-semiconductor combinations are rectifying, not ohmic, upon preparation. This rectification is due to the Schottky barrier at the metal-semiconductor interface, and these types of contacts are called Schottky contacts. Schottky contacts have asymmetric I - V characteristics similar to a p-n junction diode.

The interaction of moving electrons, or current, and the Schottky barrier at the metal-semiconductor interface is what ultimately determines the contact's rectification properties. There exist three possible mechanisms that can account for current passing across the interface: field emission, thermionic-field emission, and thermionic emission. The paths the electrons follow in each case are shown in Figure II-8.

There currently is no simple, self-consistent, comprehensive model for the formation of Schottky barriers on semiconductor surfaces [29:549]. There are, however, several important factors that influence the Schottky barrier height (SBH), one being the difference between the work functions of the metal and the semiconductor. For contacts on p-type SiC, there is no known metal with a workfunction equivalent to the material's electron affinity plus the Fermi level of the semiconductor (~ 6 eV) [30:1414]. The resulting barrier at the interface causes a depletion region of holes to occur; this region must be small for the contact to be ohmic. An example depicting this region is shown in Figure II-9.

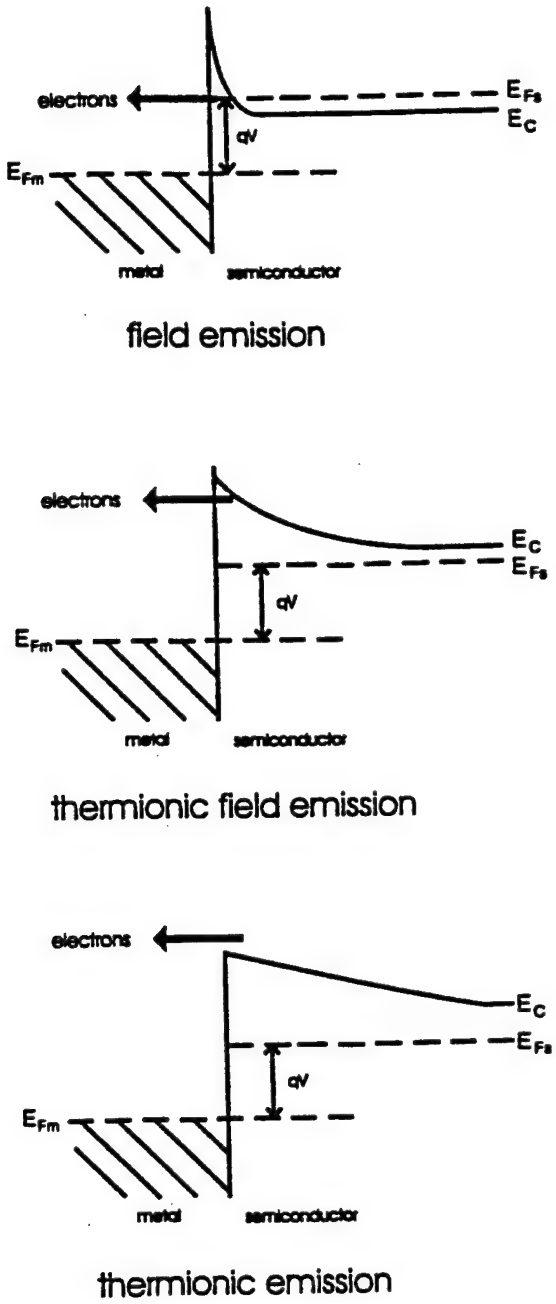

Figure II-8. Energy band diagrams depicting field emission, thermionic field emission, and thermionic emission for an n-type semiconductor. Field emission occurs when the barrier is sufficiently thin to allowing tunneling to occur.

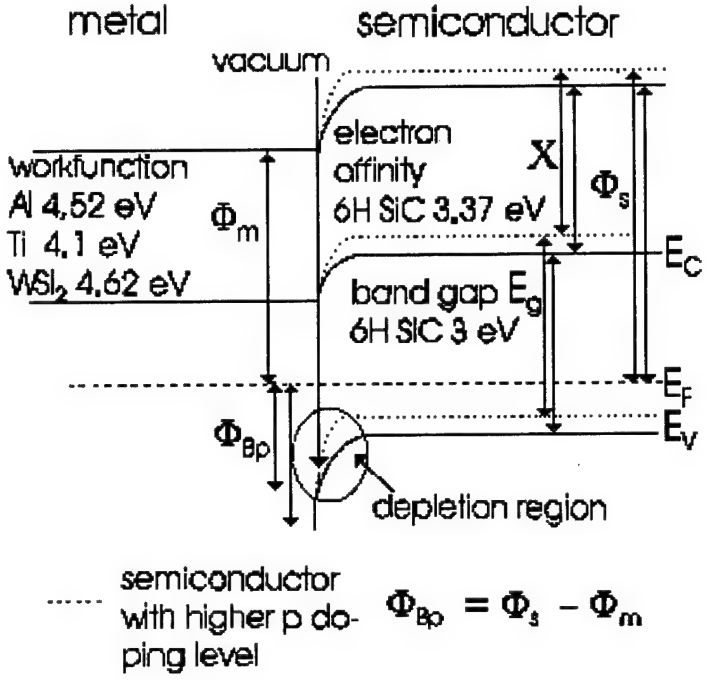

Figure II-9. Theoretical models for band bending at a metal-p-semiconductor interface (6H-SiC). The workfunctions of typical contact metals and the 6H-SiC electron affinity, χ, and bandgap, E_g, are listed. For 4H-SiC, χ is also ~ 3.3 eV, E_g is slightly larger, ~ 3.3 eV.

The depletion region may be decreased in size by very shallow p-dopant implantation [30:1414]. A smaller depletion region allows for field or thermionic-field emission to occur. It can be shown that the specific-contact resistance is proportional to the barrier height divided by the dopant concentration or

$$r_c \propto \exp\left[\frac{\phi_B}{\sqrt{N}}\right]. \tag{20}$$

Equation (20) above approximates the following expression, which gives the full dependence of contact resistance on the hole concentration

$$\frac{1}{r_c} = \frac{4\pi m q^2}{h^3} \int_0^\infty \frac{T(E)}{1 + \exp\left(\frac{E-E_f}{kT}\right)} \, dE, \tag{21}$$

where $T(E)$ is the tunneling probability for electrons through the barrier.

The ion implantation for reducing specific contact resistance to 10^{-3} Ω–cm^2 (T = 300 K; ϕ_{Bp} = 0.4 eV) must result in a hole concentrations more than 10^{19} cm^{-3}

[31:1414]. Ion implantation of 4H-SiC, as discussed in the next section, has many of its own associated difficulties. For instance, implantation above a critical dose ($1x10^{15}$ cm^{-2} for Al ions at 300 K at 50 keV) will result in amorphous regions that cannot be recrystallized by annealing at temperatures up to 1700 °C [31:879]. It should be noted that these numbers indicate that for good contacts to be formed implantation above the critical fluence for amorphization is required [32,2026].

Acceptable contact resistance's on moderately or lightly doped material has still not yet been demonstrated [28:600]. Selective doping for forming ohmic contacts by ion implantation is a potential solution but accurately controlling the p-type doping in the contact regions is still a problem. Annealing above 1500 °C causes spreading of the profile and depletion of the implanted species by evaporation from the surface (observed for temperatures above 1700 °C) [28:600]. Hot implantation for selective doping in the contact regions could solve this problem because the *in-situ* annealing that occurs with hot implantation has been reported in some cases to reduce the lattice damage caused by implantation.

II-4. Ion Implantation and Annealing Studies

For this study, 4H-SiC samples will be implanted with various ions (Al or B) at different fluences ($1x10^{13}$ cm^{-2}, $3x10^{13}$ cm^{-2}, and $1x10^{14}$ cm^{-2}). Sample implantation will be done at room and elevated temperatures (500 °C).

Implantation

Ion implantation is a process where highly energetic dopant atoms are injected into the semiconductor. The process of implantation begins with ionizing the source of dopant atoms using an electron beam. Then, the ionized atoms are passed through a mass spectrometer to select out the desired impurities. The impurities are further screened out by slits that form the front of an acceleration tube. Once in the tube, ions can be accelerated to the desired implantation energy. The doping density and depth distribution are controlled by ions mass, velocity, and particle flux. Implantation is more directional than diffusion, and therefore there is control over the profile. Figure II-10 below shows a typical implantation apparatus [25:54].

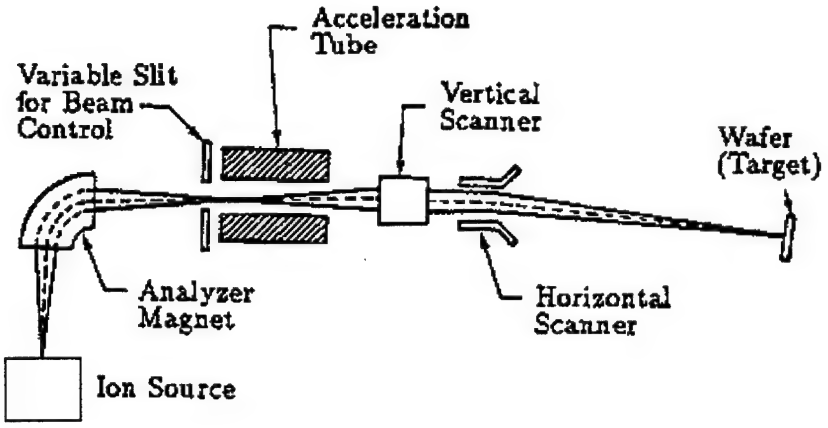

Figure II-10. Typical ion implantation apparatus.

The difficulty of implantation comes with the defects generated when the ion is injected into the solid and loses energy by nuclear collisions and coulumbic interactions with the target nuclei. The nuclear stopping power is the dominant energy dissipating mechanism for the incoming atoms. The nuclei are displaced from the lattice sites as the ions come to rest and occasionally a cascade of displacements is initiated. The question of reducing implantation defects by high temperature implantation was under debate, but recent evidence is indicating that no gains in reducing scattering centers are made by hot implantation up to 700 °C [33:289]. Implantation at higher temperatures (~ 1000 °C) may still prove beneficial.

Several different possible defects can occur from implantation including vacancies, impurities, and interstitials. It is accepted knowledge that after implantation the implanted atoms predominantly occupy interstitial lattice sites where they are rarely electrically active [34,2479]. In addition, implantation of heavier atoms is more likely to result in amorphous regions, where the crystal structure is completely destroyed, compared to light atom implantation. It has been determined that for room temperature implantation the critical fluence for heavy Al atoms is reached at ~ 10^{15} cm^{-2}. The amorphous zones produced by such high dose implantation are found to be stable even up to anneals at 1700 °C. The typical defects resulting from heavy and light ion implantation are shown in Figure II-11 [25:54].

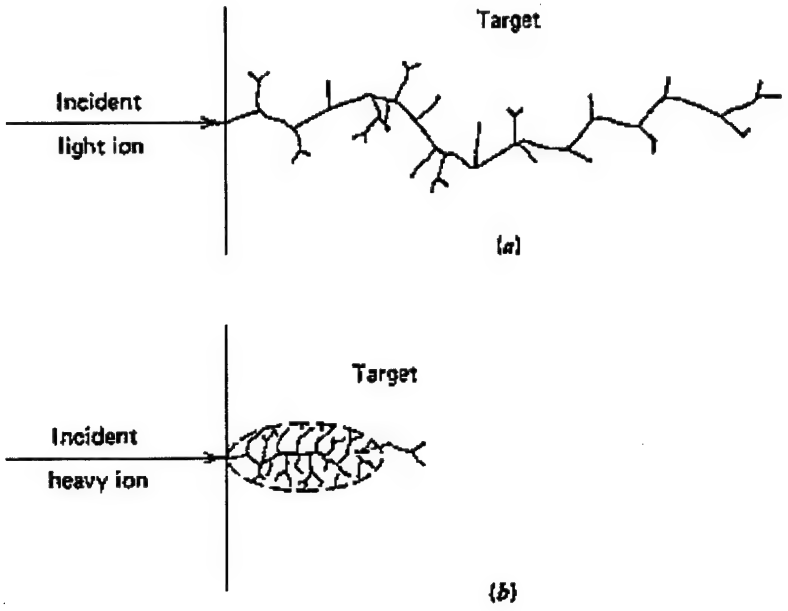

Figure II-11. Defects resulting from implantation of heavy and light atoms.

The crystalline defects produced by implantation need to be annealed in order to activate the doped atoms and reduce the lattice damage because even low concentrations of defects can have significant effects on electrical properties such as minority carrier lifetime and mobility. Annealing activates the doped atoms and reduces the lattice damage because the heating causes the amorphous material to regain its crystalline order, by inducing a phase transition within the material.

In this study, Al and B implanted samples will be analyzed. The Al and B ionization energies in 4H-SiC are reported to be the following [33:278], [35:270]:

$\Delta E(Al)$ = 191 to 280 meV

$\Delta E(B)$ = 285 to 390 meV.

A deeper B level, known as the D-center, was also found and reported to be the following:

ΔE(D-center) = 580 meV.

It has been conjectured that the D-center includes a B atom occupying a carbon site next to an empty lattice site. It has not been completely determined whether D-center behaves like a donor or an acceptor. In this study, it was observed that the ionization energy decreased with increasing acceptor or increased compensation concentration.

It was also determined that dopants can occupy either the hexagonal or cubic sites in the more complex SiC polytypes, and by studying the relative abundance of the various N dopant levels, a correspondence was made to the ratio of available binding sites [34: 264]. The implantation of 4H-SiC with n-type dopants has shown that the ionization energy is dependent on which site, the hexagonal or cubic, the dopant atom occupies. The ionization energies of Al and B acceptors are only weakly sensitive to the particular polytype and to inequivalent lattice sites.

Annealing

The implanted samples used in this study will be annealed at temperatures ranging from 1550 to 1750 °C. Implanted semiconductors are annealed to repair the damage caused by the ion implantation and activate the implanted ions. Annealing occurs when a phase transition is induced causing the semiconductor to become recrystallized. The recrystallization restores the material order, and newly implanted ions become part of the lattice. This is what activating the implanted atoms inside the crystal means; the impurity atoms occupy the former position of one of the semiconductor's constituent atoms. The success or failure of annealing depends on the following parameters: the semiconductor material, the dopant, and means of introduction into the semiconductor, and the annealing conditions. For SiC, the multitude of modifications complicates the annealing process because several structurally stable states (polytypes) exist.

For this study, thermal annealing was done to anneal the samples. In thermal annealing, samples are heated in a furnace to temperatures ranging from 1000 to 1800 °C in an Ar atmosphere. The main limitation on thermal annealing is the possibility for dissociating or destroying the semiconductor surface. This problem can be alleviated by placing the material within some kind of crucible of similar material during the annealing which increases the partial pressure of the constituent semiconductor atoms within the furnace chamber. The Ar atmosphere also helps decrease surface evaporation since the inert Ar does not react with the material and takes the place of other possible impurities. For device processing, thermal annealing is also limited since the entire device will be annealed at once and for some applications this is undesirable.

Ion Implantation Studies

The practicalities of ion implantation include the ion ranges and distributions, ion-induced damage, surface passivation, post-implantation annealing, and characterization of implanted layers. The distribution of implanted ions depends on the orientation of the substrate during the implantation and the energy given to the implanted atoms. The calculated ranges for Al, B, and Ga implantation in to 4H-SiC are shown in Figure II-12

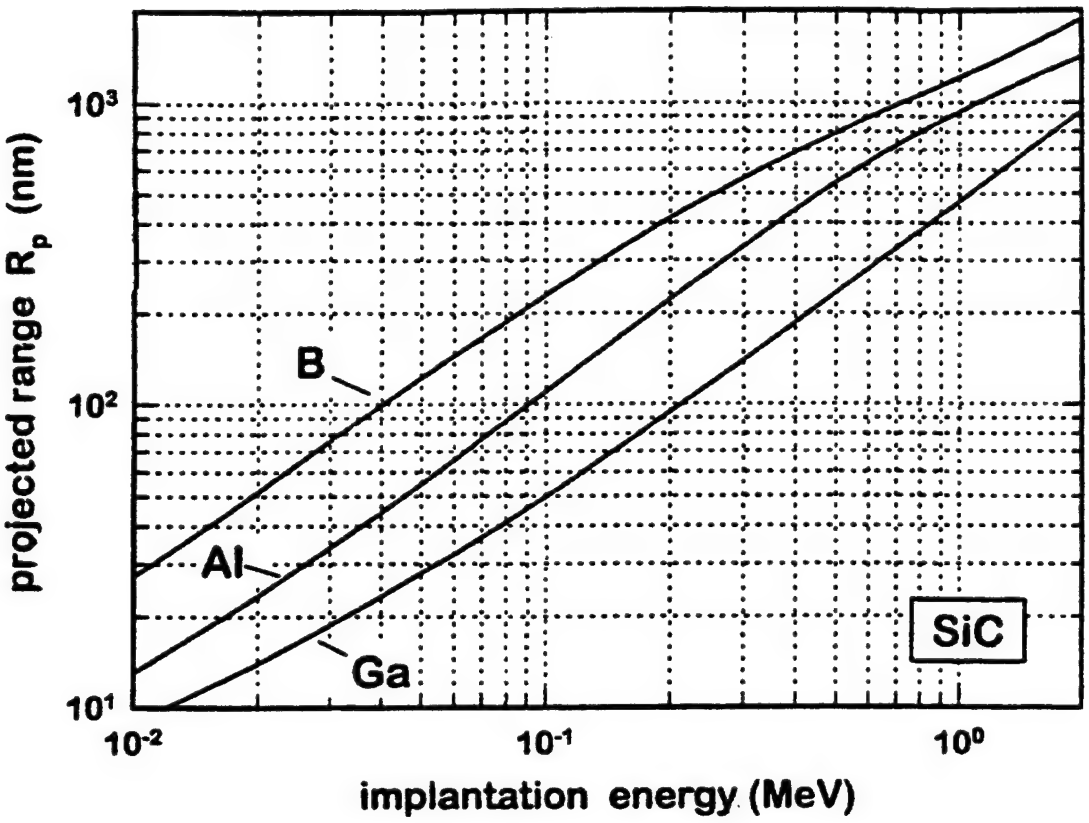

Figure II-12. Calculated ranges, R_p, for implanted B, Al, and Ga ions into SiC as a function of the implantation energy. As the ion size increases the implantation depth decreases [33:280].

To minimize the amount of channeling, the process where the incident beam is aligned with one of the major crystal axes and ions penetrate to depths far greater than predicted for amorphous targets, the samples must be intentionally misalign. The radiation damage caused by the ion implantation is found to depend on dose and dose rate, and appears as zones of amorphization. Because of this difficulty high temperature implantation has been attempted. Implantation at high temperatures (> 1700 °C) has been found to alleviate the forming of amorphous layers [36,237].

Although annealing the implanted samples was found to activate the impurity ions, the high temperature anneal was also found to cause diffusion of the impurity atoms. Therefore, annealing changes the implantation profile. When diffusion is occurring, a good means to characterize ion-implanted materials is to look at the electrical properties of the different layers, which can be accomplished by doing a series of Hall measurements, and etching thin layers off between each measurement. This will give information about the carrier concentration and the mobility profiles in the implanted regions. The diagram in Figure II-13 shows the results of an analysis of the change in the doping profile of B and Al implanted atoms subsequent to a high temperature anneal (1700 °C for 30 min).

Restoring Structure of Ion-implanted SiC

Research on annealing of SiC has already been conducted for several decades. A group of researchers at the V.I. Ulyanov Institute in Leningrad were among the first to look at restoring silicon carbide structures after ion implantation [37:960]. They deduced that for thermal annealing (TA) of 6H-SiC, the TA temperature, implantation dose, and nature of the implanted impurity all have significant influence on the restoration of the structure. The following fundamentals were also illustrated upon experiment:

1) Relative structural perfection increased with annealing temperature.
2) Number of defects and the required thermal annealing temperature rose with increased doses.
3) Implantation ions generating greater mechanical stress require an increased thermal annealing temperature.

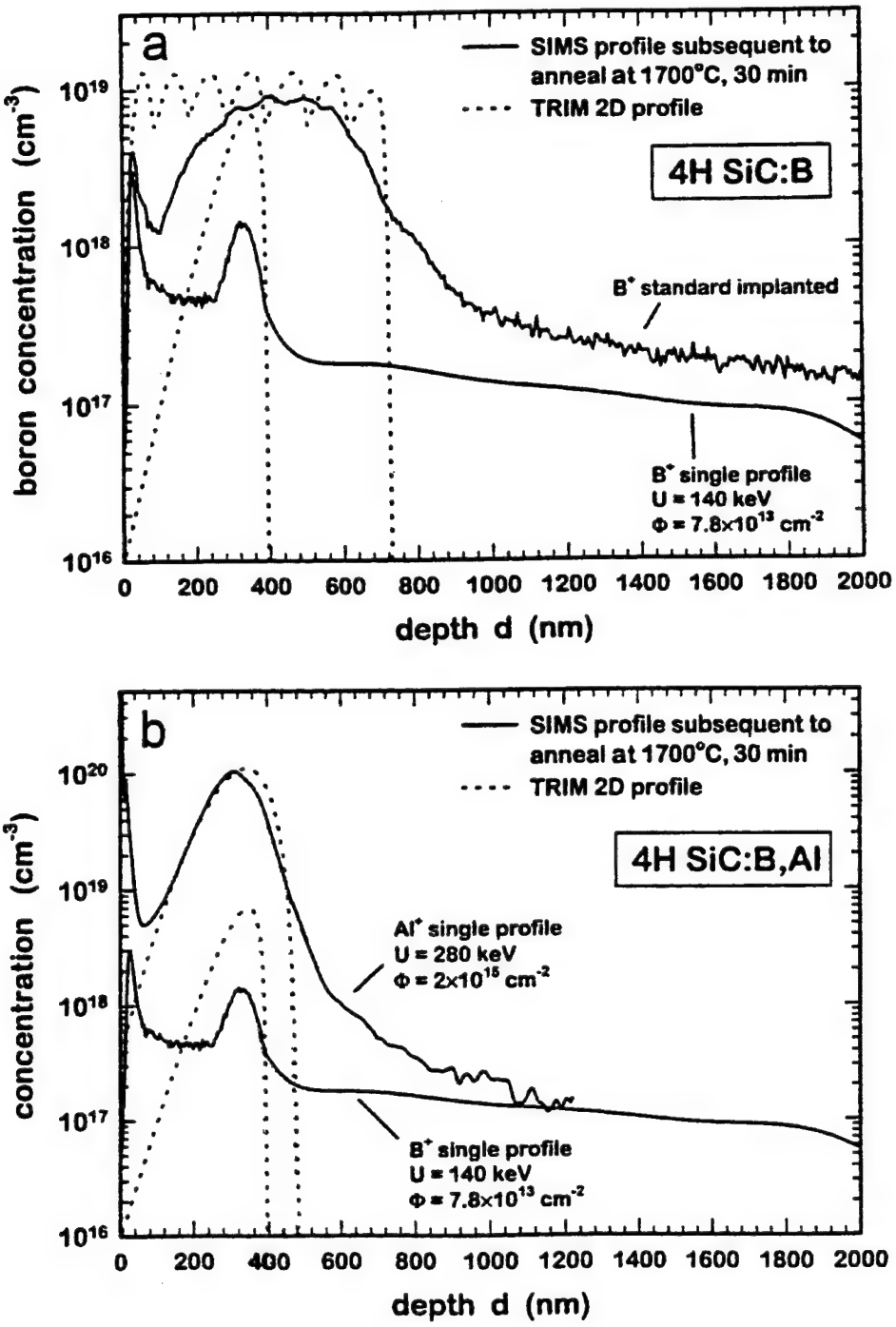

Figure II-13. Analysis of the change in doping profiles in 4H-SiC due to thermal annealing. The profile prior to anneal (dashed line) was calculated using TRIM 2D. The results of the SIMs measurements (solid line) of the doping profile after thermal annealing at 1700 °C for 30 min. Graph (a) shows diffusion of B ions in single energy and multiple energy (box profile) implantation schemes up to 2000 Å occurs with annealing. Graph (b) compares the diffusion of Al and B ions after annealing. Implantation energies and doses are listed [33:292].

It was also observed that annealing takes places over three stages. The first stage is an organization in the amorphous layer of the {000*l*} crystallographic planes, which established the long-range order along the <hki0> direction. The second stage is ordering of "packets" of the {000*l*} planes with relative positions corresponding to the cubic close packing. In the final stage, the full restoration of the polytypic structure in accordance with the underlying crystal matrix was observed, and elements of the hexagonal packing of the {000*l*} planes were evident.

The same researchers also attempted laser annealing (LA) of SiC using pulsed lasers. They demonstrated that structural perfection varies most strongly with laser pulse duration and that a pulse duration at least equal to the ordering time of a given polytypic was required. Increasing the pulse duration greatly improved the crystal structure of the annealed layers and restored the polytypic modification governed by the underlying matrix.

Several researchers at the Universitat Erlangen-Nurnberg also recently did an implantation study of p-type 4H-SiC [33,1997]. Both Al and B implantation into 4H-SiC epilayers, which have a nitrogen background doped to ~ $3x10^{16}$ cm^{-3}, at elevated (500 to 700 °C) and room temperatures were done and characterized using several experimental procedures. The mean concentrations in the implanted layers were $N_i(Al) = 2x10^{18}$ cm^{-3} and $N_i(B) = 1x10^{19}$ cm^{-3}. Hall measurements were used to determine the ionization energies and the activation. Ionization energies are found to be ~ 183 meV for the Al acceptor and ~ 285 meV for the B acceptor, and activation increases with anneal temperature up to 1800 °C for Al implanted samples and up to 1720 °C for B implanted samples. Figure II-14 and Figure II-15 show the experimental results of the temperature dependent Hall effect measurements on p-type, Al and B implanted 4H-SiC; these results are similar to what it is expected for the samples in this study.

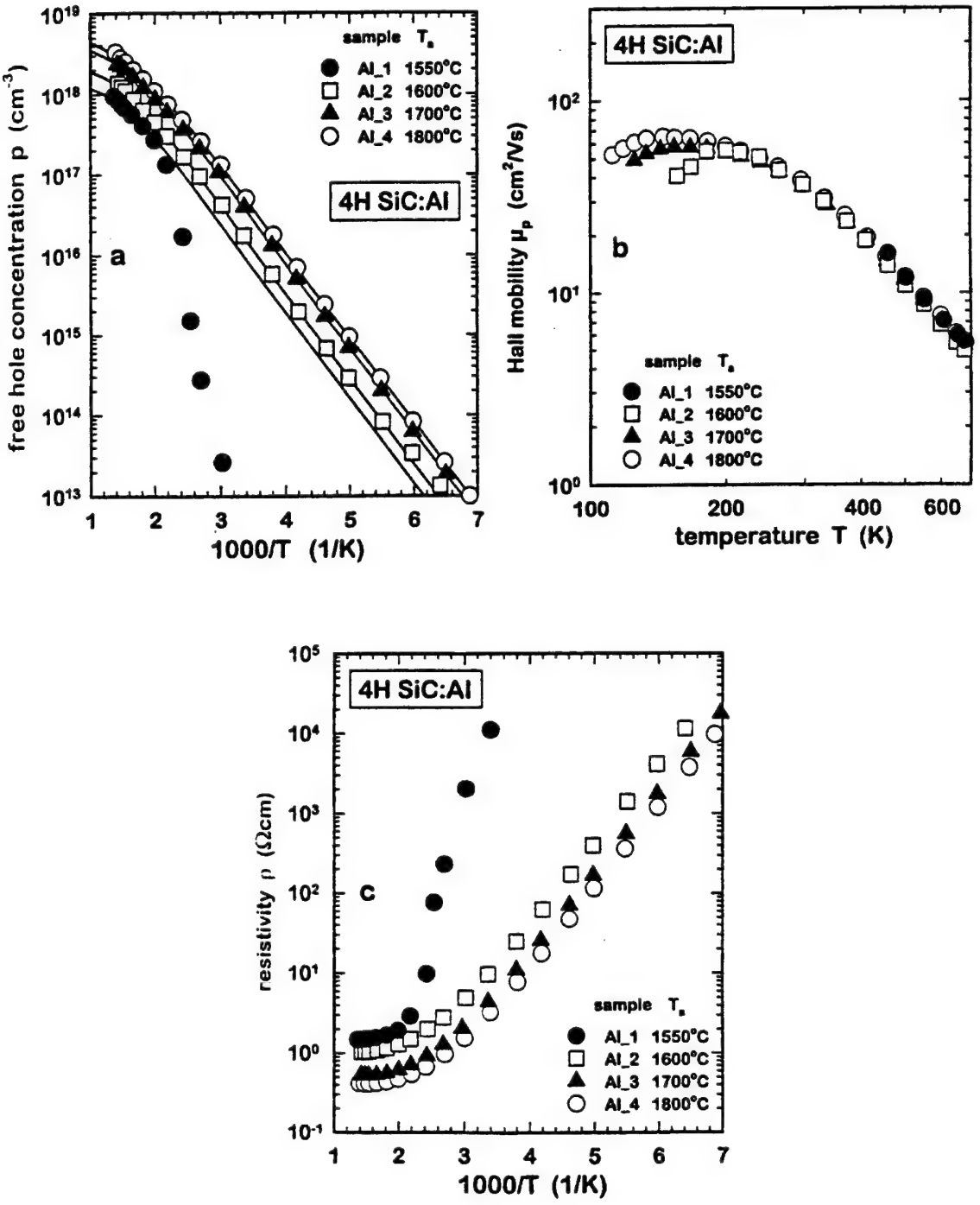

Figure II-14. Experimental results of the temperature dependent Hall Effect measurements of Al implanted p-type 4H-SiC. Results include measurements of the (a) free hole concentration, (b) Hall mobility, and (c) resistivity for Al implanted 4H-SiC samples for dose of 2 x 10^{18} cm^{-3}. These results indicate an optimum anneal temperature ≥ 1800 °C.

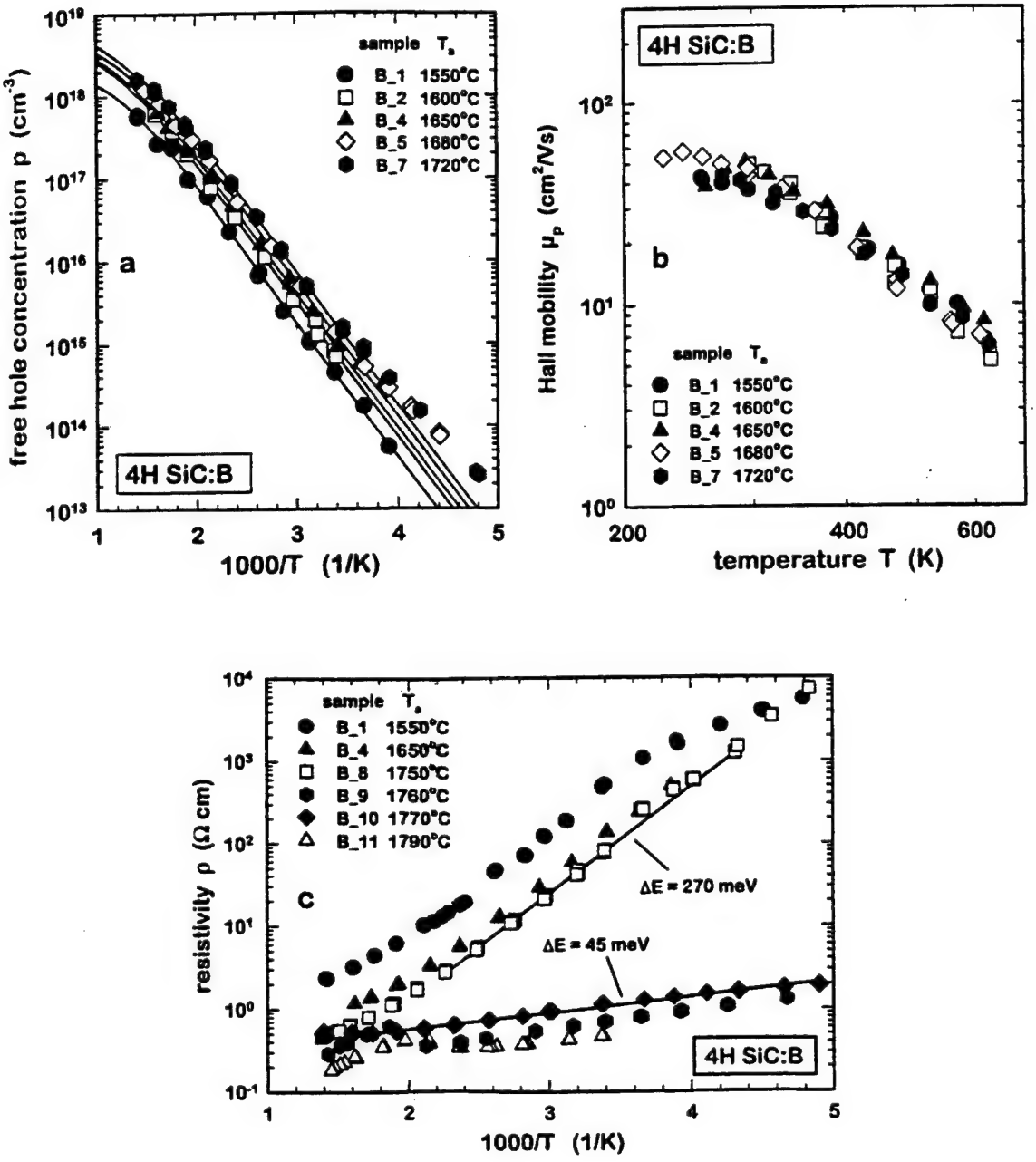

Figure II-15. Experimental results of the temperature dependent Hall Effect measurements of B implanted p-type 4H-SiC. Results include measurements of the (a) free hole concentration, (b) Hall mobility, and (c) resistivity for Al implanted 4H-SiC samples for dose of 1 x 10^{19} cm^{-3}. These results indicate an optimum anneal temperature of 1720 °C. A significant out-diffusion of B ions was observed for T_a above 1750 °C.

A significant systematic error was discovered in these results: the calculated electrical activation, $D = N_A / N_{dose}$, of the thermally annealed Al implanted ions was found to be greater than 1 for all thermal annealing temperatures (1550 °C, 1600 °C,

1700 °C, and 1800 °C). Whether this error can be accounted by a temperature dependent Hall scattering factor $r_H(T)$ remains to be investigated. The activation of B ions from thermal annealing was found to be less than the Al activation by a factor of approximately 4. This result is due to both the competitive processes for B atoms to occupy Si sites instead of C sites, and for the outdiffusion of B atoms that occurs during the anneals. The B atom outdiffusion subsequent to annealing at 1750 °C is implied by the sample changing conductivity to n-type and the slope of the $\rho(1/T)$-curves corresponding to ionization energy of 45 meV, the accepted value for the nitrogen (N) donor, the background dopant for the samples. In past research, secondary ion mass spectroscopy (SIMS) analysis of B implanted samples was used to show that annealing at 1800 °C for 5 min caused all the B to diffuse away [38,233].

In the Al implanted samples, the compensation concentration is found to be two orders of magnitude higher than the background doping of the material which either indicates the further activation of N donors or generation of additional Al^+ deep donors. Deep Level Transient Spectroscopy (DLTS) measurements on the Al implanted samples confirms that these donors would have to reside at least > 1 eV above the valence band edge since only defect levels were discovered up to that energy level. The compensation concentration in the B implanted samples is also two orders of magnitude higher than the background doping. In this case, however, DLTS measurements showed that a certain fraction of B occupy the C lattice sites in the well-known deep D center, where they acted as donors making them partially responsible for the increased compensation. Finally, to further substantiate the connection of the D center with increased compensation, C^+ / B^+ and Si^+ / B^+ coimplantation was done. An increase of acceptor concentration and reduction in D-center concentration, implied by a reduction in compensation concentration, with C^+/B^+ implantation was demonstrated.

Figure II-16 shows the results of further studies by researchers in Japan on the activation of Al and B ions implanted in p-type 6H-SiC [32:50].

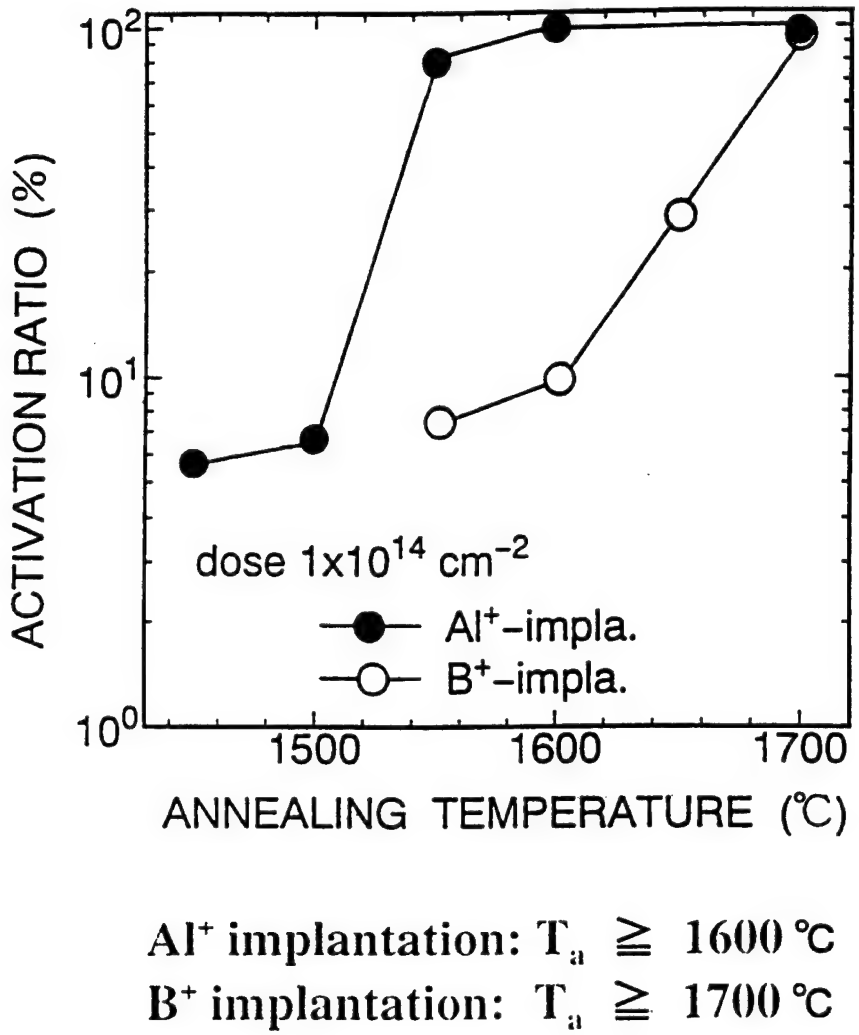

Figure II-16. Percentage of activated implanted Al and B ions at a dose of $1x10^{14}$ cm^{-2} implanted into p-type 6H-SiC for annealing at 1400 °C – 1700 °C for 30 min in Ar.

Figure II-16 indicates that the thermal annealing at 1600 °C and 1700 °C for 30 min. results in 100% activation for Al and B ions, respectively. These results show a clear activation dependence on annealing temperature and to some degree they differ with the results obtained for 4H-SiC discussed earlier. This difference should be expected considering the difference in crystal structure and bandgap, E_g. Considering these past results on p-type SiC, there is only one well-determined fact; a high temperature annealing between ~ 1550 °C and ~ 1750 °C is required for 100% activation.

Activation of Ion-implanted N-type 4H-SiC

A recent electrical and optical characterization was also done on the activation of P^+ and N^+ ions in epitaxial n-type 4H-SiC implanted at high temperature [39]. Although the research in this study is to characterize p-type 4H-SiC layers, the p-layers are grown on top of an n-epitaxial layer and n substrate and if conduction starts to occur through these layers, an idea about what to expect is necessary. The implanted n-type (nitrogen) samples were n- epitaxial layers grown by MBE on bulk n+ substrate material grown by modified sublimation that were implanted with various ion species, P, N and Ar, at several different energies with doses ranging between $1x10^{13}$ and $1x10^{14}$. The samples were then annealed at 1400 °C, 1600 °C, or 1800 °C for 30 min in flowing Ar gas. Ohmic contacts were made in the van der Pauw geometry using evaporated 500 μm diameter dots of Ti / Ni.

The donor activation energies were determined to be ~ 46 meV for the P-implanted samples and ~ 63 meV for the N-implanted samples. The annealing temperature that maximized free carrier concentration in each sample were found to be near 1600 °C for P-implanted and near 1400 °C for N-implanted 4H-SiC. CL measurements showed that both N- and P-implanted samples had significantly high concentrations of damage-related sites. Less damage or less complexing of residual substitutional nitrogen occurred from phosphorous implantation than from nitrogen implantation, an interesting result considering that phosphorus is the heavier of the two atoms.

This chapter has introduced several of the important ideas and the necessary relationships of semiconductor theory for understanding this research. This introduction was focused on developing the relationship between carrier concentration and temperature, which is central to this study and provides some basis for developing the other important relationships; mobility vs. temperature and resistivity vs. temperature. Past research on implantation and annealing of p-type and n-type 4H-SiC has also been reviewed, with the goal in mind that we will be able to compare our results to those. The past research also introduced some other important relationships, like percent activation and electrical activity. The next chapter will discuss the experimental methodology. Both the sample geometry and the experimental technique will be reviewed.

III. Methodology

The preceding chapter mentioned the results of several studies on the implantation and annealing of 4H-SiC. In this study, further experimental work has been done to electrically characterize implanted p-type 4H-SiC. Hall effect measurements were done on Al and B implanted epitaxial p-type 4H-SiC at temperatures ranging from 100 K to 600 K. This chapter reviews the experimental methodology for this research, which includes the sample growth, implantation and preparation, and the characterization technique, temperature dependent Hall effect measurements. The Hall effect in general is also reviewed.

III-1. Experimental Procedure

The experimental procedure includes the sample growth geometry, implantation and annealing, the cleaning procedure for annealing and prior to depositing metal for contacts. The physical process of making ohmic contacts is also described. Difficulties encountered with making good ohmic contacts on the samples led to attempting several different approaches. The question of why these difficulties occurred is discussed in the next chapter.

Sample Geometry

The samples used in the experiment were purchased from Cree Research. The sample growth geometry is shown in Figure III-1.

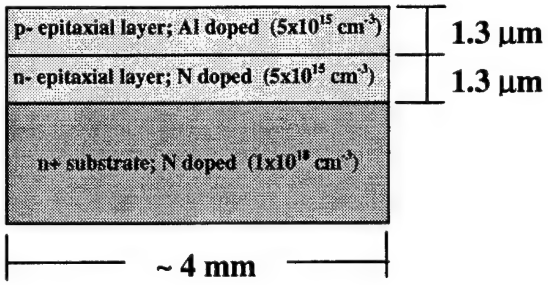

Figure III-1. Side view of typical growth geometry of p-type 4H-SiC samples used in this research. There are 3 main layers: a low doped 1.3 μm p-type (aluminum) epitaxial layer on top of a low doped 1.3 μm n-type (nitrogen) epitaxial layer, on top of a highly dope n-type (nitrogen) bulk substrate. The p-layer was implanted with different ions at different temperatures and different doses. The built-in pn junction electrically isolates the p-layer. Samples are roughly ~ 4 mm x 4 mm squares.

As Figure III-1 shows, the samples are1.3 μm epitaxial p-type layers grown on 1.3 μm epitaxial n- type layers, which were in turn grown on bulk n-type substrate material. The epitaxial p-layers are low doped ($N_A - N_D = 5x10^{15}$ cm^{-3}) grown by MOCVD. Metalorganic chemical vapor deposition (MOCVD) is a variation on the MBE method discussed in the previous chapter, where gases replace the elements and the forming means is a chemical reaction. Aluminum and nitrogen are the background dopants for the p- and n-type layers, respectively. The substrate material is grown by modified sublimation and has a doping concentration ~ 10^{21} cm^{-3}.

Implantation and Annealing

Implantation of the samples was done with either Al or B ions at doses ranging from $1x10^{13}$ cm^{-2} to $1x10^{14}$ cm^{-2}, resulting in peak implantation concentrations from $2x10^{17}$ cm^{-3} to $1x10^{19}$ cm^{-3}. Samples were implanted either at or above (500 °C) room temperature. The implantation energy was 180 keV and 85 keV for the Al and B implantation, respectively. This resulted in peak concentration depths between 2200 and 2500 Å. The samples were implanted at either of three different doses: $1x10^{13}$ cm^{-2}, $1x10^{13}$ cm^{-2}, or $1x10^{13}$ cm^{-2}.

Because the samples are low level doped, a shallow (50 keV), high dose (~ $1x10^{19}$ cm^{-3}) implantation into the corners was done to assist in forming ohmic contacts for the Hall measurements. This was done because for tunneling current, which is always the case with p-type 4H-SiC, contact resistivity decreases with concentration.

Typical sample geometry displaying the region where shallow implantation occurred is shown in Figure III-2.

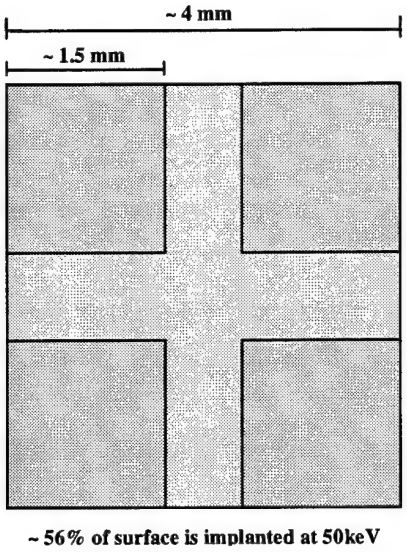

Figure III-2. Geometry of the Hall samples showing the corner region where shallow Al implantation (50 keV) was done. The implantation region covers a significant portion of the sample (> 50%).

Spin-on photoresist was applied to the sample's surface prior to the shallow implantation to allow for these regions to be defined. It is important to notice that the shallow implantation was done over most of the surface of the sample (> 50%). In addition, for both Al and B implanted samples, Al was used for shallow implantation.

Annealing was done in a vacuum furnace, capable of annealing up to ~ 2400 °C. Prior to annealing, all samples were descummed and then oxide etched using the following cleaning procedure:

Trichloroethlyene (TCE)	- 30 sec (rinse)
Acetone	- 30 sec (rinse)
Methanol	- 30 sec (rinse)
Deionized (DI) water	- 30 sec (rinse)
H_2SO_4: H_20_2 (1:1)	- 5 min (soak)
DI water	- 5 min (soak)
N_2 blow dry	- 30 sec

The annealing was done in an Ar atmosphere. Samples were annealed at 1550 °C, 1650 °C, or 1750 °C for 30 min. Samples were located on a graphite block during the

annealing, not within a SiC crucible. This was done with the intention that the surface state density would increase due to the surface degradation, which would result in a higher carrier concentration at the interface for forming ohmic contacts. As discussed in the previous chapter, specific contact resistance is inversely proportional to the increase concentration of dopant atoms.

Metal Deposition and Contact Annealing

After annealing, samples were then cleaned again prior to metal deposition for forming ohmic contacts. Metal contacts are required for making the Hall measurements. Best results were achieved using the following cleaning procedure:

TCE	- 30 sec (rinse)
Acetone	- 30 sec (rinse)
Methanol	- 30 sec (rinse)
DI water	- 30 sec (rinse)
H_2SO_4: H202 (1:1)	- 1 hr (soak)
HF: DI water (1:1)	- 1 hr (soak)
DI water	- 5 min (soak)
N_2 blow dry	- 30 sec

After cleaning, samples were then immediately placed in the evaporator system. Several different combinations of metals, amounts, and means were used for making contacts because it was extremely difficult to make good ohmic contacts on the material. The combination of metals and amounts used to form contacts on the samples include Al (6000 Å), Al / Ni (2000 Å / 2000 Å), and Al/Ti (500 Å / 4000 Å). The metal deposition was done at a nominal evaporation pressure of ~ 10^{-6} Pa by thermal and e-beam evaporation using an Edwards Auto 306 Turbo metal evaporators. Metal deposition by sputtering was also done on 4 samples at the AFRL, Materials Directorate, Wright Patterson AFB, OH.

After metal contacts were formed, they were annealed in a Rapid Thermal Annealing (RTA) furnace. Contact annealing was done at temperatures ranging from 450 to 1150 °C and for times ranging from 1 min to 10 min. These ranges were again driven

by the inability to make good ohmic contacts. Good contacts could not formed by contact annealing at temperatures < 950 °C for 5 min.

III-2. Characterization Technique

Electrical characterization using the Hall Effect is a simple and effective means to determine several important properties of the semiconductor. The following section will discuss the basics of the Hall effect using the Hall bar as an example. From this example, the material properties of carrier concentration, resistivity, and mobility will be made clearer, and the associated relationships for each with measured quantities will be developed. Then, the same idea will be applied to make Hall effect measurements using the van der Pauw geometry. Further discussion will include a description of the systematic error with each measurement, which is related to the contact size and placement, and a description of the measurement apparatus.

Hall Effect Measurements

To control the conducting properties of a semiconductor, the most important property to be controlled is the concentration of dopant impurities, especially for use in electronic devices. Accurate measurements of this quantity are therefore very important. Determining the impurity concentration and impurity types can be accomplished by measuring the resistivity ρ and Hall coefficient R_H over a wide temperature range [40:2]. These quantities are related to the carrier concentrations and the carrier mobilities by the following expressions

$$\rho^{-1} = e(p\mu_p + n\mu_n) \tag{22}$$

$$R_H = \frac{(p\mu_p\mu_{Hp} - n\mu_n\mu_{Hn})}{e(p\mu_p + n\mu_n)^2}, \tag{23}$$

where p and n are the hole and electron concentrations, μ_p and μ_n are the conductivity mobility for holes and electrons, μ_{Hp} and μ_{Hn} are the Hall mobility for holes and electrons, respectively, and e is the charge on electrons. If, for instance, hole conduction dominates these equations reduce to the following

$$\rho^{-1} = e\, p\, \mu_p \tag{24}$$

$$R_H = \frac{\mu_{Hp}}{e\, p\, \mu_p} = \frac{r}{e\, p}, \tag{25}$$

where $r = \mu_{Hp} / \mu_p$ is the Hall scattering factor, which accounts for the distribution of velocities of the moving charges in the sample. The Hall scattering factor is temperature dependent and on the order of unity. It can only be measured over limited ranges in a few cases. It is usually calculated or estimated, or in most cases including this research, taken to be unity. The carrier concentration and mobilities are then calculated from

$$p = \frac{r}{R_H\, e} \simeq \frac{1}{R_H\, e} \tag{26}$$

$$\mu_{Hp} = \frac{R_H}{\rho} \tag{27}$$

$$r = \frac{\mu_{Hp}}{\mu_p}. \tag{28}$$

R_H and ρ are the measurable quantities in equations (26) and (27). Measuring these quantities involves making voltage measurements at several locations on a sample that is held at a precisely controlled temperature and subjected to a constant current in the presence and absence of a magnetic field.

Hall Bar Technique

For Hall effect measurements using the Hall bar geometry as shown in Figure III-3,

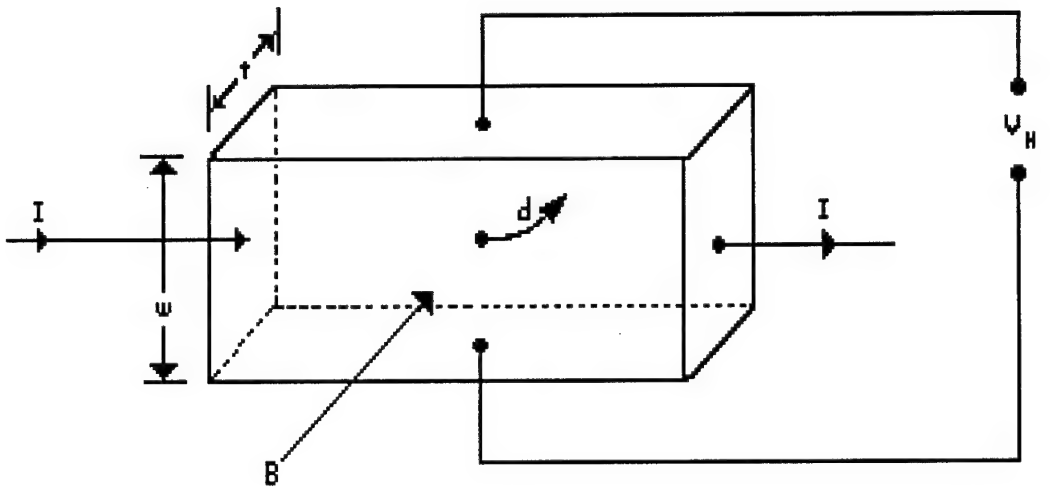

Figure III-3. Schematic of the Hall effect measurement using the Hall bar geometry. Current, *I*, is passed through the sample, *B* is the magnetic field applied perpendicular to *I*, V_H is the Hall voltage measured perpendicular to *I* and *B*, and *d* is the deflected (positive) charge. The sample thickness and width are *t* and *w*, respectively.

a current, I, is passed through the sample, and the Hall voltage, V_H, is measured. The Hall voltage is the result of the magnetic field deflecting the moving charges in a direction mutually perpendicular to B and I. This occurs until the charge concentration at the top and bottom of the sample are large enough that the force from the electrostatic field, generated by this charge separation, balances the Lorentz force being applied to the moving charges. This electrostatic field, or Hall field, is equal to the Hall voltage, V_H, divided by the width between the contacts, w.

Given the current density, $J = n\,q\,v = I/(w\,t)$, the Hall field, $E_H = V_H/w$, and the Lorentz force, $F_{mag} = q\,v\,B$, we equate the two forces on the positive charge carriers. The resulting proportionality constant between the current and the Hall field is the Hall coefficient R_H. It is expressed as the following

$$R_H = \frac{V_H}{I}\,\frac{t}{B}\,. \tag{29}$$

The Hall coefficient is directly related to the free carrier concentration, as expressed in equation (26).

The resistivity is the resistance of the sample corrected for the dimensions of the sample. The schematic diagram for resistivity measurement schematic for the Hall bar experiment is shown in Figure III-4.

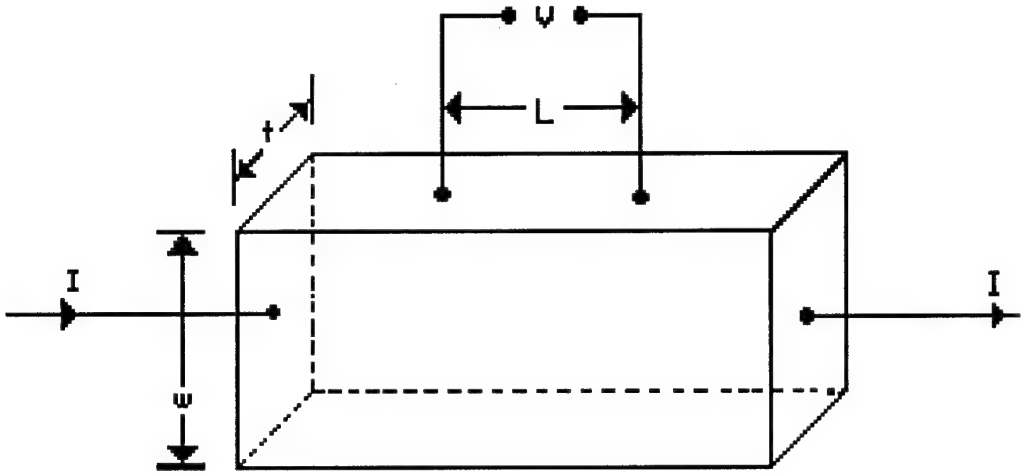

Figure III-4. Schematic of the resistivity measurement using the Hall bar geometry. *I* is the current passed through the sample and *V* is the voltage measured between the contacts separated by a distance *l*. The sample thickness and width are *t* and *w*, respectively.

The resistivity for a sample in this geometry can then be calculated from measurable quantities, V and I, and the dimensions of the sample, using the following expression

$$\rho = \frac{V}{I}\frac{wt}{l}. \qquad (30)$$

Van der Pauw Technique

For this study, Hall effect measurements will be made using the standard van der Pauw geometry. The van der Pauw method has the advantage that no physical dimensions need to be measured to calculate the sheet resistance or sheet-carrier concentration. The sample can also be of arbitrary shape as long as it is flat, simply connected and of uniform thickness with contacts on the periphery. This is visible in Figure III-5, the schematic for Hall effect measurements using the van der Pauw technique.

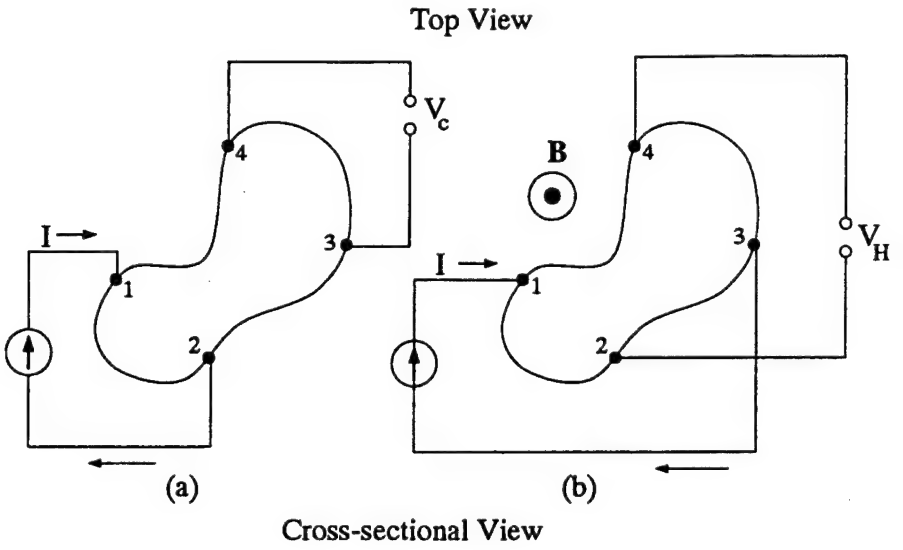

Figure III-5. Schematic diagram of the Hall effect measurement using van der Pauw technique. Diagram (a) depicts resistivity measurements. Diagram (b) depicts Hall effect measurements. Samples can be of arbitrary shape, but must be of uniform thickness and completely connected (no holes).

The Hall effect and resistivity measurements for van der Pauw are similar to the Hall Bar experiment in that voltages are measured across the contacts in the presence and absence of a magnetic field. The van der Pauw technique differs, however, in that all contacts are used for applying current and measuring voltages. For typical van der Pauw geometry resistivity measurements as shown in Figure III-5a, a current, I, is passed through contacts 1 and 2, and a voltage, V_c, is measured between contacts 3 and 4. A resistance, $R_{ij,kl}$ is defined to be $R_{ij,kl} = V_{kl} / I_{ij}$, where the current enters contact i and leaves contact j, and $V_{kl} = V_k - V_l$. The sample volume resistivity, ρ, with no magnetic field ($B = 0$) is given by

$$\rho = \frac{\pi\, t}{\ln(2)}\left[\frac{R_{21,34} + R_{32,41}}{2}\right] f(Q), \qquad (31)$$

where t is the thickness of the sample, $f(Q)$ is a geometrical correction factor, t is the thickness of the active layer and Q is the ratio of the resistances, either $R_{21,34} / R_{32,41}$ or $R_{32,41} / R_{21,34}$, whichever is greater than unity. If $Q = 1$ the sample is uniform. The geometrical factor is determined by the following transcendental equation

$$\frac{Q-1}{Q+1} = \frac{f}{\ln(2)} \operatorname{arccosh}\left\{\frac{1}{2}\exp\left[\frac{\ln(2)}{f}\right]\right\}. \tag{32}$$

As will be discussed further in the next section, when making measurements on high resistivity samples, the measurement apparatus used must have been designed for high resistivity measurements. This requires employing high impedance meters and using an electrometer, triaxial cable combination that shields the signal.

The Hall mobility, μ_H, and Hall coefficient, R_H are found using the configuration in Figure III-5b. In this configuration, the Hall voltage is the difference in potential between contacts 4 and 2, with and without an applied magnetic field, $V_{H42} = (V_4 - V_2)_B - (V_4 - V_2)_0$, while a current, I, is passed between contacts 1 and 3. The Hall voltage in terms of the mobility is the following:

$$V_{H42} = \rho \mu_H \frac{BI}{t}. \tag{33}$$

The Hall coefficient is given by the following:

$$R_H = \frac{t}{B}\left(\frac{R_{31,42} + R_{42,13}}{2}\right), \tag{34}$$

where the Hall voltages, V_{H42} and V_{H31}, are averaged together and t is the thickness of the active layer. In this study, measurements of resistance were taken across all possible combinations of pairs of contacts, backwards and forwards. There are eight measurements for resistivity total that are averaged together. For measuring the Hall coefficient, eight measurements are also done; forwards and backwards across each pair in a positive and negative B field. Thus, a total of sixteen measurements are taken at each temperature. By averaging the measurements this way, the effects of any temperature gradients within the sample are significantly reduced.

In the van der Pauw geometry, the uncertainty in the measurements of resistivity, Hall coefficient, and mobility are related to the size and position of the contacts on the sample. Ideally, point contacts on the periphery of the sample should be used, but since this is not feasible, the error must be contended with. Estimates of the errors in the resistivity, Hall coefficient and mobility for a square sample with 4 contacts are given the following:

$$\frac{\Delta\rho}{\rho} \simeq 4\left[\frac{-1}{16\ln(2)}\frac{l_c^2}{l_s^2}\right] \tag{35}$$

$$\frac{\Delta\mu_H}{\mu_H} = \frac{\Delta R_H}{R_H} \simeq 4\left(\frac{2}{\pi^2}\frac{l_c}{l_s}\right). \tag{36}$$

where l_c and l_s are the length of the one contact (diameter for a circular contact) and the length of the sample respectively. By forming cloverleaf shaped samples instead of square samples, the errors can be significantly reduced, however, contact size can still be a source of error. For this research, apart from the above-mentioned built-in errors, estimates of the uncertainty in resistivity, concentration and mobility are quite large because each sample had a shallow implantation done on it over a significant area of the sample (> 50%). This will be discussed further in the next chapter.

When the active layer is not uniform, the concentration, mobility, and resistivity will vary with the thickness. As mentioned in the preceding chapter, in these situations the resistivity and Hall effect measurements must be done sequentially between chemical etchings, which remove thin layers, to profile the sample. A second technique for profiling non-uniform samples employs a Schottky gate deposited on the surface of the van der Pauw structure to make portions of the sample electrically inactive. Schroder discusses these techniques further [41:202].

Hall Effect Measurement Apparatus

A schematic block diagram of the Hall effect measurement apparatus is given in Figure III-6.

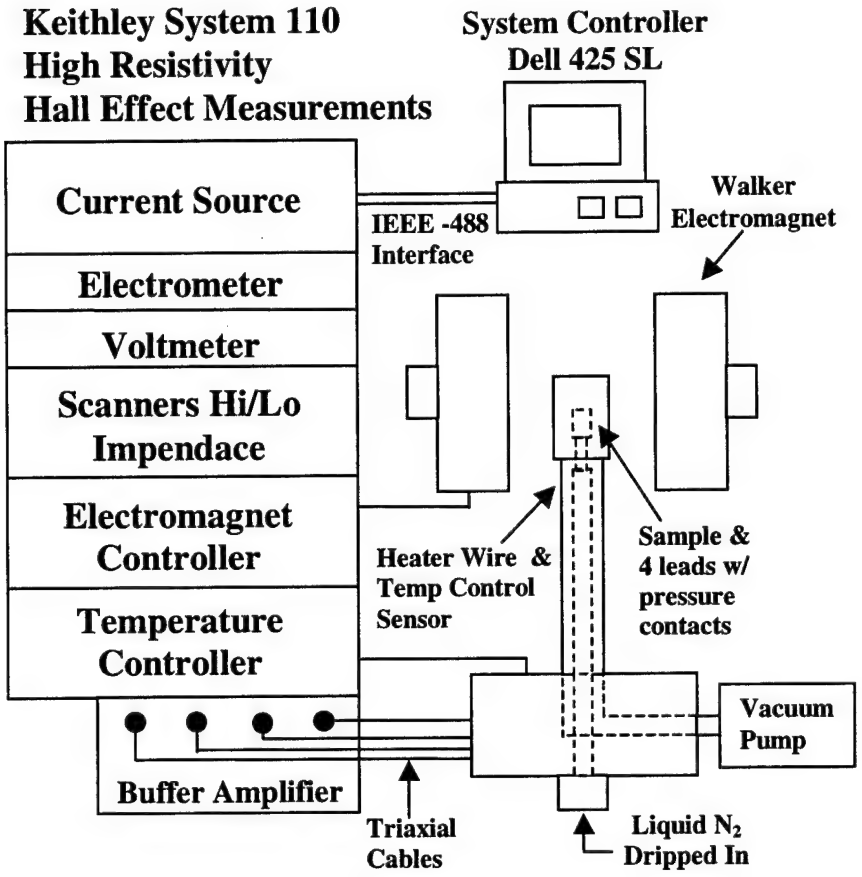

Figure III-6. Schematic diagram of the automated temperature dependent Hall effect measurement apparatus used in this research. Cooling down to 77K is accomplished by a liquid nitrogen supply that is dripped slowly into dewar. Heating up to 700 K is accomplished by Walker Temperature controller. Vacuum pumping down to < 10^{-6} Pa is accomplished by Drytel Vacuum Pump.

The automated Hall effect apparatus used in this research is a System 110 from Keithley, Inc. This apparatus allows for sheet resistivity and Hall voltage measurements to be made under computer control, via the IEEE-488 interface. The triaxial cables carry the electrical signals. To deal with the cable charging effects and small leakage currents which are significant in high resistivity samples, the cables have their inner shields kept at the signal voltage by the electrometers which are operated as unity-gain buffer amplifiers. The setup is capable of passing currents as low as 10^{-10} A, which allows the system to measure resistances up to $10^{12}\ \Omega$.

This chapter discussed the experimental methodology used in this study, which included the sample growth and implantation and annealing. The Hall effect and resistivity measurements were explained and the governing equations for carrier

concentration, Hall mobility, and resistivity in the Hall Bar and van der Pauw geometry were stated. Then the apparatus used to make the measurements was described. The next chapter focuses on the results of this study and the accompanying analysis.

IV. Results and Analysis

In this chapter, the results of the resistivity and Hall measurements and corresponding analyses are presented. This chapter will begin by discussing exactly what measurements were made. Then, a complete discussion of the problems encountered during the research will be made. This will include the difficulties encountered with forming good ohmic contacts and the uncertainty in the measurements due to contact size and the shallow implantation. Next, the results and analyses of the measurements on the Al and B implanted samples will be presented. Finally, the chapter will conclude with reviewing the significance of results in this research and a comparison to past research.

Temperature dependent resistivity and Hall effect measurements were made on 34 different implanted, p-type 4H-SiC samples. The samples differed by four characteristics: implanted ion, dose, implantation temperature, and annealing temperature. A sample matrix of this size would have allowed several questions to be answered; however, good ohmic contacts could not be easily formed on almost all of the samples. For that reason, a significant portion of the research was devoted to characterizing the effects of poor contacts on the Hall measurements, and to improving our ability to form contacts. The first section describes the results and analyses of room temperature measurements done to electrically characterize these effects.

IV-1. Forming Ohmic Contacts

A substantial difficulty prior to making the resistivity and Hall measurements was in forming good ohmic contacts on the p-type 4H-SiC samples. Ohmic contacts by definition have a linear I - V dependence. The I - V relationship between all possible combinations of contacts on samples must be evaluated prior to doing Hall measurements. This is because the equations for resistivity and the Hall coefficient in van der Pauw geometry are based on the assumptions that the contacts have a small resistance and a linear I - V relationship. This prevents one from measuring the electrical characteristics of the contacts instead of the sample. In this study, the I - V curves of the contacts on each sample were evaluated using a curve tracer, a device similar to an

oscilloscope that measures the curve by passing different currents through the sample, forward and reverse, and measuring the voltage at each.

For p-type 4H-SiC, it is well understood that is physically impossible to have a Schottky barrier height (SBH) of zero at the metal-semiconductor interface, as described in Chapter II. Therefore, electrons' tunneling through the barrier is the means for passing current in to the sample. As previously discussed, the accepted procedure for forming ohmic contacts on p-type 4H-SiC is roughly to deposit metal, usually Al, on a clean sample surface, followed by a 5 min "burn-in" via thermally annealing the contacts (~ 950 °C). The annealing allows some of the metal to diffuse in creating a metallic region of high acceptor concentration which decreases the depletion width allowing holes to effectively tunnel [42,94]. Good ohmic contacts on p-type 4H-SiC will have linear *I - V* curves and small specific contact resistances (< 10^{-5} Ω–cm^2) [42,83].

Example I-V Curves

Contacts formed on the p-type 4H-SiC samples in this research were generally rectifying in some manner. Two commonly observed examples of the rectification are shown in Figure IV-1.

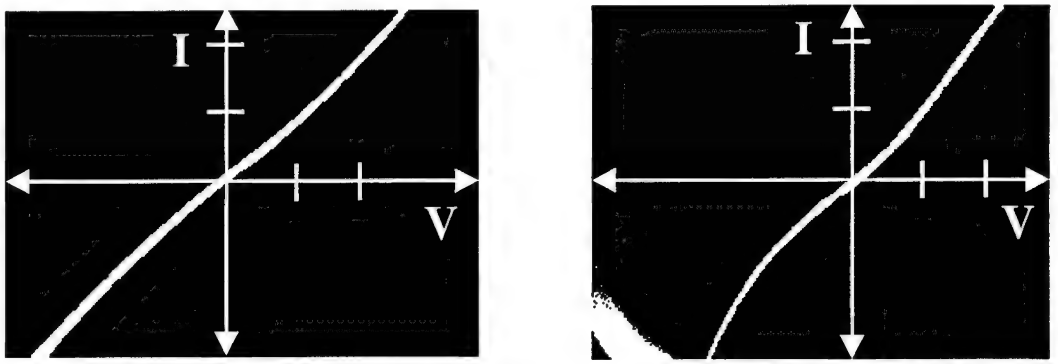

(a) (b)

Figure IV-1. Typical *I-V* curves for the metal contacts formed on low doped p-type 4H-SiC samples. The scale on the y-axis, current, is 1 μA / div; the scale of the x-axis, voltage, is 1 volt / div. Samples are implanted at 300 K with Al dose of $3x10^{13}$ cm^{-2}. In the ideal case, the *I-V* curve is linear. The two curves are measured with two different contacts, and curves are on the same scale.

The *I - V* curves measuring different contacts shown in Figure IV-1 (a) and (b) reflect the poor quality of the samples and how significantly each contact can vary compared to

other ones on the sample. The next illustration, Figure IV-2, shows a different example of contact difficulties; applying pressure to the curve tracer probe on the contact changes the *I* - *V* curve. The change in slope with pressure applied is an indication that the current is partially "poking through" the p-layer and being passed through either the n-epitaxial layer or more likely the highly doped substrate layer.

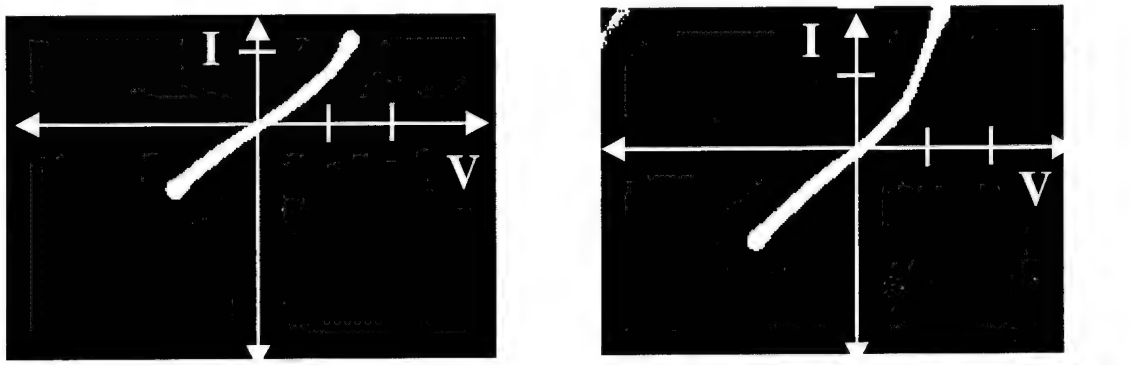

(a) (b)

Figure IV-2. *I-V* curves for a 4H-SiC sample with probe (a) not pressured and (b) under pressure. The increase in length in the portion of the curve with the steeper slope is an indication that metal is punching through to n-type epitaxial layer and substrate. Curves are on the same scale as in Figure IV-1.

There is no one clear explanation as to why these difficulties were encountered. It would not be unusual to have difficulties making ohmic contacts on low doped material ($N_A - N_d = 5x10^{15}$ cm^{-3}) considering that the barrier width at the interface, through which tunneling currents pass through, depends inversely on free carrier concentration and because several parameters affect the forming of ohmic contacts. This problem is unusual for these samples, however, considering the effort made to decrease the barrier width beforehand by doing the shallow corner implantation and increasing the acceptor concentration to roughly ~ 10^{19} cm^{-3}. On only 2 samples were reasonably good ohmic contacts were formed.

Attempts were made at forming good contacts on several samples using a standard contact forming procedure before a serious effort was undertaken to improve the deposition and contact annealing process. Forming good ohmic contacts is a long procedure with several parameters, some of which are not easily defined, such as the interface barrier. Thus, if poor contacts resulted for one sample, it is a hard to decide if

the metal deposition and annealing procedure are correct because any number of mistakes could have made in the deposition process or with the original sample preparation. Some of the parameters that affect forming contacts as well as the physics of ohmic contacts were discussed in Chapter II.

The first attempts at forming metal contacts were depositions of Ni 2000 Å / Al 2000 Å. The Ni was deposited on top of the Al to improve the surface morphology. From these first attempts, it was observed that contacts on the same sample could have significantly different *I* - *V* curves. Attempting to improve the contacts by annealing them at higher temperatures increased the linearity of the *I* - *V* curves in all cases. However, an upper limit on contact annealing was found since after repeated annealing at higher temperatures up to 1150°C for 5 min, enough metal diffused through the *p*- layer to allow the n-type layer and substrate to conduct. This conduction was implied by Hall measurements, which showed n-type conductivity. The measured sheet-concentrations also increased to ~ 10^{17} cm^{-2}, which is on the order of the expected concentration in the substrate layer. Metal contacts that diffused through the p-layer also became perfectly ohmic with very steep *I* - *V* curves; steep enough that at first it was proposed that shorting was occurring. To prevent diffusion through the p-layer from occurring again, contact-annealing temperature/time was kept below the 1150 °C / 5 min limit.

After the original contact formation procedure proved largely unsuccessful, various other deposition procedures found in the literature were attempted; the differences in these procedures amounted to using different cleaning methods, types and amounts of metal deposited and annealing temperatures and lengths of time. An attempt was also made to improve the old contacts by depositing extra metal on them, which was thought would prevent the probes from poking through the p-type layer. As deposited, this extra metal gave the contacts Schottky behavior, but after annealing the contacts had improved, but not significantly enough to make them ohmic. When it became obvious that these procedures were also ineffective then a systematic evaluation of the experimental procedure and equipment were done, the results of which are discussed in the next section.

Evaluation of Experimental Procedure for forming Ohmic Contacts

When it was discovered that good ohmic contacts could not be easily formed on the samples, it was decided that each step of the contact deposition process should be evaluated. First, the actual amount of metal being deposited by the thermal evaporator was checked. The contacts appeared quite thin, and it was suspected that the actual amount of metal being deposited might be less than the machine was reporting. The metal height on the surface was measured using a Tencor Instruments step profiler, which runs a probe over the sample to measure the relative height of the surface. On average, the amount of metal being deposited was correct, however, the surface appeared extremely rough and the contact surface was not uniform. Depositing extra contact metal on the old contacts was thought to improve the surface morphology, however, as mentioned before, it did not lead to good ohmic contacts.

The Al being deposited was then investigated to see if it was completely oxidized or contaminated. This was accomplished by forming metal contacts on a sample of pure Si doped with boron. The Al metal was thermally evaporated on to the sample. The preparation process for forming these contacts was based on a standard found in the literature. These contacts were found perfectly ohmic upon annealing at 425 °C, and thus it was concluded that the Al was not contaminated.

The next part of the procedure to be evaluated was the actual surface cleaning and deposition process for p-type 4H-SiC. These were evaluated by forming contacts on highly doped ($N_A - N_D = 10^{21}$ cm^{-3}) p-type bulk 4H-SiC substrate material. Substrate material in general is of less quality than epitaxial material. Despite this ohmic contacts were formed by thermal deposition of 5000 Å of Al and annealing at 1000 °C for 5 min. The cleaning procedure used to form these contacts is exactly the same procedure that was used on the p-type epitaxial samples and that is found in the literature. Since ohmic contacts were formed on this sample it was concluded that the surface cleaning and metal deposition process were at least adequate to form contacts on highly doped material, but not necessarily adequate for forming ohmic contacts on low doped material like the samples in the research.

Essentially this is all that was done to evaluate the physical process that was being used for forming ohmic contacts. Since no mistakes in the original process were

uncovered, the focus to form ohmic contacts slightly shifted to the samples and to finding a different process. The first step was trying a different deposition process that had been successfully used in the past for forming ohmic contacts on p-type 4H-SiC. On four different samples, implanted with various ions and concentrations, 6000 Å of Al was sputtered on the sample surface in the van der Pauw geometry. Prior to the sputtering, the standardized cleaning procedure, similar used on our samples, was followed. The surface cleaning and sputtering were done in the AFRL/Wright Patterson Materials Lab. This process has been employed there successfully for forming metal contacts on p-type 4H-SiC. The contacts on the four samples were thermally annealed at 925 °C for 5 min, but unfortunately were found to be rectifying. Similar results were obtained after several different attempts at forming metal contacts.

Considering this evidence, the procedure evaluation has made it apparent that the problem in forming good ohmic contacts was not with the experimental preparation, deposited metal, or the result of poor lab equipment. The evidence points more to the problem being with aspects of the sample preparation. The two most likely aspects responsible for these difficulties are the shallow implantation and the sample cleaning prior to the annealing. The shallow implantation may have resulted in a stable amorphization, which it has been reported to prevent the formation of ohmic contacts [31:879]. The sample cleaning prior to annealing may have been inadequate to completely remove grease and any oxide layers that had formed on the samples. The samples were purchased several years prior to the beginning of this study, and therefore are old by common standards. Oxide layers would have formed on the surface during that time and any surface impurities could have diffused in to the sample during the annealing.

Ion implantation for forming contacts was previously mentioned as a means for selective doping in the contact region in Chapter II. The problems associated with ion implantation for contacts are the similar to those seen for doing full sample implantation: diffusion of the implanted species during annealing, diffusion caused by high temperature implantation (> 500 °C), and the lattice damage resulting from implantation. Out diffusion by evaporation of impurities through the surface can also be a problem; it is reported to occur at annealing temperatures above 1700 °C [34:275].

As discussed in Chapter II, annealing causes the implantation profile to spread. Answering the question exactly how did the shallow implantation profile change with the annealing would require a SIMs analysis on the implanted corners, which was not done. Samples in this research had their corners Al implanted at 50 keV to produce a mean concentration of 10^{19} cm^{-3}. The critical fluence that results in stable amorphization for 6H-SiC for Al implantation is reported by Kimoto as $1x10^{15}$ cm^{-2} [32:879] and as $5x10^{15}$ cm^{-2} by Spiess [31]. *Stable* is implying that recrystallization does not occur after anneals up to at least 1700 °C. 4H-SiC should have a critical fluence close to these values. Spiess calculated the implantation profiles for 6H-SiC Al implanted at 50 keV and the results show that a mean concentration of ~ 10^{19} cm^{-3} occurs for implantation roughly between $5x10^{14}$ cm^{-2} and $1x10^{15}$ cm^{-2}. According to these numbers, then the shallow implantation dose was close to the limit of amorphization, as reported by Kimoto. Therefore, the possibility exists that the sample corners were amorphisized by the shallow implantation.

Another possibility is that the surface was not properly cleaned before the annealing and that this resulted in contamination of the sample. During the sample annealing at 1550 °C and 1650 °C, bubbling on the surface was visually observed which indicates some surface effects. The results of the Hall measurements also seem to indicate that the cleaning prior to annealing affected the measurements. The set of samples annealed at 1550 °C and 1650 °C, which were cleaned at the same time prior to the annealing, have similarly shaped free hole concentration plots. The plots for samples annealed at 1750 °C, which were cleaned at a different time, differed significantly from the plots from the 1550 °C and 1650 °C annealed samples and show behavior closer to what is expected. The analysis of the actual temperature dependent Hall measurements will highlight this fact. The possibility also exists that the bubbling on the surface was a mixture of the surface impurities and the outdiffusion of implanted impurities. The next section contains the results of measurements done to characterize the effects of the poor ohmic contacts formed on the samples.

The final possibility is that the pn junction does not sufficently electrically isolate the active layer. This occurrence is reviewed in reference [38].

Characterization of Effects of Poor Ohmic Contacts

Since the procedure evaluation failed to find specific reasons for the contact difficulties, a characterization of the effects of these difficulties on measurements of the sheet carrier concentration, sheet resistivity and mobility for each sample was done. This included making resistivity and Hall measurements at room temperature for currents at 5, 10, 50, and 100 μA. The results of the carrier concentration measurements for the Al implanted samples are plotted in Figure IV-3 - 5. The sample identification numbers that appear in the legend of each plot are grouped in three's because samples with similar growth/implantation were annealed at three different temperatures.

Inspection of these plots reveals that the measured range of sheet concentrations for different currents is widely varying from sample to sample with no apparent dependence on anneal temperature or implantation temperature. Higher implantation doses appears to have the overall effect of increasing the measured range of concentrations. Taking the experimental percent uncertainty to be $\Delta p / p_{avg}$, we eliminate the dependence on dose and activation, and the relative percent error for each sample is evident. Employing this scheme, however, still does not result in a conclusive trend and overall the dose does not appear to have a measurable effect on the percent uncertainty.

There will be some range of measured concentrations for different currents simply because of the finite size of the contacts and the shallow implantation done. This is because fundamentally the van der Pauw equations assume true point contacts on the surface [30: 9]. This effect was seen in Hall measurements done on the high dose, p-type substrate layer on the backside of an n-type epitaxial 4H-SiC sample. The contacts on this sample were perfectly ohmic and the relative percent error from the measurements at different currents was found to be ~ 6%. Results reported by Lundberg on resistivity measurements at different currents of a highly doped p-type epitaxial 6H-SiC samples had measured uncertainties of ~ 11% [43:1562]. From this evidence, it is concluded that part of the range of the measured concentrations is entirely due to the contact size.

To evaluate the expected percent error from the contacts on the samples in this research, it was first considered that only the deposited metal was affecting the range of the measured concentrations. The samples have average sized 500 μm diameter metal contacts on them. Samples are square with an average length of 4 mm; therefore,

$l_c/l_s = .5/4 = 1/8$ which results in an estimated percent uncertainty in the Hall voltage of ~ 10% due to non-ideal contacts. Only 2 Al+ implanted samples have uncertainties < 10% and the average percent uncertainty of these room temperature measurements is found to be ~ 26%.

It was also observed that the most consistent results for the majority of the Al implanted samples occurred when passing 10 μA, the point marked on the plots for each of the samples. The 10 μA point was usually within a portion of the contact's I - V curve that was linear, which it was generally hoped would alleviate some of the problems due to rectification. This is also the current where the same Hall coefficient was measured for positive and negative magnetic fields, an expected result and indicative of sample uniformity and no rectification effects from the contacts. The error bars on the plots represents the range of measured values at different currents. Typically the highest concentration was measured at the highest current and lowest concentration for the lowest current. This does not imply that increasing current will keep increasing the carrier concentration; it only implies that we are limited by the performance of the contacts, which were more rectifying at the higher currents. The results of the room temperature measurements at different currents for the B implanted samples are given in Figure IV-6 – 8. These results are similar to the Al implanted samples; the range varies from sample to sample and again, on the average the best results were obtained when passing a current of 10 μA. The average percent uncertainty in the measurements on the B implanted samples was ~24% and only one sample had an uncertainty < 10%.

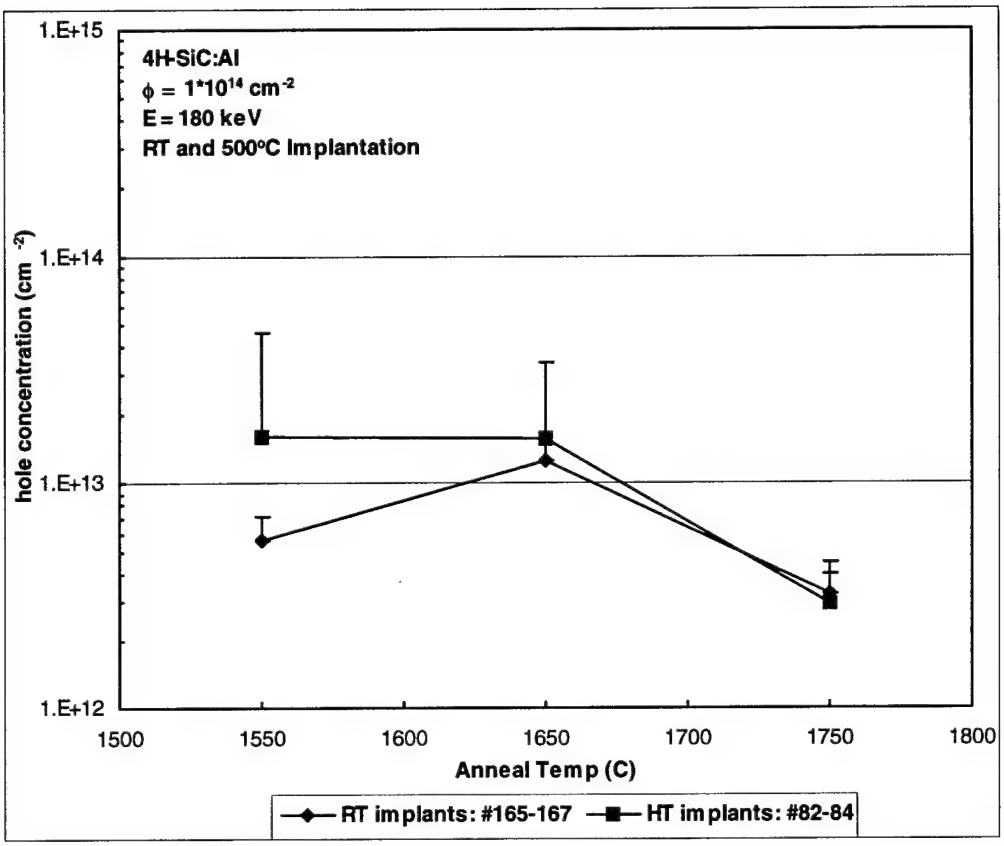

Figure IV-3. Room temperature measurements of carrier concentration at currents ranging from 5 μA to 100 μA for $1x10^{14}$ cm^{-2} Al implanted p-type 4H-SiC annealed at 1550 °C, 1650 °C and 1750 °C. Samples are implanted at 500°C or room temperature.

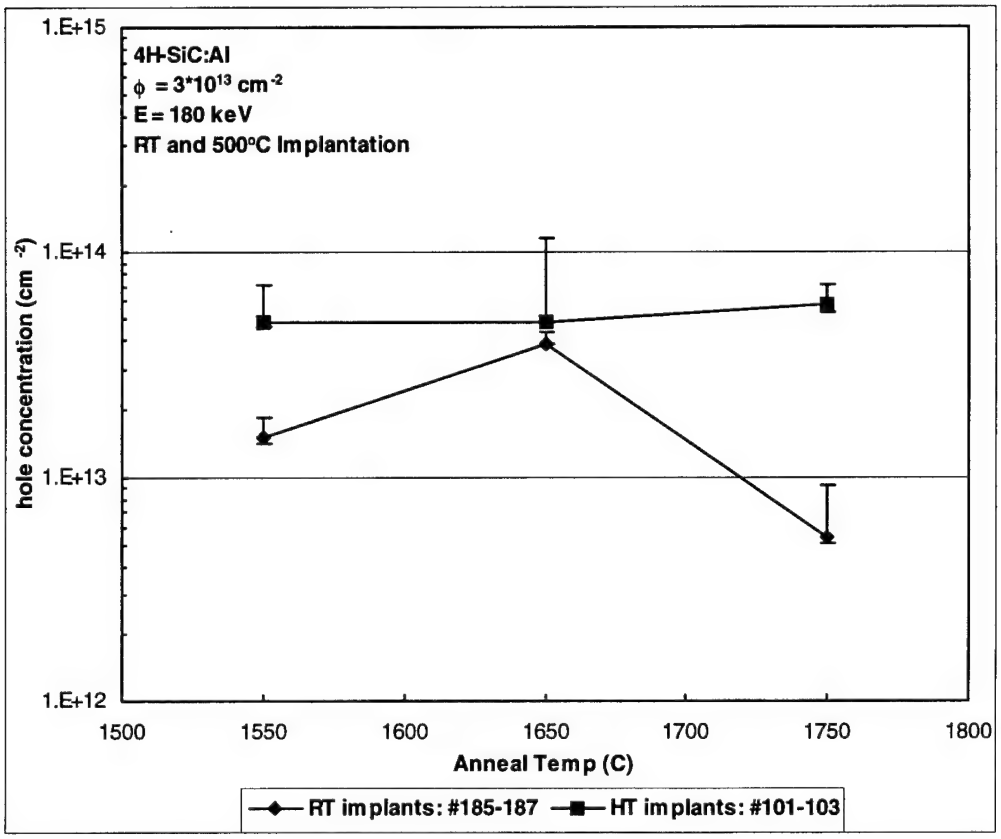

Figure IV-4. Room temperature measurements of carrier concentration at currents ranging from 5 μA to 100 μA for $3x10^{13}$ cm^{-2} Al implanted p-type 4H-SiC annealed at 1550 °C, 1650 °C and 1750 °C. Samples are implanted at 500°C or room temperature.

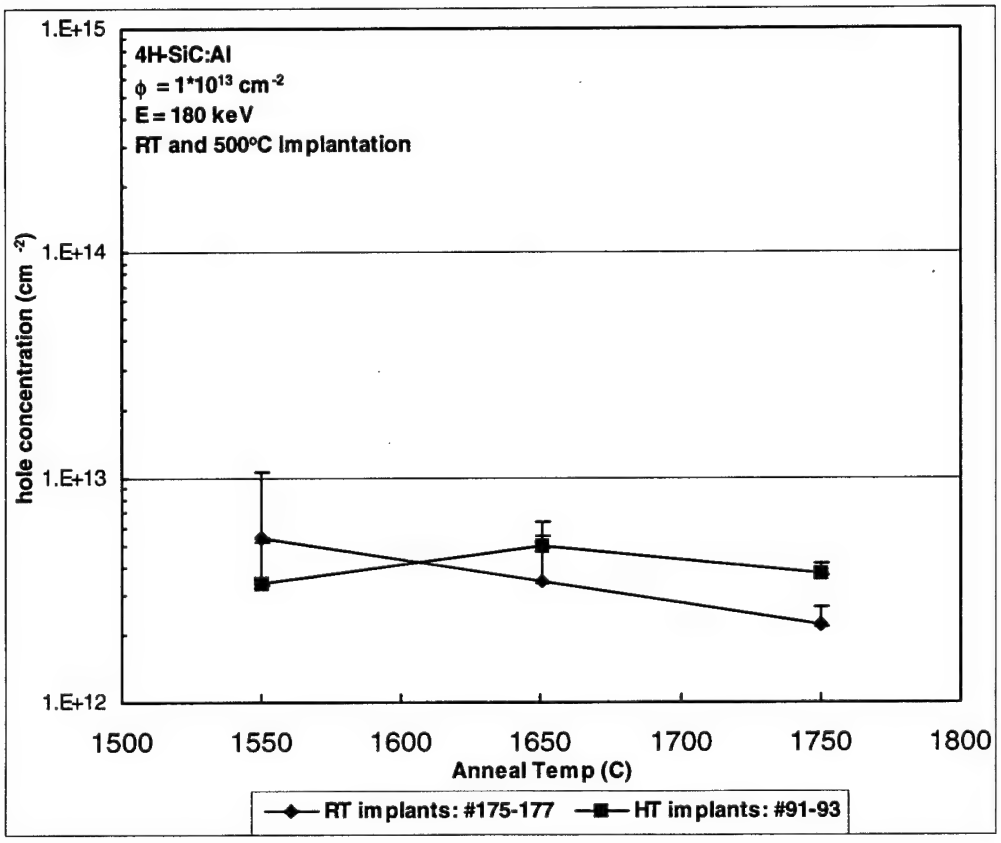

Figure IV-5. Room temperature measurements of carrier concentration at currents ranging from 5 μA to 100 μA for $1x10^{13}$ cm^{-2} Al implanted p-type 4H-SiC annealed at 1550 °C, 1650 °C and 1750 °C. Samples are implanted at 500°C or room temperature.

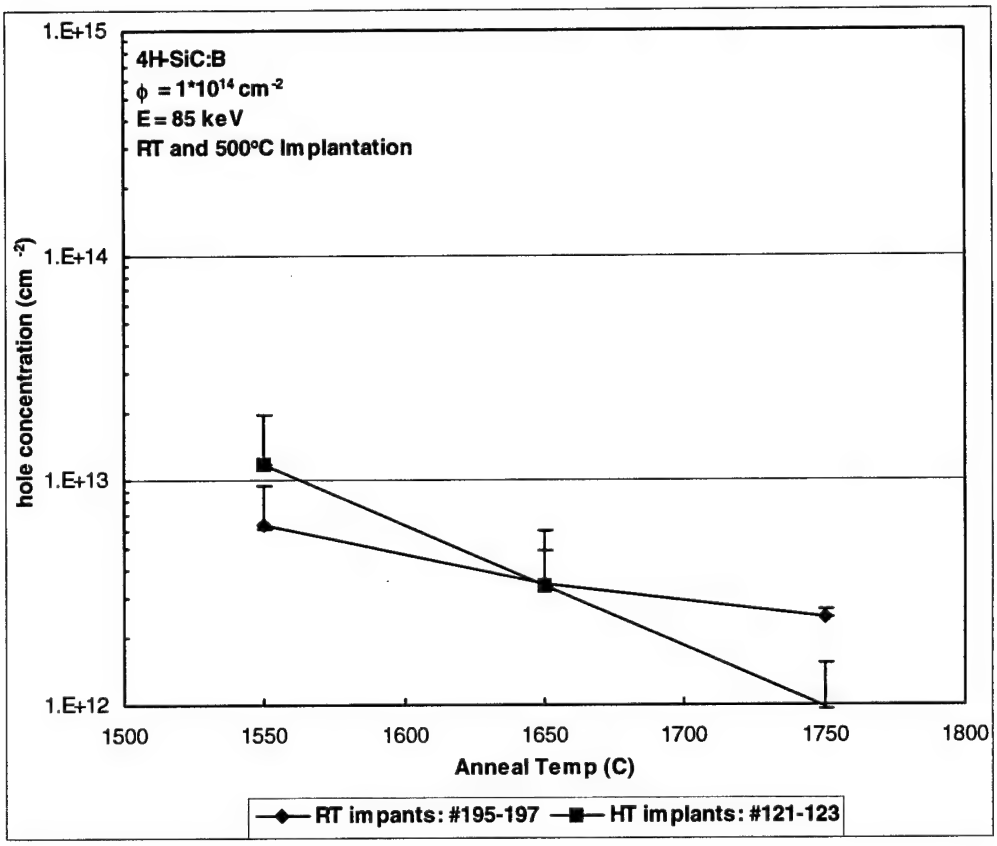

Figure IV-6. Room temperature measurements of carrier concentration at currents ranging from 5 μA to 100 μA for $1x10^{14}$ cm^{-2} B implanted p-type 4H-SiC annealed at 1550 °C, 1650 °C and 1750 °C. Samples are implanted at 500°C or room temperature.

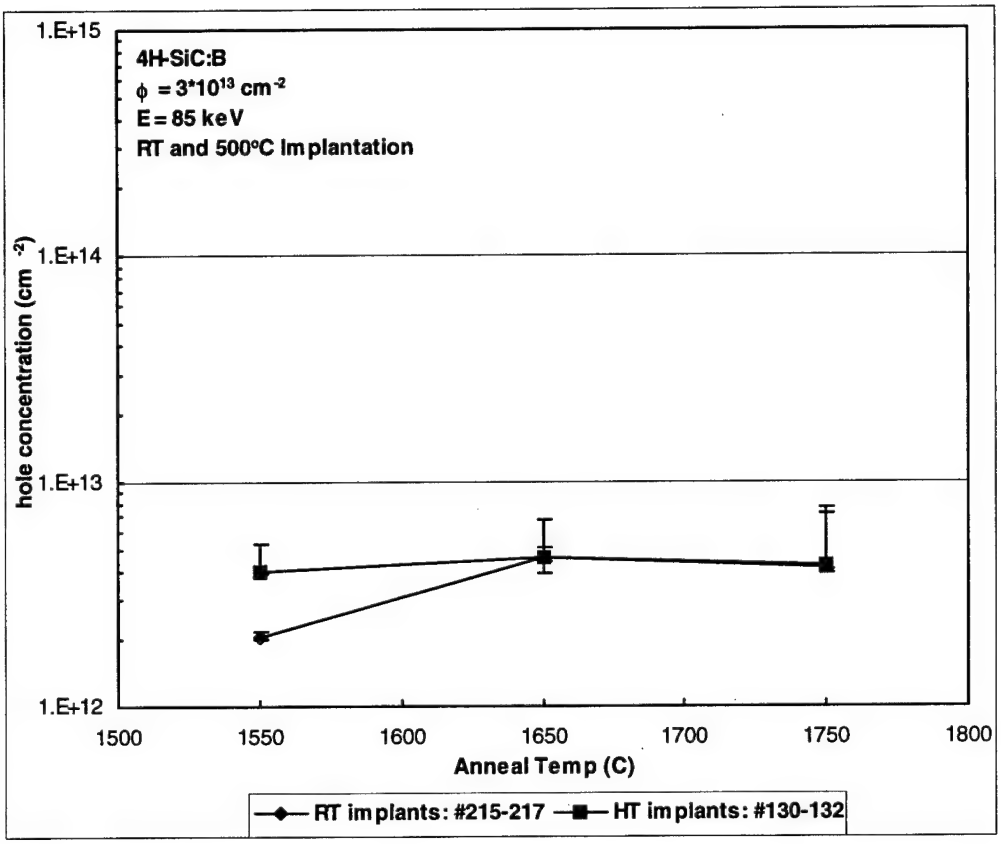

Figure IV-7. Room temperature measurements of carrier concentration at currents ranging from 5 μA to 100 μA for $3x10^{13}$ cm^{-2} B implanted p-type 4H-SiC annealed at 1550 °C, 1650 °C and 1750 °C. Samples are implanted at 500°C or room temperature.

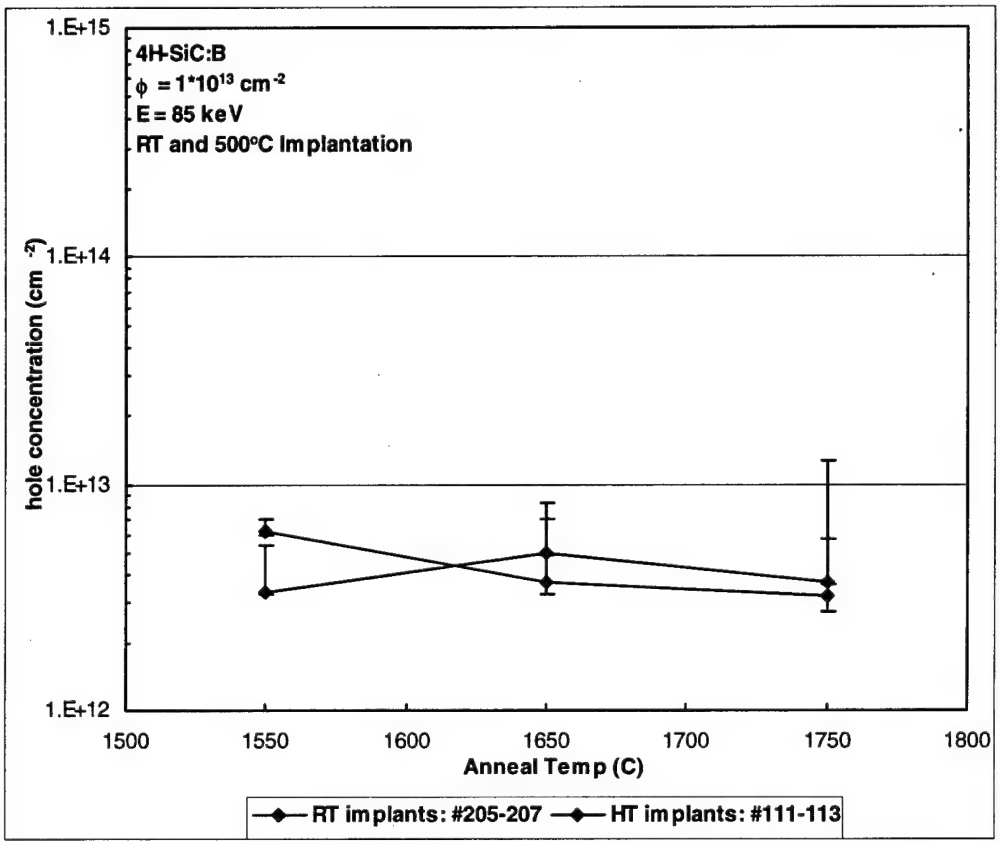

Figure IV-8. Room temperature measurements of carrier concentration at currents ranging from 5μA to 100 μA for $1x10^{13}$ cm^{-2} B implanted p-type 4H-SiC annealed at 1550 °C, 1650 °C and 1750 °C. Samples are implanted at 500°C or room temperature.

The second major difficulty encountered in this research, which is visible in this set of room temperature measurements, is that the measured carrier concentrations are too high. It is not likely that samples implanted at $3x10^{13}$ cm^{-2} would have > 100% activation at room temperature as it appears in Figure IV-4; nor is it likely that the lower dose samples have higher carrier concentrations at room temperature than samples implanted at the highest dose, $1x10^{14}$ cm^{-2}. It also unlikely that the optimum anneal temperature has some dependence on the implantation dose, as these measurements might seem to indicate.

The more likely possibility is that the sample's shallow implantation and the surface impurities and oxidation layers infusing during the annealing affect the measurements. The shallow implantation was done over too large a region of the sample area, and the measurements could be reflecting conduction from those carriers in addition to the main implanted layer. An inadequate prior cleaning of the sample surface may have resulted in contamination of the sample surfaces by infusion of impurities on the surface during the annealing. Whether these are the actual sources of this error will be expanded on in the next section where an analysis of the temperature dependent carrier concentration will be used to characterize where the carriers are coming from.

One result of the experimentation worth highlighting is the measured carrier concentration for the samples Al implanted at 500 °C with $3x10^{13}$ cm^{-2}. The carrier concentration measurements at room temperature indicate a relatively significant higher amount of carriers present in these samples. All three of these samples were repeatedly contact annealed up to 1150 °C for 5 min, which resulted in metal diffusing through the p-layer as described in the previous section, and n-type conductivity. After preparing the samples again for metallization by chemically etching the old metal contacts off and cleaning the sample, and then after putting new metal contacts on, the samples showed p-type conductivity again. The relatively higher carrier concentration present in these samples could be from conduction through the p-type and n-type layers.

When the new contacts were formed on these samples, they were positioned at the surface edges and in between the regions of shallow implantation. These contacts were of similar nature to those made in the corners of other samples. This was confirmed by observing the contacts' *I - V* curves, which showed some rectification. The room

temperature measurements shown in Figure IV-4, which reflect an extremely high acceptor concentration, were made using these side contacts. It is unusual that there was no significant difference between the quality of contacts formed on the shallow implanted regions in the corners and the contacts formed between those regions. This occurrence seems to imply that the shallow implantation may not have been carried out, but the shallow implantation area is visible to the naked eye. The region is visibly darker than the other parts of the sample, an effect caused by the implanted ions. 4H-SiC is usually transparent because the bandgap is larger in energy than visible light. The corner implantation appears to cause some increased absorption of visible light. The fact that similar contacts were made on the shallow implanted area and the area not receiving the shallow implantation does not rule out the possibility of amorphization by the shallow implanted area.

The final observation in the characterization of the metal contacts was that the final procedure found for forming the best contacts was to rigorously clean the sample before metal deposition. This process was described in Chapter 3 and required performing a chemical oxide etch on the sample using H_2SO_4: H_2O_2 (1:1) up to 1 hr followed by HF:H_2O (1:1) also for 1hr followed by a DI rinse and N_2 blow dry. This procedure removed most of the old contacts and cleaned the surface for new ones to be deposited. Newer contacts were placed next to old ones. This method was proposed since 4H-SiC is extremely resistant to any chemicals and this process will not remove the shallow implanted surface. In actuality, etching SiC requires the use of reactive plasma ions. Therefore, this procedure was only removing the possible surface contaminants. The rigorous cleaning was observed to reduce the measured concentrations on samples by up to 1 order of magnitude at room temperature, and the best contacts were formed on samples cleaned using this approach. The conclusion drawn from these observations is that some impurities, including some oxidation, were probably residing on the surface of the SiC and taking part in the conduction. It was also concluded that better contacts could be formed on the "rigorously" cleaned surfaces, a result visible in their *I* - *V* curves. The improvement in contacts was evident in the room temperature measurements because the range of concentrations measured at different currents decreased.

Conversely, it was also observed that for a few samples the new contacts made on these newly cleaned surfaces were of similar quality as the original ones made on the sample using the original cleaning routine that was taken from the literature. In these cases, the same values for room temperature concentration were also measured. This point reflects the difficulty in determining the best way to attack a problem such as forming good ohmic contacts when the focus of the research is on electrically characterizing the sample.

The purpose of this section was to review the characterization of how less-than-ideal contacts would affect the resistivity and Hall effect measurements, and as a means for deciding which samples should be ignored because of the error due to their contacts. It is also intended to provide reference for future researchers with similar difficulties. Although the plots of the room temperature measurements give the impression that the best anneal temperature corresponds to the highest measured concentration, the temperature dependent carrier concentration curves overlapped one another in some cases. Thus, it is better to inspect those plots to find which anneal temperature resulted in the highest electrical activation. These results are analyzed in the next section along with conductivity and mobility measurements.

IV-2. Resistivity and Hall Effect Measurements

This section will begin by reviewing the results of the temperature dependent resistivity and Hall effect measurements. This will include a discussion of the non-linear fitting methods used to find the parameters N_A, N_D and E_A from the free hole concentration plots. The last section mentioned that the measured carrier concentrations were in some cases much to high. This section will expand upon that discussion and also on how the poor contacts produced visible effects in the temperature dependent results.

The results of the free hole sheet-concentration, sheet-conductivity, and mobility measurements for the Al implanted samples for all three doses and both implantation temperatures are shown in Appendix A, B, and C respectively. From these plots, it is apparent that some of the samples (samples annealed at 1550 °C and 1650 °C) do not show the expected behavior; what's expected are plots similar to those in Chapter II. Comparing these plots, the results indicate that the samples annealed at 1550 °C and

1650 °C have different behavior in the freeze-out region compared to the samples annealed at 1750 °C. This is significant because the samples annealed at 1550 °C and 1650 °C were cleaned and oxide etched prior to the annealing at the same time, and during both those anneals bubbling was visible from the entire surface of those samples. Samples annealed at 1750 °C were cleaned for the annealing at a later time and bubbling was not visible from the surface of those samples during the annealing.

The most striking behavior evident in these plots is 7the magnitude of the free hole concentration, which was much higher than expected. This was also evident in the room temperature measurements. The results also do not indicate clear cut relationships between implantation parameters and resistivity, mobility and concentration. This may be attributed to the poor contacts and shallow implantation. Since the data is less than ideal, it is also difficult to correctly fit the data to the expected results because the fitting parameters become "mushy." When this occurs several acceptable fits to the data may be possible and sometimes the best fit does not give acceptable parameters. Since the samples annealed at 1750 °C show the most promising results the next two sections, which describe typical carrier concentration, mobility and resistivity measurements, will focus on those samples. Then, despite the fact that the results are mixed, the results from a comparison of all the samples will then be presented highlighting exactly what the data did indicate.

Typical Sheet-Concentration Measurements

To analyze the data the carrier concentration measurements will be fit to the dominant acceptor model, which is a p-type sample, $p >> n$. The equation for free hole concentration in the dominant acceptor model is given by the following

$$p + N_D^{\text{net}} = \frac{N_A}{1 + \frac{p}{\Phi_A}} . \tag{37}$$

The source of equation (37), the charge balance equation, was reviewed in chapter 2.

The primary method used to fit the data was a two-step, non-linear least squares computer fitting. Initially a "fit-by-eye" was attempted, but the data was apparently too

scattered to make this an effective approach. The "fit-by-eye" method is outlined by Casey [44: 2950]. This method begins with equation (37) being put in the following form

$$\frac{p(p + N_D^{net})}{(N_A - N_D^{net} - p)N_c^*} = \frac{M^{*3/2}}{g} \exp\left(\frac{-E_A}{kT}\right), \qquad (38)$$

where $N_c^* = 2(2\pi m_o k T / h^2)^{3/2}$, m_o is the electron mass, and g is the degeneracy of the acceptor level, taken to be four.

Fitting proceeds with initial guesses being made for N_D and N_A - N_D, and the plotting the natural log of the LHS of equation (38) against the reciprocal of the temperature 1/T. This plot will only be linear when the proper parameters, N_D and N_A - N_D, are entered. Then a linear fit is done on the resulting data, and the calculated slope and intercept can be used to find the activation energy and the effective mass from M^*. Therefore, this procedure also assumes a temperature independent effective mass.

An example demonstrating this approach is shown in Figure IV-9. The data being fit is the free hole concentration measurements for an Al implanted sample with a dose $3x10^{13}cm^{-2}$, which also appears in Appendix A. The plot shows different guesses for N_A - N_D, while assuming that $N_D = 10\%\ N_A$. Fitting the data using this procedure is difficult because discerning which curve is the most linear and which data points should be concentrated on is done without the benefit of uncertainty measurements. It appears from the fitting that N_A - N_D is between $1x10^{14}$ cm^{-2} and $2x10^{14}$ cm^{-2} since the data points along the edge of this range are deflecting away in opposite directions at the higher temperatures. This estimation makes sense if the actual data is consulted. Thus, while a decent estimation of N_A - N_D can be made, the point of Figure IV-9 is to demonstrate the effort involved in fitting by this manner and the lack of accuracy. To show this method's effectiveness a linear fit of the N_A - $N_D = 2x10^{14}$ cm^{-2} results was done and the acceptor energy was found to be ~ 200 ± 30 meV, which is within the range of measurements for the Al acceptor activation energy.

A non-linear least squares fitting of the same data are shown in Figure IV-10. This fitting was done using a simple, self-generated, fit routine written for use within *Mathcad,* a commercial math software application. This was a simple and relatively effective way to do a reasonable fit of the data. The fit routine was essentially in two parts; the first part was used to get an estimate of the expected activation energy, and the

second part was the full fitting to equation (37) using a typical chi-squared reduction scheme. The estimation of the activation energy was done by plotting $\ln(p / T^{3/4})$ vs. $(1/T)$ and finding the slope which equals $-E_A / 2\,k_B$. This routine approximates equation (37) in the low temperature region, with $\phi \gg N_D^{net}$ and $\phi \ll (N_A - N_D^{net})$. Therefore, this approximation is only valid for extremely small N_D^{net}, which is a reasonable assumption for these samples considering the material is a low doped ($N_A - N_D = 5\times10^{15}\ cm^{-3}$) p-type epitaxial layer. How well the fit works determines whether this assumption was correct and for most of the samples the approximation was reasonable.

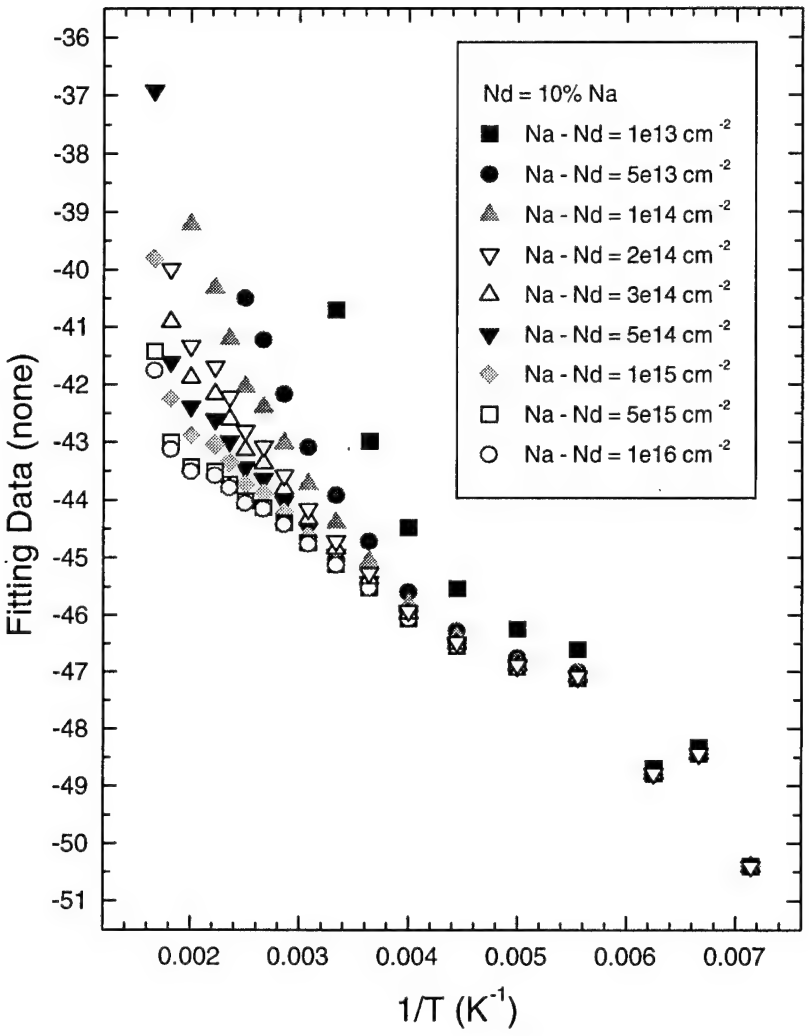

Figure IV-9. Plot of the "fit-by-eye" procedure using the dominant acceptor model. The most linear fitting appears to reside in the range of $1x10^{14}$ cm^{-2} < N_A - N_D < $2x10^{14}$ cm^{-2}. Discerning linearity within this range is difficult. For each plot N_D is assumed to be 10% N_A.

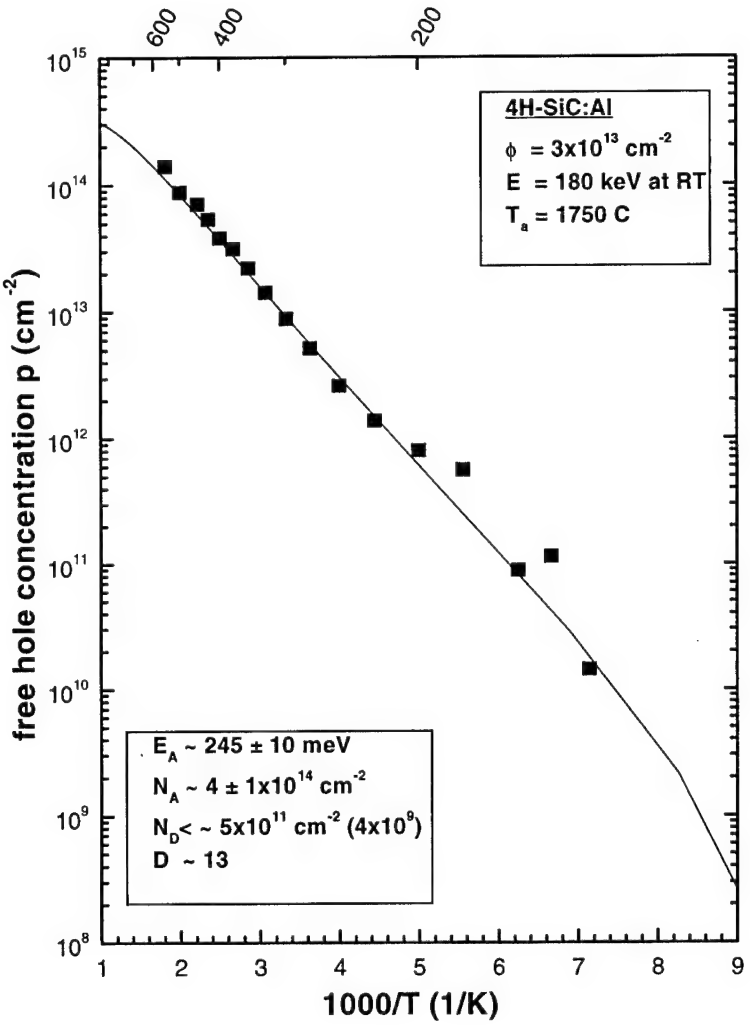

Figure IV-10. Free hole concentration measurements and fitting using dominant acceptor model. Fitting parameters are taken only as estimates of actual values. The limit on N_D is given as well as actual value used in fitting, the in parentheses.

The fit equation for the full-reduced chi-squared fitting is found by solving equation (37) for p, which results in the following expression

$$p = \frac{1}{2}(\phi + N_d^{net})\left[\left[1 + \frac{4\phi(N_A - N_d^{net})}{(\phi + N_d^{net})^2}\right]^{1/2} - 1\right] . \qquad (39)$$

The fitting routine employs a built-in function for reducing the chi-squared. This built-in function approaches the minima using a Levenberg-Marquardt solving algorithm. The uncertainty in each parameter was not calculated since a much a larger percent uncertainty is already being reflected by the room temperature measurements.

The fitting parameters from the non-linear least squares fitting are listed on the plot. The Al acceptor activation energy obtained by the fitting is close to the upper limit of the range of values quoted in Chapter II. This large magnitude of the ionization energy may be because the sample is low-doped to begin with since activation energy decreases with large impurity concentrations. The estimate given by the straight linear fitting routine was ~ 240 meV, which shows the usefulness of this two step approach; the approximation provides a good initial guess for the full reduced chi-squared fitting routine. Although this is by no means a strong fit, the results indicate a much larger than expected electrically active concentration, N_A and virtually no compensation concentration, N_d. Low compensation is also expected since the sample is low doped p-type to begin with.

The high concentration leads to a high electrical activity, N_A/N_{dose}. Electrical activity much greater than unity makes no physical sense unless you consider that there is an another possible source of carriers, the shallow implantation. The other possibilities are that other levels are contributing to the conduction, that the temperature dependent Hall scattering factor, $r(T)$, can not be neglected or possibly that the excited states of Al also need to be included in the fitting. These possibilities would normally not be able to account for such a large difference. One other possibility is that the evaluated acceptor concentrations may be enhanced by an inefficient electrical insulation of the p-n junction between the implanted p-type layer and the n-type layer. Inefficient electrical insulation was given as a reason for D >> 1 by Troffer [33,285] and an explanation is given by Schoner in [45,661]. Estimates of the uncertainty in each parameter were found

statistically, and should be considered as a lower limit since the contacts will could have a significant effect on the measurements and they are not being considered in this calculation.

This problem of measuring high concentrations was brought up in the previous section where it was seen that in some cases samples implanted with a lower dose had higher concentrations at room temperature than those implanted at the highest dose. However, the result of an electrical activity greater than 1 is not completely unusual since a similar result was reported by Troffer [33:162]. The fact that the first fitting procedure led us to think that N_A - N_D ~ $2x10^{14}$ cm^{-2} and the computer fitting showed otherwise is probably due to the incorrect choice for the compensation in that procedure. This also reflects the inherent difficulty in using that approach.

An example of a B implanted sample with the same dose and anneal temperature (1750 ^{o}C) is shown in Figure IV-11. Comparing this to the plot in Figure IV-10, the electrically active concentration, N_A, are close to one another, and the compensation is again below the limit where it is seen to affect the fitting. It is expected that the higher implanted sample would have a higher electrically active concentration. The plot for the high implanted dose makes more sense, however, since D is much closer to 1, as we would expect it to be. Comparing the low temperature regions of both plots ($T < 200$), the data points are so scattered. The scattered data could be the result of not measuring real Hall-voltage due to carrier freeze-out.

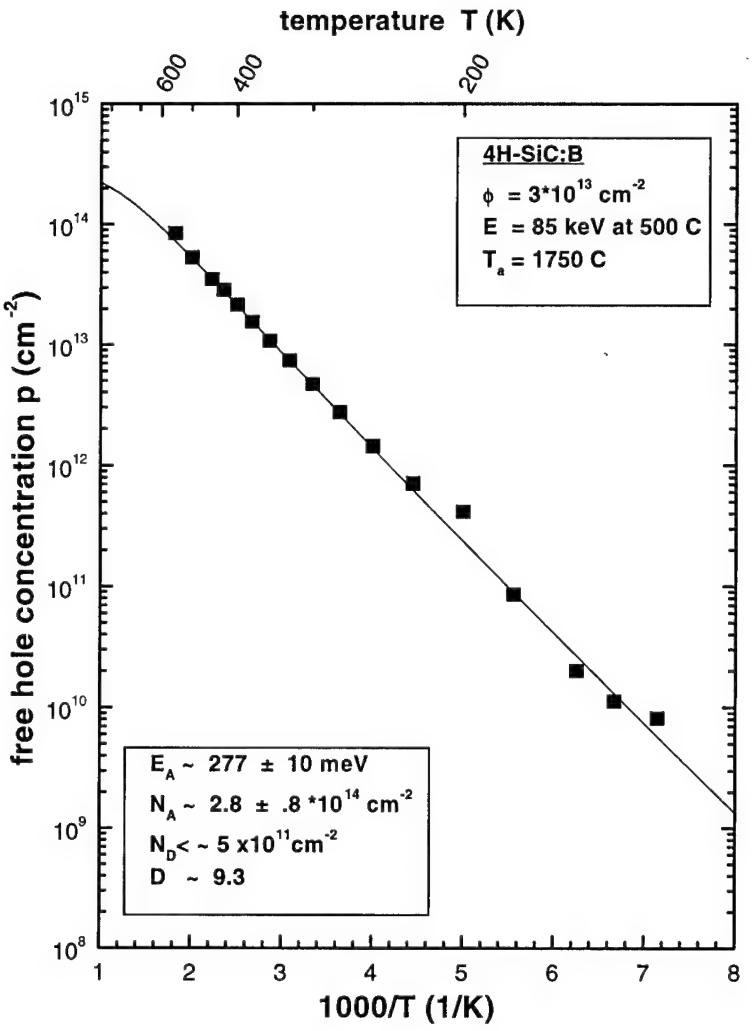

Figure IV-11. Free hole concentration measurements and fitting using dominant acceptor model. Fitting parameters are taken only estimates as of actual values. Parameter uncertainty was found statistically. A limit on N_D is given since a value <0 was given by fitting routine indicating it does not affect fitting.

These plots were presented as examples of the fitting routine that was used on all the hole concentration measurements results, which are given Appendix A. The results of the hole concentration fittings are summarized in the tables accompanying each plot. Further analysis, including a comparison to the implantation parameters and annealing temperature, is done at the end of this chapter. From the analysis of all the samples, the following results are found:

- ionization energy of Al acceptor $\Delta E(Al) = 252 \pm 20$ meV
- ionization energy of B acceptor $\Delta E(B) = 285 \pm 10$ meV
- compensation $N_D^{net} < 6.5 \times 10^{11}$ cm^{-2}

The uncertainty in these values was obtained statistically. The Al acceptor ionization is within the range of expected values (~ 185-280 meV), but slightly higher than expected. The B acceptor ionization is also within the expected range (~ 285-300 meV), but slightly lower than what was expected. Better fit results could possibly have been obtained using an acceptor model that allows for more than one species of impurities, which is the probably the case for the boron implanted samples. This would require using an algorithm that can handle the multiple acceptor solution. The fact that these ionization energies are near what was expected, however, indicates that the carriers present in the sample are from the implanted Al and B acceptors as expected.

Typical Sheet-Resistivity and Mobility Measurements

The resistivity and mobility temperature dependence for this Al implanted sample are given in Figure IV-12 and Figure IV-13. These plots show behavior similar to what is expected in this temperature regime. Ionized impurity scattering is source for the decreasing conductivity at higher temperatures. The Al implanted sample has a low temperature min resistivity of ~ 7800 $\Omega\,\square^{-1}$ and a maximum Hall mobility of ~ 73.5 cm^2 / V s at 200 K. The room temperature Hall mobility is 36 cm^2 / V s, which is exactly the same value reported by [33:285]. Room temperature resistivity for this sample was $1.94 \times 10^4\ \Omega\,\square^{-1}$. Resistivity and mobility temperature dependence for the B implanted sample is given in Figure IV-14 and Figure IV-15. This sample also shows the expected behavior. The B implanted sample has a low temperature min resistivity of ~ $1.60 \times 10^4\ \Omega\,\square^{-1}$, which is significantly higher than the Al implanted sample discussed

above (same dose). The room temperature Hall mobility for the B implanted sample is 36.6 cm^2 / V s and the maximum Hall mobility is ~ 65.7 cm^2 / V s at 225 K. Room temperature resistivity for this sample was $3.6x10^4$ Ω $\square^{-1}$. The sample resistivity and mobility data for the other samples is shown in the Appendix B and C. The next section will discuss the possible trends evident in this data.

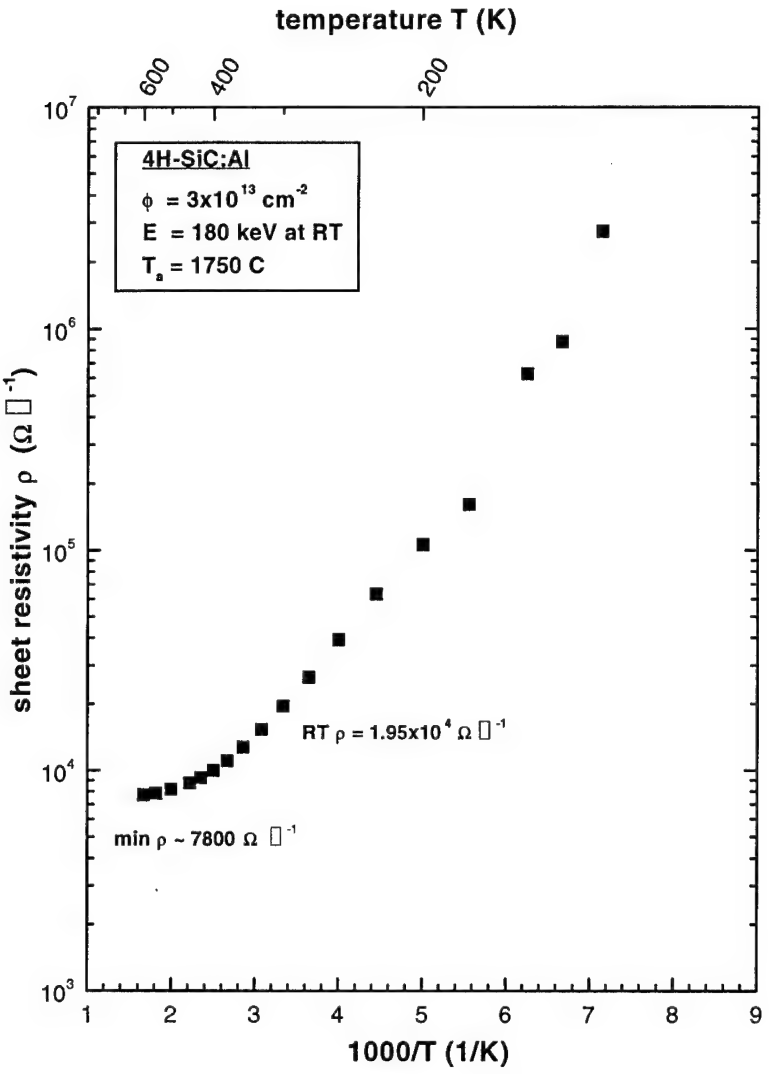

Figure IV-12. Resistivity temperature dependence for an Al implanted 4H-SiC sample at room temperature with $3x10^{13}$ cm^{-2} and annealed at 1750 °C for 30 min in Ar.

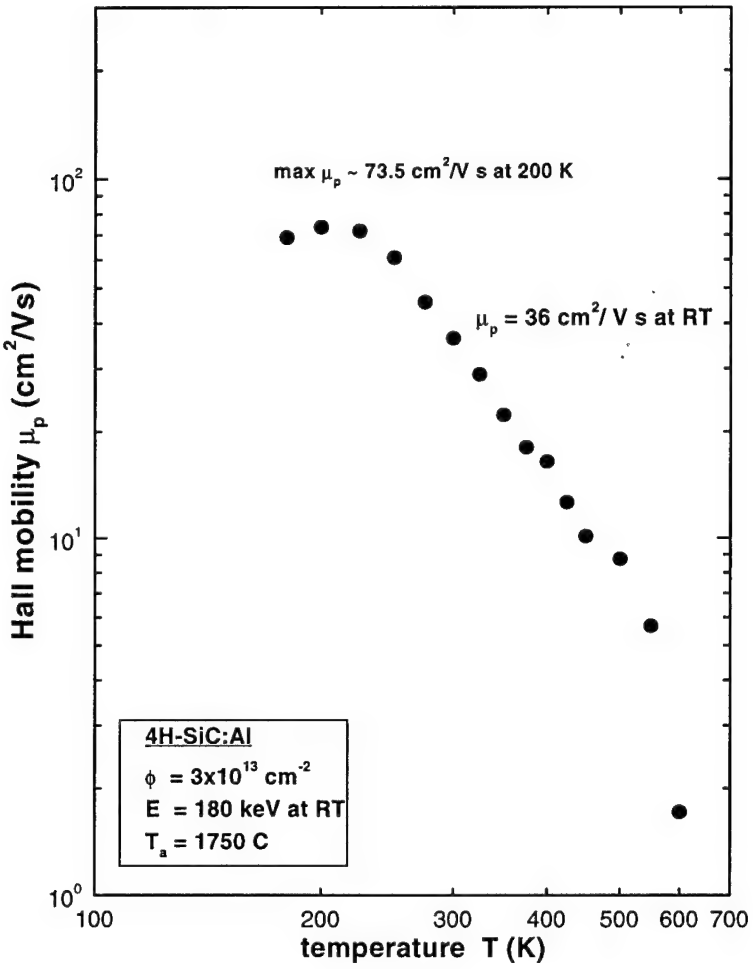

Figure IV-13. Hall mobility temperature dependence for an Al implanted 4H-SiC sample at room temperature with $3x10^{13}$ cm^{-2} and annealed at 1750 °C for 30 min in Ar.

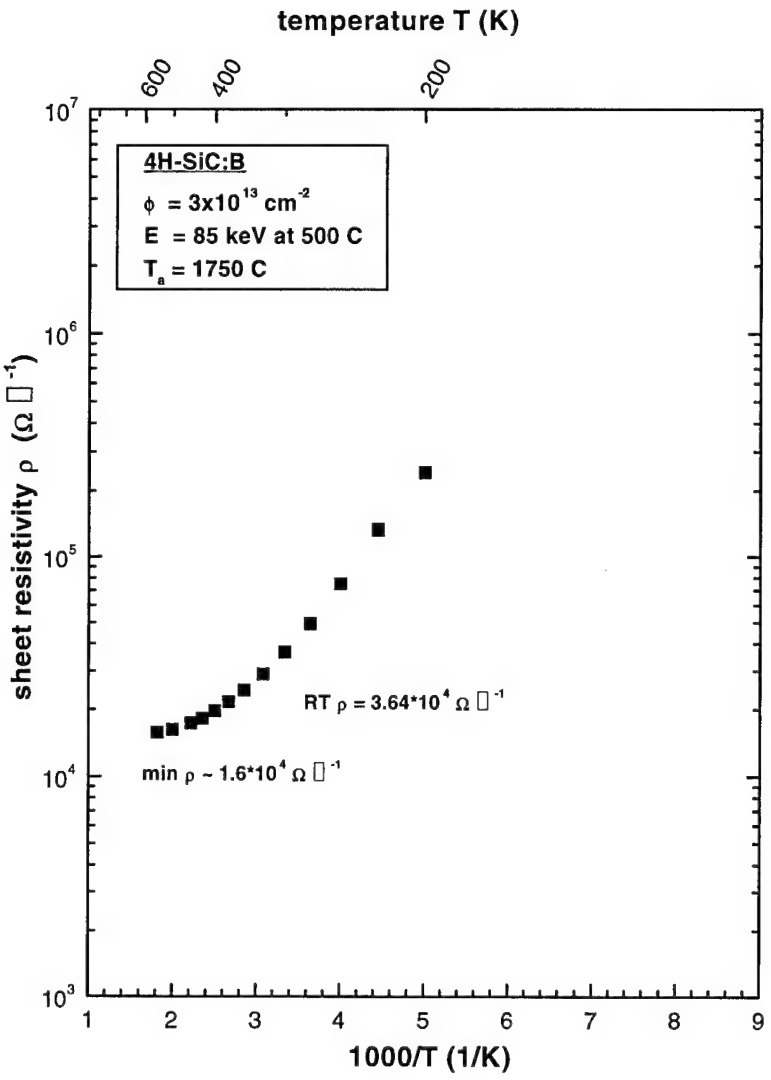

Figure IV-14. Resistivity temperature dependence for a B implanted 4H-SiC sample at 500 °C with $3x10^{13}$ cm^{-2} and annealed at 1750 °C for 30 min in Ar.

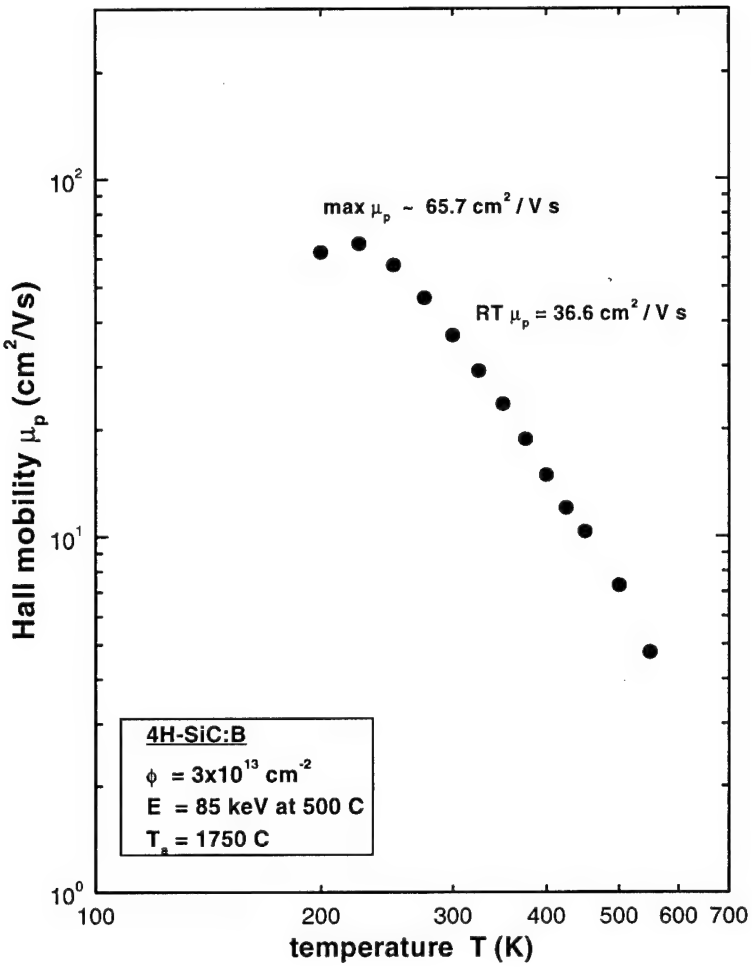

Figure IV-15. Hall mobility temperature dependence for a B implanted 4H-SiC sample at 500 °C with 3x10^{13} cm^{-2} and annealed at 1750 °C for 30 min in Ar.

Comparison of Measurements to Implantation and Annealing Parameters

Despite samples with less-than-ideal behavior and only fairly ohmic contacts an analysis can be made of the samples that were reasonably well behaved. The analysis is necessary to find the optimum implantation and annealing parameters. As a preface to this discussion though it must be understood that these samples have unique implantation geometry; a significant portion (> 50%) of each samples' surface is highly implanted (Al 50 keV) in the corners in addition to the main implantation. It must also understood that cleaning complications and poor contacts may be affecting the data as well. This comparison will evaluate the differences in transport properties in samples implanted at different doses, annealed at different temperatures, and implanted at different temperatures for both Al and B implanted samples.

Plots of the sheet-resistivity, mobility, and carrier concentration measurements of Al implanted samples annealed at 1750 °C and implanted at three different doses are shown in Figure IV-16, Figure IV-17, and Figure IV-18, respectively. This comparison is done to find the effects of implantation dose. The plot of the resistivity indicates that the lowest resistivity (~ 7250 $\Omega\,\square^{-1}$) is measured for a sample implanted at the highest dose, but also that the sample implanted at the middle fluence has the lowest resistivity on average over the entire temperature range (200 - 600 K). From this plot it is also apparent that curves for each sample are slightly different shaped, but have roughly the same slope. The average trend for all the Al implanted samples was similar to the trend here; a dose of $\phi = 3x10^{13}$ cm^{-2} resulted in the lowest resistivity (Appendix B).

The highest mobility is measured for the sample implanted at the lowest dose (μ_H ~ 200 cm^2 / V s at 175 K), as indicated in Figure IV-17. The sample implanted at the highest dose, however, has the highest mobility on average over the entire temperature range (200 - 600 K). Maximum mobility for each sample occurs at different temperatures but centers on ~ 200 K. The data at temperatures below where the peaks occur, T < 175 K, appears too scattered to be significant and is ignored. While mobility is dependent on the presence of point defects resulting from the implantation, the presence of ionized impurity and lattice phonon scattering is what causes the mobility to decrease with temperature. The other sample data, on average, also indicates the highest mobility for samples implanted at $1x10^{13}$ cm^{-2} (Appendix C).

The carrier concentration plots, Figure IV-18, indicate that the highest activation was found for samples implanted at the middle dose, which is a completely unexpected result. The high implantation dose was expected to result in the highest concentration. Why this occurred is not understood, but considering the ill success encountered with forming contacts, cleaning and the high concentration shallow implantation the result is not an impossibility. The same shallow implantation was done on all the samples, but since the effects of the different implantation's on each other is not known the shallow implantation must be considered as a possible reason for the middle fluence resulting in the highest acceptor concentrations. The fit parameters are given in the accompanying table, Table IV-1. This tables shows ionization energies ranging from 250 - 274 meV; although these are relatively high for the Al acceptor they are within the range of published values. Considering the other Al implanted samples, on average they also indicate a dose of $3x10^{13}$ cm^{-2} results in the highest carrier concentrations. The carrier concentration plot also confirms that ionized impurity scattering is responsible for the mobility data because the sample with the highest activation had the lowest mobility.

Plots of the sheet-resistivity, mobility and carrier concentration for B implanted samples at the different doses are given in Figure IV-19, Figure IV-20, and Figure IV-21. These results indicate that the B implanted samples have a roughly similar dependence on dose as the Al implanted samples. For these samples, the lowest resistivity is measured for the sample implanted at the middle dose ($\phi = 3x10^{13}$ cm^{-2}). The minimum value of sheet resistivity (~ 6820 Ω $\square^{-1}$) found is lower, but relatively close to the minimum resistivity from the Al implanted samples. The overall results from all the sample data shown in Appendix B concurs with this data, indicating the middle dose results in the lowest resistivity.

For the B implanted samples the highest mobility (μ_H ~ 150 cm^2 / V s at 180 K) is again measured for the samples implanted with the lowest dose ($\phi = 1x10^{13}$ cm^{-2}), as was the case for the Al implanted samples. The results below 175 K are again ignored. These results indicate that ionized impurity and lattice phonon scattering are the primary scattering mechanisms in the samples. The lowest implantation dose, as was expected, results in a lower concentration of electrically active acceptors, which results in lower ionized impurity scattering and higher mobility.

In comparison to the Al implanted samples the highest carrier concentration is also found for samples implanted at the middle dose as shown in Figure IV-21. The fit parameters from these samples show ionization energies ranging from 273-300 meV, which are on the low end of the reported values for B acceptors, but within the published range of values. The reason these values are low could possibly be due to the fact that a significant number of Al carriers are also present in the sample and the effects of the different species can not be resolved.

From this comparison the dependence of the transport properties on dose has been shown. An implantation dose of $3x10^{13}$ cm^{-2}, unexpectedly, resulted in the highest carrier concentration for both Al and B implantation. It has also been shown that the primary scattering mechanisms in the samples are ionized impurity and lattice phonon scattering. The resistivity is also seen to be dependent on the carrier concentration present since samples with the highest concentration had the lowest minimum resistivity. In the next section a similar analysis will be done comparing the transport properties of samples implanted at one dose and annealed at the three different temperatures.

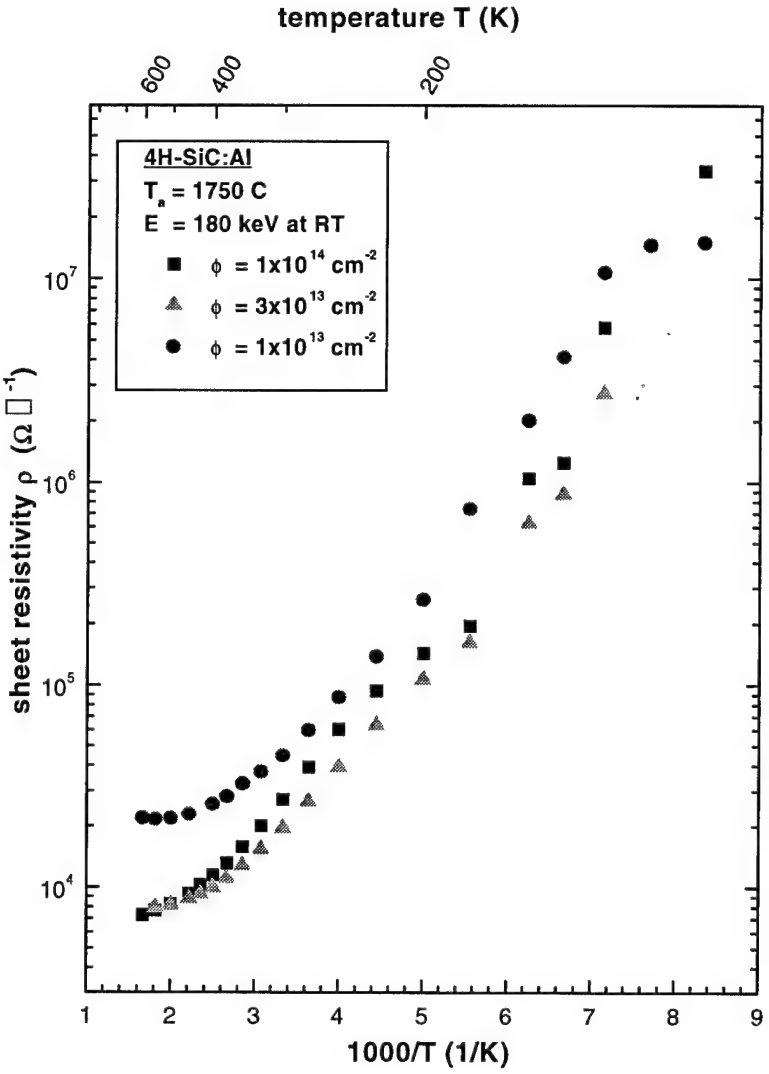

Figure IV-16. Resistivity temperature dependence for 4H-SiC samples annealed at 1750 °C and Al implanted at 3 different doses. The lowest resistivity is measured for samples implanted at the highest dose, but the middle dose sample is the lowest on average over this temperature range.

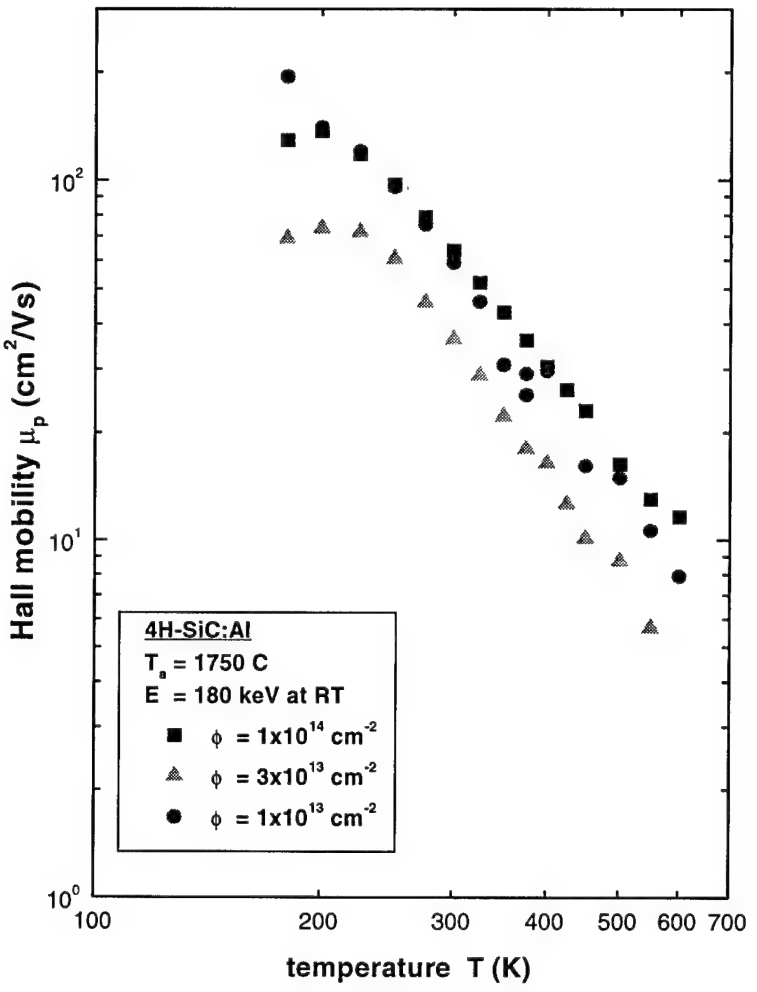

Figure IV-17. Hall mobility temperature dependence for 4H-SiC samples annealed at 1750 °C and Al implanted at 3 different doses. On average, the highest mobility is measured for samples implanted at the lowest dose.

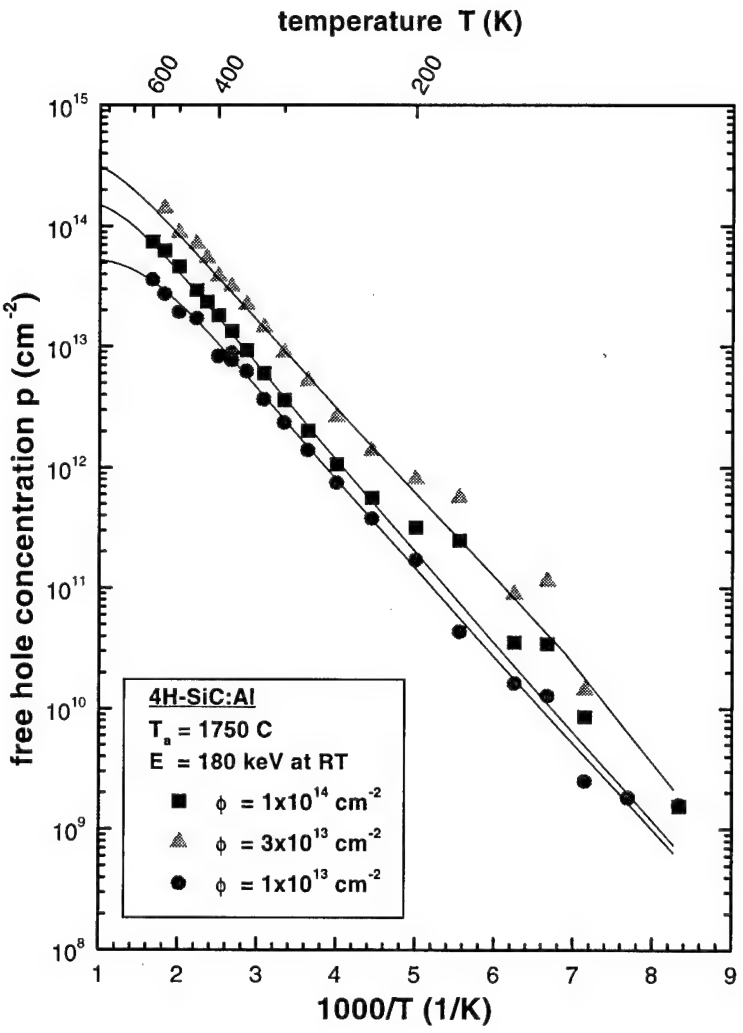

Figure IV-18. Carrier concentration temperature dependence for 4H-SiC samples annealed at 1750 °C and Al implanted at 3 different doses. On average, the highest carrier concentration is measured for samples implanted at the middle dose.

Table IV-1. Fit parameters of the carrier concentration plots in Figure IV-18.

ion	dose (cm^{-2})	Anneal temp T_a (°C)	acceptor sheet concentration N_A (10^{14} cm^{-2})	Activation energy E_A (meV)	electrical activity D
Al	1x10^{14} (RT)	1750	1.8 ± .5	274 ± 6	1.8
Al	3x10^{13} (RT)	1750	3.9 ± .6	249 ± 6	13
Al	1x10^{13} (RT)	1750	.6 ± .2	260 ± 10	5.5

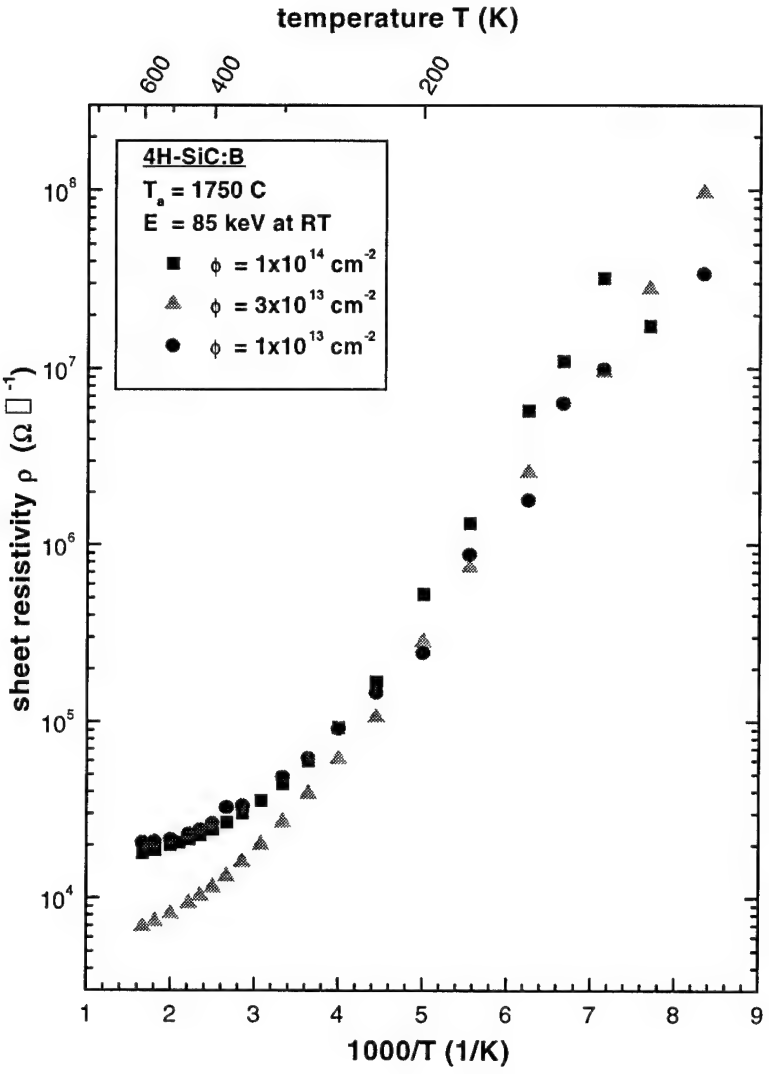

Figure IV-19. Resistivity temperature dependence for 4H-SiC samples annealed at 1750 °C and B implanted at 3 different doses. The lowest resistivity is measured for samples implanted at the middle dose.

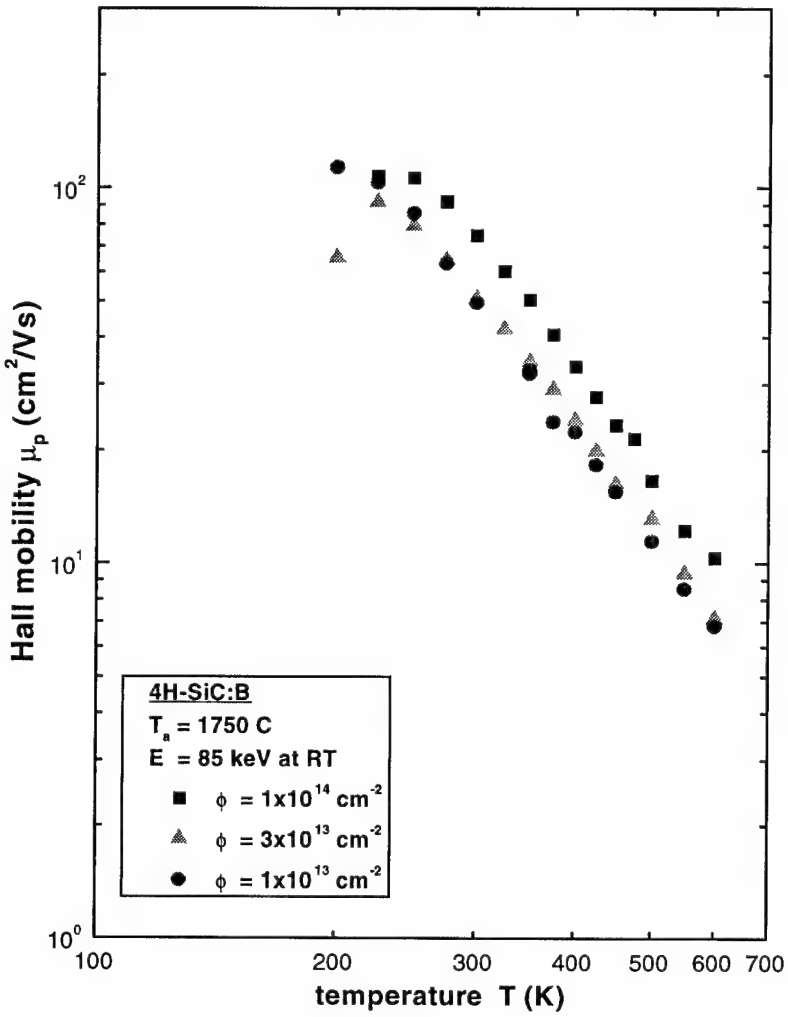

Figure IV-20. Hall mobility temperature dependence for 4H-SiC samples annealed at 1750 °C and B implanted at 3 different doses. The highest mobility is measured for samples implanted at the lowest dose. Results below 175°C are ignored.

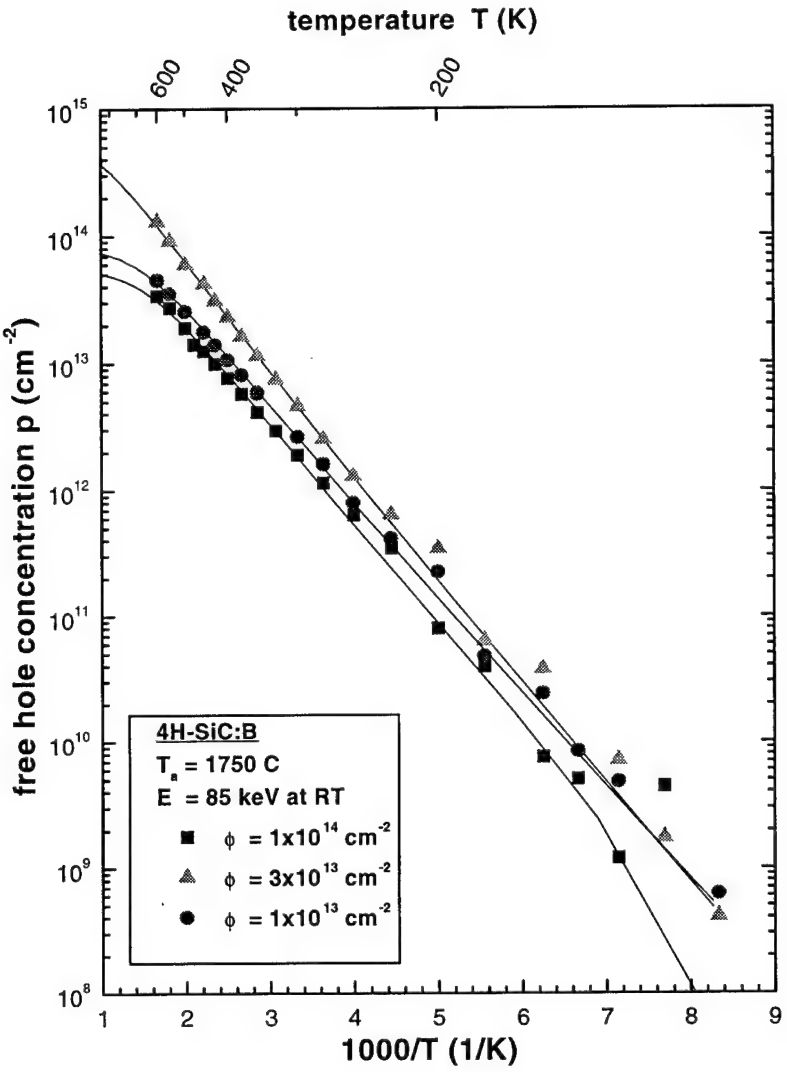

Figure IV-21. Carrier concentration temperature dependence for 4H-SiC samples annealed at 1750 °C and B implanted at 3 different doses. On average, the highest carrier concentration is measured for samples implanted at the middle dose.

Table IV-2. Fit parameters of the carrier concentration plots in Figure IV-21.

ion	dose (cm^{-2})	Anneal temp T_a (°C)	acceptor sheet concentration N_A (10^{14} cm^{-2})	Activation energy E_A (meV)	electrical activity D
B	$1x10^{14}$ (RT)	1750	.53 ± .09	281 ± 7	.53
B	$3x10^{13}$ (RT)	1750	6.6 ± 1.0	300 ± 5	22
B	$1x10^{13}$ (RT)	1750	.8 ± .1	273 ± 6	8.0

Plots of the transport properties for a comparison of one Al implantation dose ($\phi = 1x10^{14}$ cm^{-2} at 300 K) at the three anneal temperatures are given in Figure IV-22, Figure IV-23, and Figure IV-24 in order to find the optimum anneal temperature. The plot of the sheet resistivity temperature dependence, Figure IV-22, indicates that the lowest resistivity (~ 5500 $\Omega\,\square^{-1}$) is measured for samples annealed at 1650 °C. On average this was the case for all the Al implanted samples.

The plot of the mobility temperature dependence for the Al implanted samples annealed at 3 different temperatures, Figure IV-23, indicates annealing at 1750 °C results in the highest mobility of the three anneal temperatures. Annealing at this temperature led to a maximum mobility of μ_H ~ 137 cm^2/ V s at 200 K and a RT mobility of μ_H = 63 cm^2 / V s, which is significantly higher than the average value, ~ 36 cm^2 / V s. The samples annealed at 1650 °C show the lowest mobility. It has a RT mobility of ~ 29.4 cm^2 / V s, which is close to the average values seen in the literature.

The optimum annealing temperature indicated by the plot of the carrier concentration temperature dependence, Figure IV-24, is 1650 °C. This is significantly lower than the value seen in the literature, which indicate an optimum annealing temperature of ~ 1800 °C. The samples in this research, however, were not implanted in the same manner as those in the literature; they have had one main implantation of Al or B at either of three different doses and a shallow corner Al implantation at one dose significantly higher than the others. The fitting parameters for the curves in this plot are given in Table IV-3. The values found for activation energy are within the published range for the Al acceptor, which was reviewed in Chapter II. Considering all the Al implanted samples, annealing at 1650 °C resulted on average in the highest carrier concentrations. Thus, the optimum anneal temperature for Al implantation is taken as ~ 1650 °C.

The same comparison is done for B implantation in order to find the optimum anneal temperature for that ion species. Figure IV-25, Figure IV-26, and Figure IV-27 are plots of the transport properties for a samples at one implantation dose (ϕ = $1x10^{14}$ cm^{-2} at 300 K) annealed at three different temperatures. The plot of the resistivity temperature dependence shows that the lowest resistivity was measured for samples annealed at 1550 °C. This sample has a minimum resistivity of ~ 5100 $\Omega\,\square^{-1}$. Although

this value is lower than the value for the Al implanted samples, on the average it was found that higher resistivity was measured in the B implanted samples. This is evident in the plots of resistivity in Appendix B.

Figure IV-26 is the plot of the mobility temperature dependence for the samples annealed at the 3 different temperatures. These plots indicate that annealing at 1750 °C, resulted in a maximum mobility of ~ 100 cm^2 / V s at 200 K. Room temperature mobility for this sample was measured to be 74 cm^2 / V s, which is again above the average quoted values. As this plot indicates, the temperature where the maximum mobility occurs is dependent on the anneal temperature, which indicates the mobility is dependent on the concentration of electrically active acceptors. Samples annealed at 1550 °C had on average the lowest mobility over the entire temperature range.

Finally, Figure IV-27 shows the plots of the carrier concentration dependence on the anneal temperature. For these B implanted samples, annealing at 1550 °C results in the highest concentration of electrically active carriers. This was also the average result for all the B implanted samples. The fitting parameters for this plot are given in Table IV-4. These values for the ionization energy are lower than was expected, but within the published range of values. The fitting curves also reflect a less than ideal fitting, which might be the result of the presence of a significant number of carriers from the shallow implanted Al acceptors. The results in the literature have indicated that 1720 °C is the optimum anneal temperature for B implantation, which is again much higher than the optimum anneal temperature found in this research.

From these comparisons it is evident that the optimum anneal temperatures for implanted Al ions is 1650 °C and 1750 °C, and for implanted B ions it is roughly between 1550 °C and 1650 °C. Annealing in between these ranges appears should on average result in a combination of high concentration, high mobility, and low resistivity. These results are significantly different compared to the work presented in the Chapter II, which indicated optimum anneal temperatures of 1800 °C and 1720 °C for Al and B implanted ions respectively [33]. This difference can only be attributed to the difference in sample preparation and specifically the addition of the shallow implantation.

The research by Troffer also indicated the same result of activation efficiency > 100%. Those samples did not, however, have a shallow high implantation, as did the

samples in this research. Thus, the fact that the samples in the research were found to have activation greater than 100% is not an unexpected result considering that this same result was seen in samples that only had one main implantation.

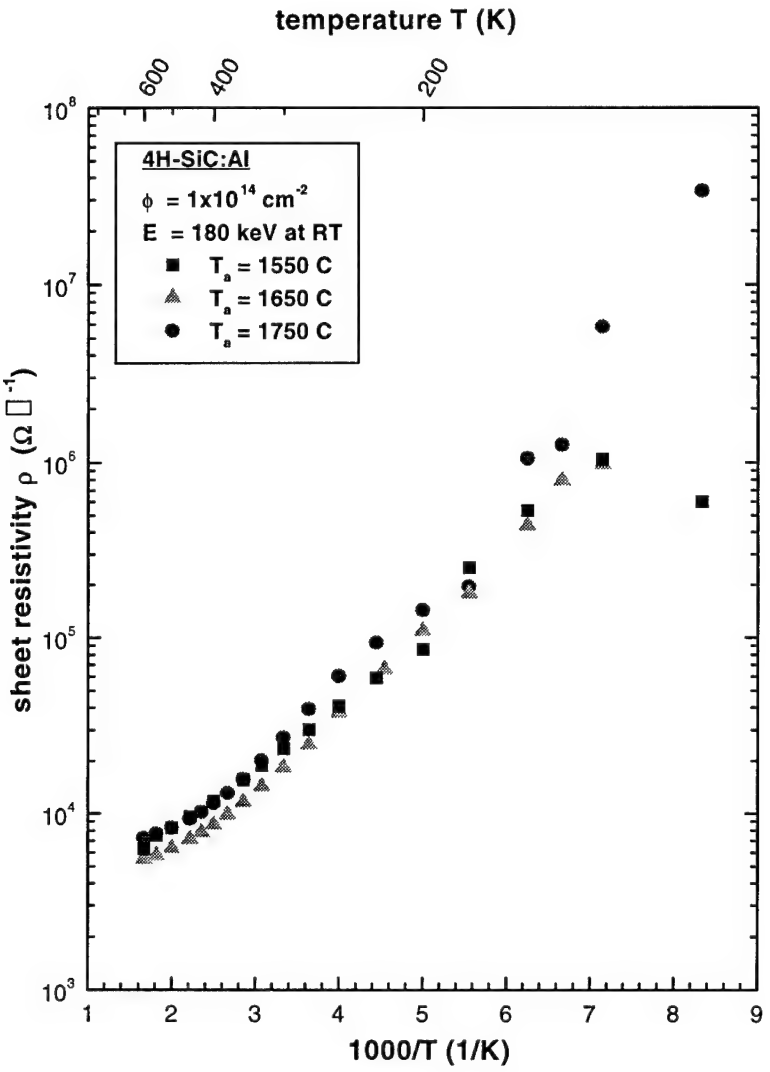

Figure IV-22. Resistivity temperature dependence for Al implanted 4H-SiC samples at room temperature with $1x10^{14}$ cm^{-2} and annealed at 3 different temperatures. The lowest resistivity is measured for samples annealed at 1650 °C.

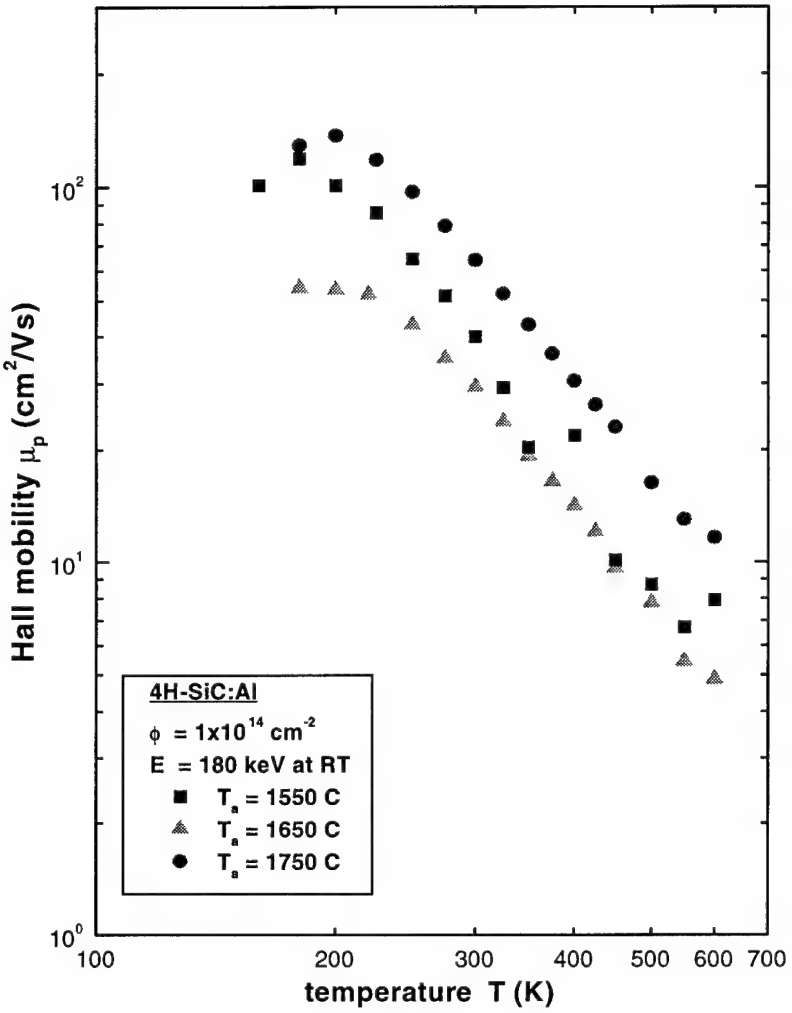

Figure IV-23. Hall mobility temperature dependence for Al implanted 4H-SiC samples at room temperature with 1x10^{14} cm^{-2} and annealed at 3 different temperatures. On average, the highest mobility is measured for samples annealed at 1750 °C.

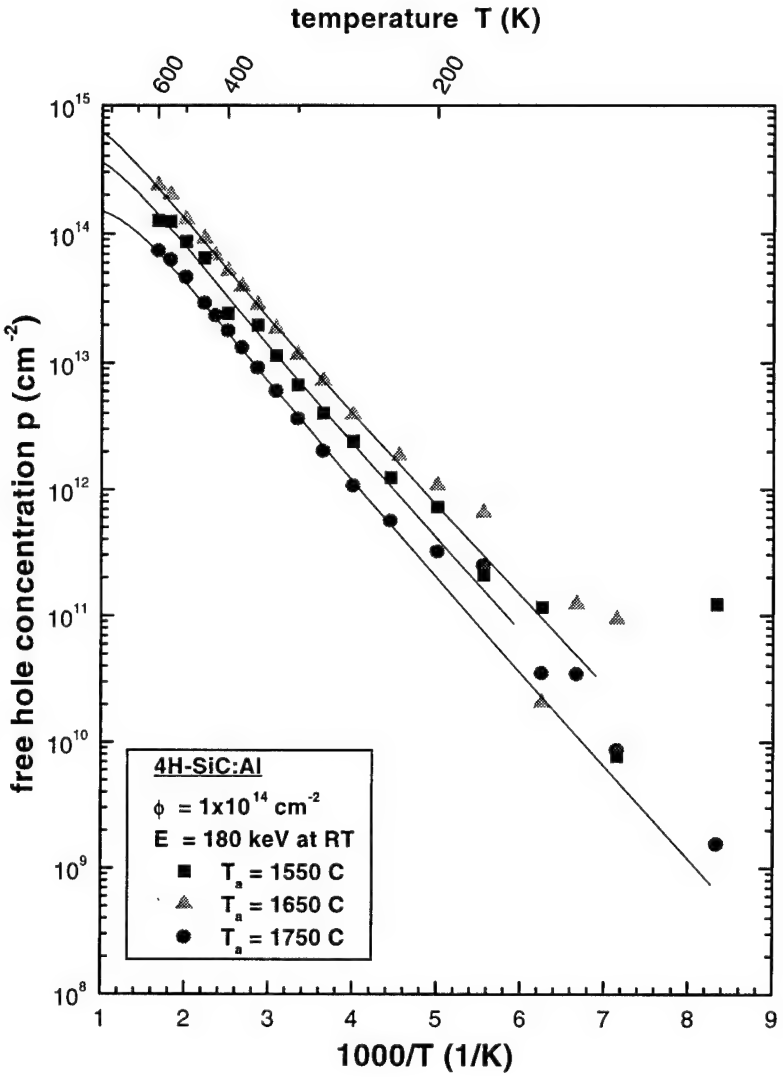

Figure IV-24. Carrier concentration temperature dependence for Al implanted 4H-SiC samples at room temperature with 1x10^{14} cm^{-2} and annealed at 3 different temperatures. On average, the highest carrier concentration is measured for samples annealed at 1650 °C.

Table IV-3. Fit parameters of the carrier concentration plots in Figure IV-21.

ion	dose (cm^{-2})	Anneal temp T_a (°C)	acceptor sheet concentration N_A (10^{14} cm^{-2})	activation energy E_A (meV)	electrical activity D
Al	1x10^{14} (RT)	1550	4.9 ± 1.6	267 ± 7	4.9
Al	1x10^{14} (RT)	1650	9.9 ± 2.8	258 ± 8	9.9
Al	1x10^{14} (RT)	1750	1.8 ± .5	274 ± 6	1.8

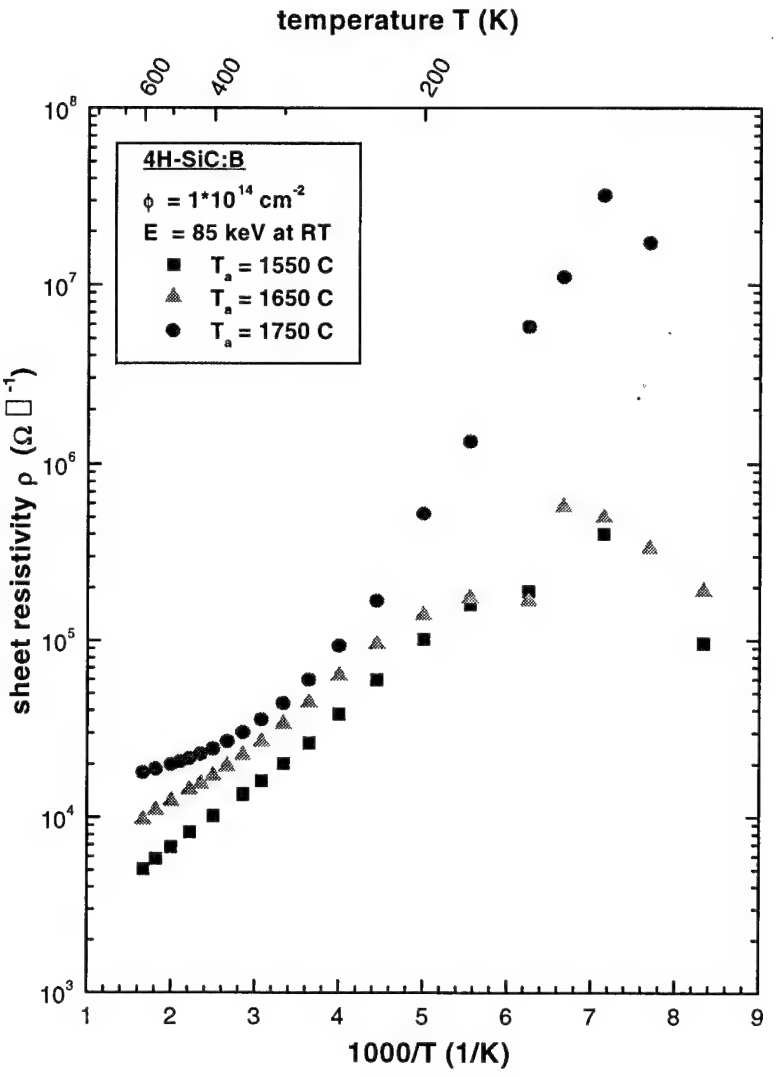

Figure IV-25. Resistivity temperature dependence for 4H-SiC samples B implanted at $\phi = 1x10^{14}$ cm^{-2} and annealed at 3 different temperatures. The lowest resistivity is measured for samples annealed at 1550 °C. This was also the average result for all the B implanted samples.

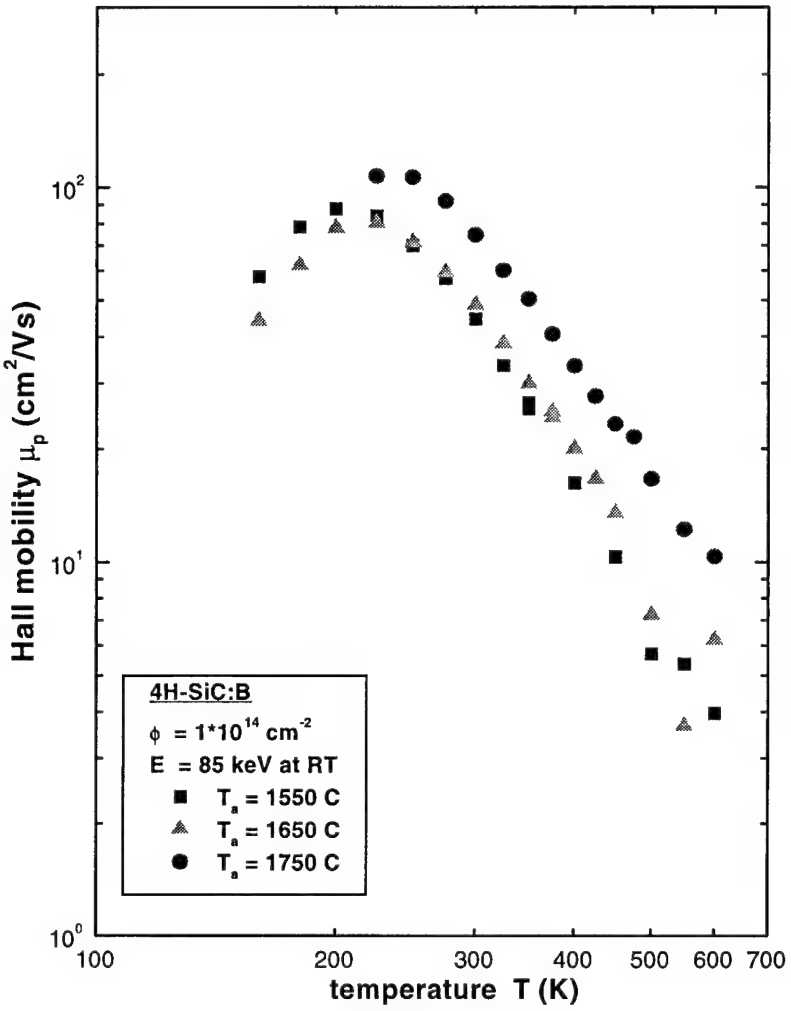

Figure IV-26. Hall mobility temperature dependence for 4H-SiC samples Al implanted at $\phi = 1x10^{14}$ cm^{-2} and annealed at 3 different temperatures. On average, the highest mobility is measured for samples annealed at 1750 °C.

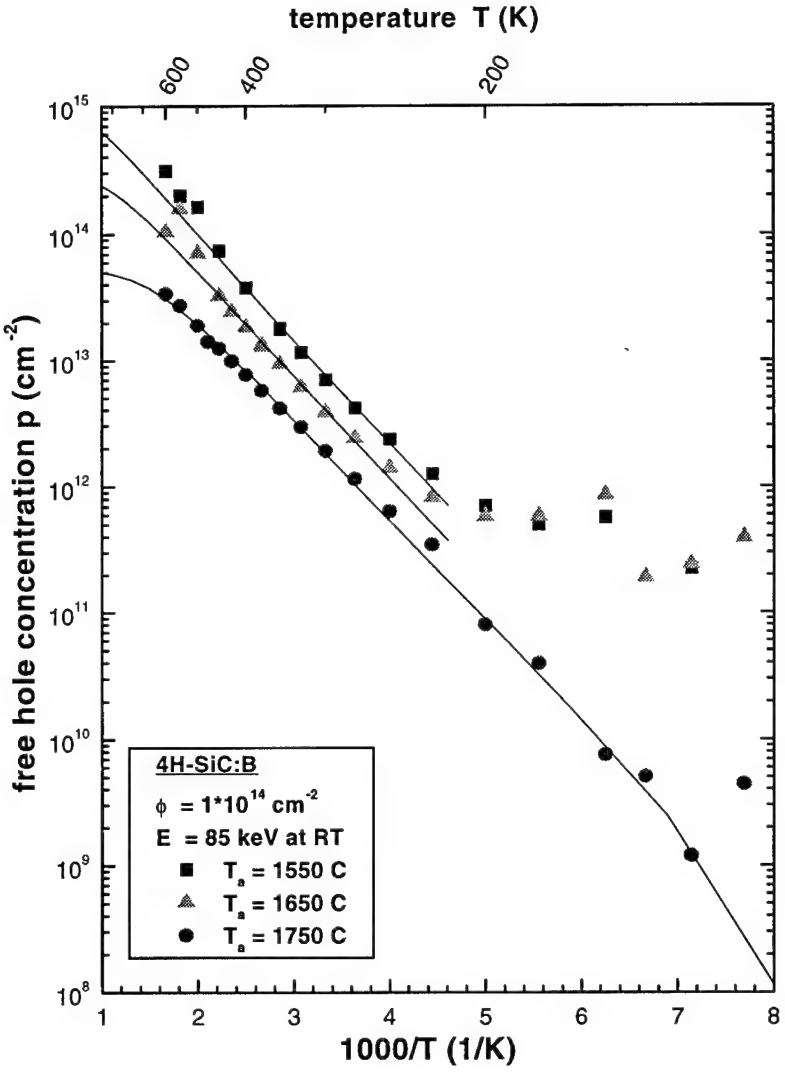

Figure IV-27. Carrier concentration temperature dependence for 4H-SiC samples Al implanted at $\phi = 1x10^{14}$ cm^{-2} and annealed at 3 different temperatures. The highest carrier concentration is measured for samples annealed at 1550 °C, which was the average result for all the samples.

Table IV-4. Fit parameters of the carrier concentration plots in Figure IV-21.

ion	dose (cm^{-2})	Anneal temp T_a (°C)	acceptor sheet concentration N_A (10^{14} cm^{-2})	activation energy E_A (meV)	electrical activity D
B	$1x10^{14}$ (RT)	1550	12 +- 4	281 +- 7	12
B	$1x10^{14}$ (RT)	1650	3.2 +- .6	287 +- 9	3.2
B	$1x10^{14}$ (RT)	1750	.53 + .09	281 +- 7	.53

A comparison of the room temperature implanted samples compared to the high temperature implanted samples revealed no significant difference in the material properties between these samples. This is evident in the plots in Figure IV-28, Figure IV-29, and Figure IV-30. These plots indicate higher activation and lower resistivity for the samples implanted at higher temperatures, but there is no observable difference in the mobility plots, which indicates that in-situ annealing was not occurring. Other Al implanted samples indicated similar findings; that implantation at 500 ^{o}C did not significantly increase mobility and carrier concentration. The B implanted sample data reflected the same conclusion. This data is shown in Appendix A and C. Thus, the overall results indicate that no gain was achieved with high temperature implantation at 500 ^{o}C. Other research has indicated that implantation at T > 850 ^{o}C results in higher activation for B implantation. Therefore, it is suggested that hot implantation is still a reasonable possibility for future research.

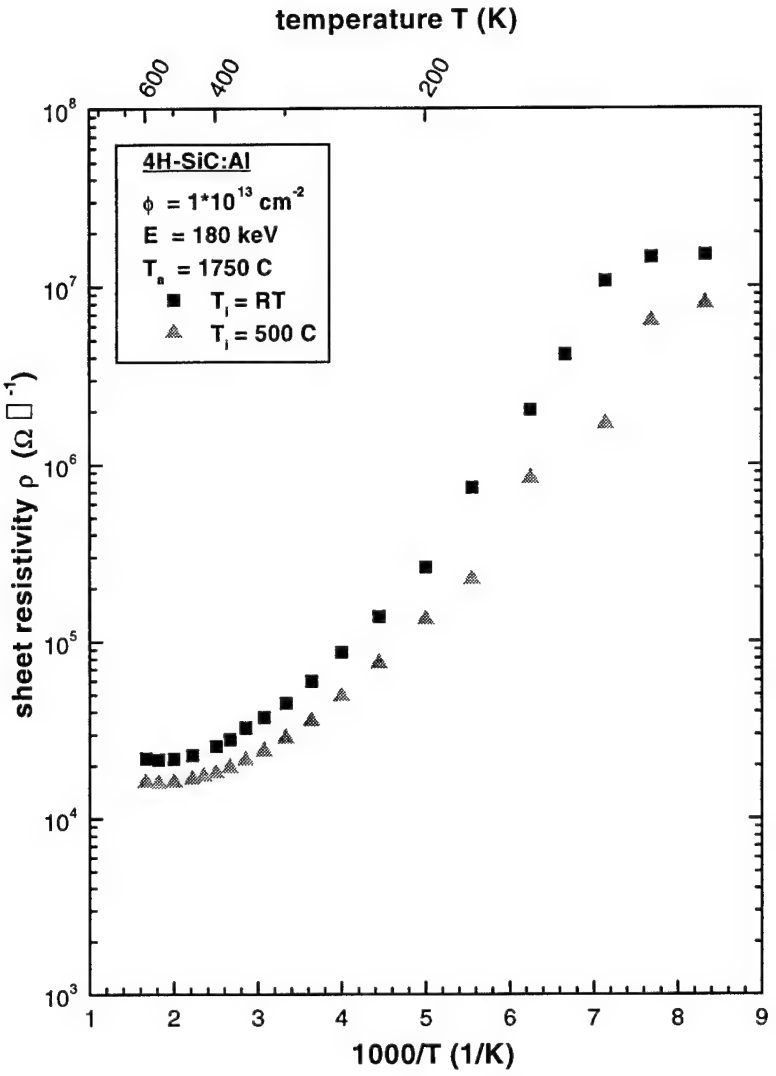

Figure IV-28. Resistivity temperature dependence for 4H-SiC samples Al implanted $\phi = 1x10^{13}$ cm^{-2} at either 500 °C or RT and annealed at 1750 °C. The results indicate a lower minimum resistivity for samples implanted at RT.

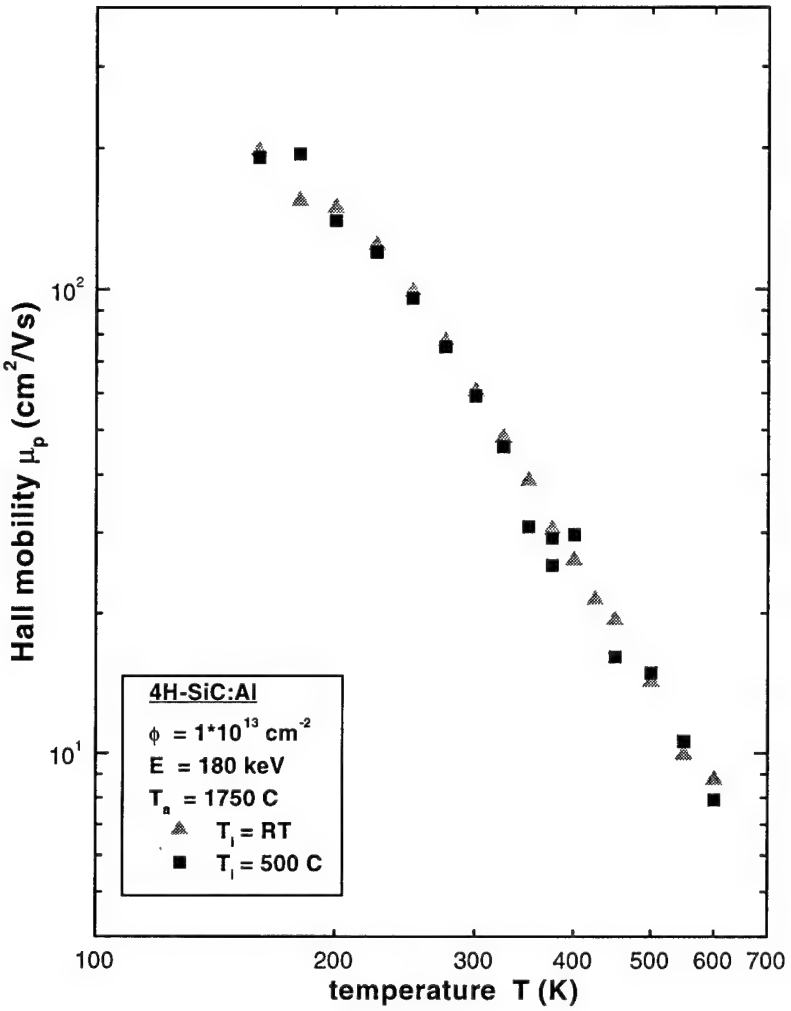

Figure IV-29. Hall mobility temperature dependence for Al implanted 4H-SiC samples at either 500 °C or RT with 1x10^{13} cm^{-2} and annealed at 1750 °C.

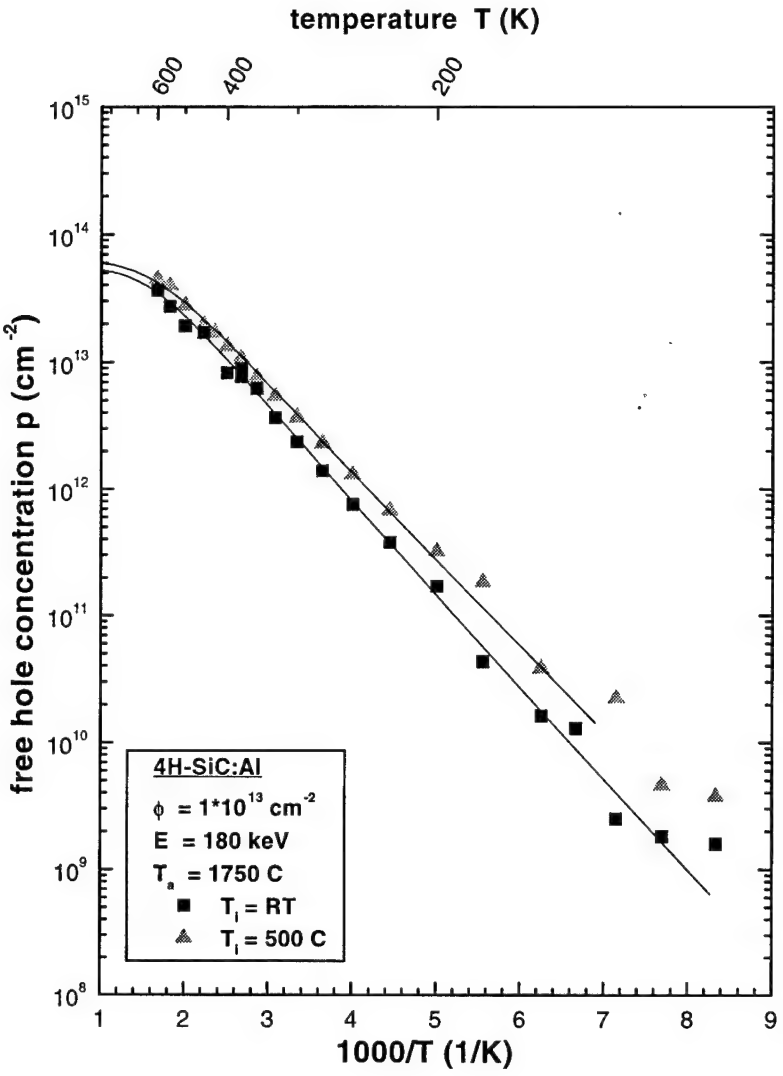

Figure IV-30. Carrier concentration temperature dependence for 4H-SiC samples Al implanted $\phi = 1x10^{13}$ cm^{-2} at either 500 °C or RT and annealed at 1750 °C.

Table IV-5. Fit parameters of the carrier concentration plots in Figure IV-21.

ion	dose (cm^{-2})	Anneal temp T_a (°C)	acceptor sheet concentration N_A (10^{14} cm^{-2})	activation energy E_A (meV)	electrical activity D
Al	$1x10^{13}$ (RT)	1750	6.0 ± 2.0	260 ± 10	6.0
Al	$1x10^{13}$ (500°C)	1750	6.2 ± 1.1	245 ± 8	6.2

V. Conclusions

The primary goals of this research were proposed in Chapter I. This chapter will review each of these goals and, drawing upon the analysis, reach some conclusions about each one. The analysis also discussed the difficulties with forming ohmic contacts to this material and some conclusions drawn from that experience will be touched on in this chapter as well. Since there were significant difficulties with the samples and with the data, any conclusions made will not give the full answer and future research will need to be done. A section within this chapter will propose future research to complement that which has already been done and to further answer the original proposed questions.

Less than ideal semiconductor behavior was evident from the samples studied in this research. Implantation and annealing did, however, significantly increase the carrier concentrations in the samples as was intended. The samples annealed at 1750 °C displayed the most reasonable results, but the highest carrier concentrations were measured for samples annealed at 1650 °C and 1550 °C for Al and B implanted samples respectively. The concentration data for every sample was fit to the dominant acceptor model, and from the nonlinear least squares fitting the average ionization energies for the Al and B acceptor were found to be ~ 252 and ~ 285 meV, respectively. These values lie within the expected range. Thus, ion implantation and high temperature annealing appear to be a viable technique for increasing the carrier concentration in 4H-SiC.

Control over the implantation and therefore the conductivity was also demonstrated since the data shows relationships between implantation dose and annealing temperature and the resulting carrier concentrations, mobility, and resistivity. A dose of $3x10^{13}$ cm^{-2} resulted in the highest carrier concentrations for both Al and B implantation; the dose of $3x10^{13}$ cm^{-2} resulted in higher carrier concentrations than the dose of $1x10^{14}$ cm^{-2}, which is a completely unexpected result. The optimum anneal temperatures are found to be 1650 °C and 1550 °C for the Al and B implanted samples respectively, because annealing at this temperature resulted in the highest carrier concentrations. On average, implantation at 500 °C apparently did not make a significant difference in the resulting carrier concentration, mobility or resistivity. Considering all the samples it was

also apparent that Al implantation on average resulted in better material properties compared to B implantation.

With regards to forming good ohmic contacts, the best procedure for surface preparation was described in the analysis section. Rigorous cleaning was found to improve the results but not adequately enough to be completely confident in them. Thermal or e-beam evaporation of straight aluminum on to the cleaned surface, followed by annealing at ~ 1000 °C for 5 min was found to work best for these samples. It is assumed that this procedure is adequate for 4H-SiC in general.

Shallow corner implantation has not been demonstrated as an effective means for helping to form ohmic contacts. Whether this implantation resulted in significant amorphization of the material which made it impossible to form good ohmic contacts is not fully known, but it is certain that the region of implantation was much too large. This large implanted area and the subsequent annealing is also likely to have been partly responsible for the large carrier concentrations. Electrically active acceptor concentration measurements were all below 1.3×10^{15} cm^{-2}, which corresponds to the average sheet concentration for the fluence implanted into the corners.

Future research on these implanted samples and on 4H-SiC in general needs to be done. For these samples the Hall measurements should be done over using a stronger magnetic field (~ 1 *T*) and over a larger temperature range (up to ~ 1000 °C). A stronger magnetic field should produce larger Hall voltages and therefore make it more obvious that real Hall voltage was being measured. The higher temperature range is needed to see the full sheet concentration versus temperature curve, including some of the intrinsic carrier region.

Prior to any new measurements the samples should have their edge zones removed using reactive ion etching to prevent leakage currents over the sample edges. The contacts should also be improved as much as possible, by either adding more metal and annealing or completely re-cleaning the surfaces and depositing new metal. A different model for fitting the data could also be investigated since there could be multiple acceptors in the samples, specifically the B implanted samples. The results from the B implanted samples in this research did not fit the model well, and it is assumed this is because Al acceptors were also present.

Other measurements should also be done on these samples, specifically cathodaluminescense (CL) and SIMs. CL measurements would allow us to a different means for measuring the acceptor ionization energies, and therefore offer some sort of comparison for the analysis done in this research. A SIMs analysis would help to characterize the implantation profile resulting from both the main and shallow implantation and for the B implanted samples, to see the effects of implanting multiple ion species.

If another study on low doped 4H-SiC is considered using temperature dependent Hall effect measurements then a shallow co-implantation of Al/C should be done in the sample corners to create a highly doped region and assist in forming ohmic contacts. Co-implantation has been proven in this capacity for p-type SiC [31:1414]. This shallow implantation would also needs to be done only over a very small region of the sample's surface.

VII. Appendix A: Free Hole Concentration Measurements and Fitting Results

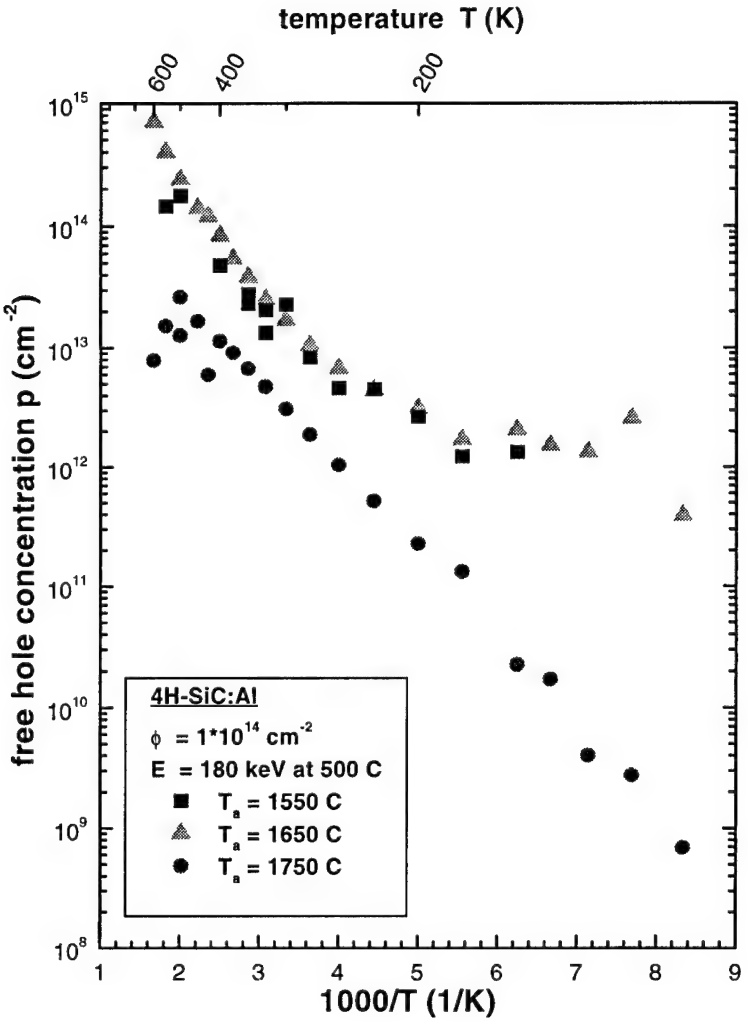

Figure VII-31. Free hole concentration measurements on Al implanted 4H-SiC samples at high temperature (500 °C) with 1x10^{14} cm^{-2} and annealed at 1550 °C, 1650 °C, and 1750 °C for 30 min in Ar.

ion	dose (cm^{-2})	Anneal temp T_a (°C)	acceptor sheet concentration N_A (10^{14} cm^{-2})	activation energy E_A (meV)	electrical activity D
Al	1x10^{14} (500°C)	1550	1.4 ± .7	200 ± 30	1.4
Al	1x10^{14} (500°C)	1650	10.1 ± 1.8	238 ± 6	10.1
Al	1x10^{14} (500°C)	1750	.37 ± .08	243 ± 6	.37

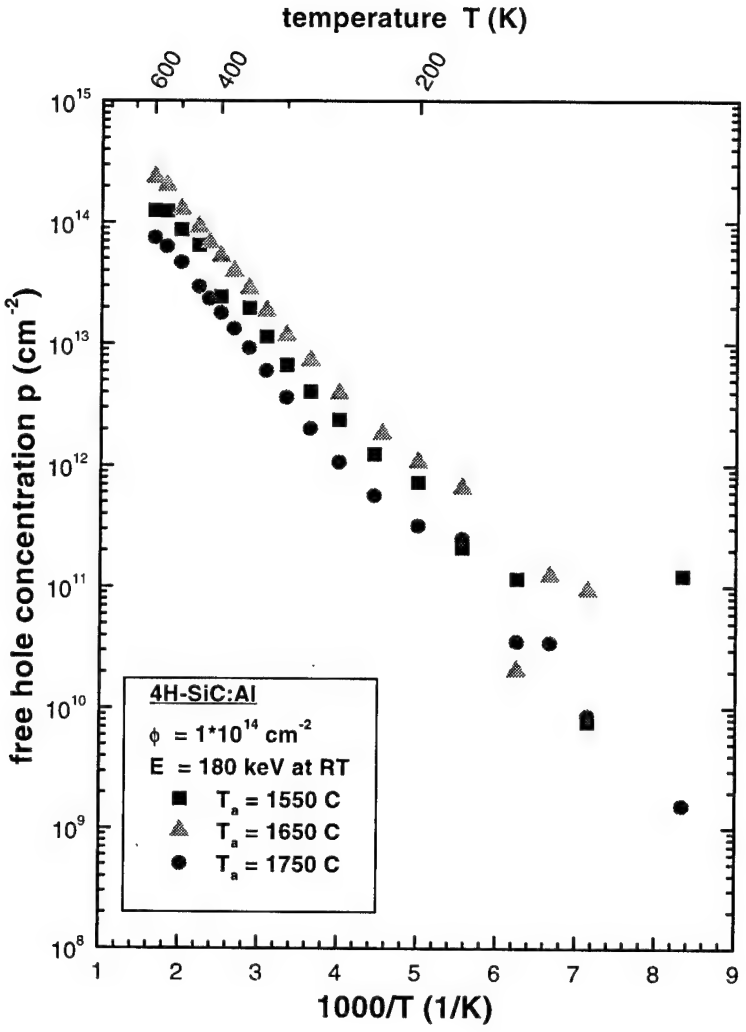

Figure VII-32. Free hole concentration measurements on Al implanted 4H-SiC samples at room temperature with 1x10^{14} cm^{-2} and annealed at 1550 °C, 1650 °C, and 1750 °C for 30 min in Ar.

ion	dose (cm^{-2})	anneal temp T_a (°C)	Acceptor sheet concentration N_A (10^{14} cm^{-2})	Activation energy E_A (meV)	electrical activity D
Al	1x10^{14} (RT)	1550	4.9 ± 1.6	267 ± 7	4.9
Al	1x10^{14} (RT)	1650	9.9 ± 2.8	258 ± 8	9.9
Al	1x10^{14} (RT)	1750	1.8 ± .5	274 ± 6	1.8

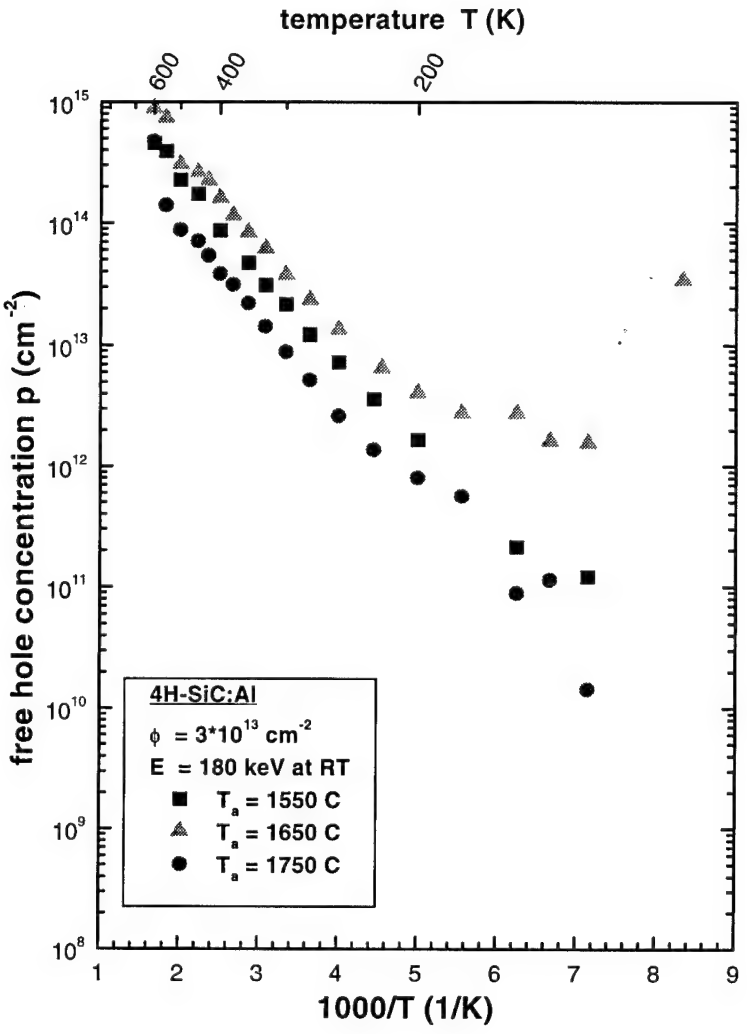

Figure VII-33. Free hole concentration measurements on Al implanted 4H-SiC samples at room temperature with 3x10^{13} cm^{-2} and annealed at 1550 °C, 1650 °C, and 1750 °C for 30 min in Ar.

ion	dose (cm^{-2})	anneal temp T_a (°C)	Acceptor sheet concentration N_A (10^{13} cm^{-2})	Activation energy E_A (meV)	electrical activity D
Al	3x10^{13} (RT)	1550	246 ± 45	252 ± 5	82
Al	3x10^{13} (RT)	1650	390 ± 8	237 ± 2	130
Al	3x10^{13} (RT)	1750	39 ± 6	249 ± 6	13

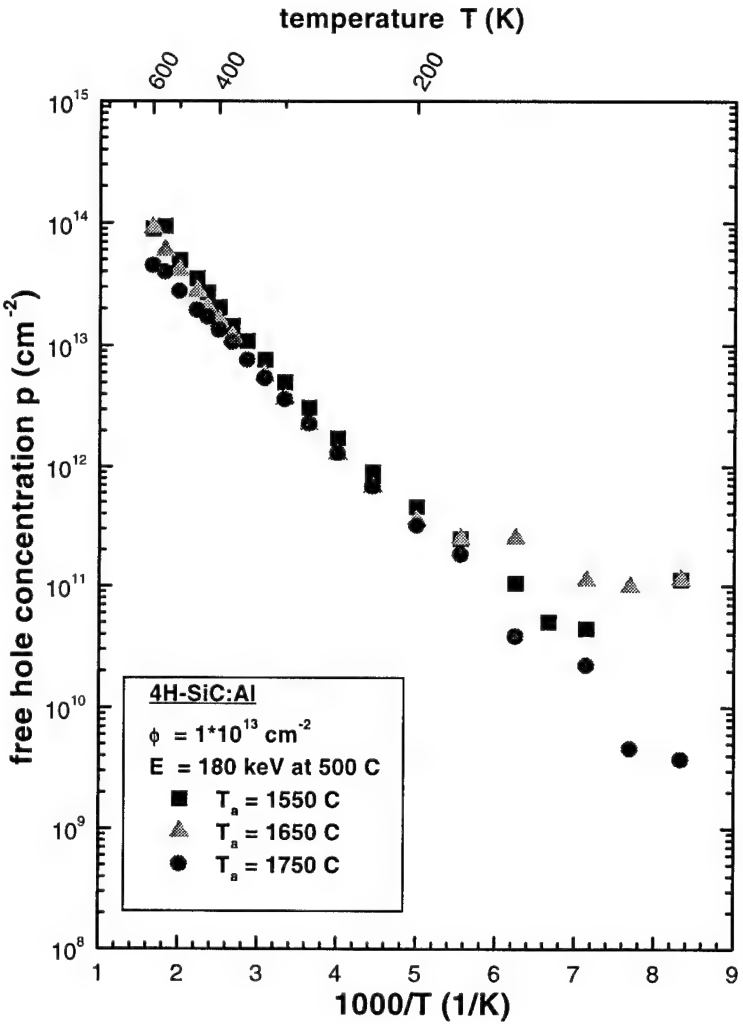

Figure VII-34. Free hole concentration measurements on Al implanted 4H-SiC samples at high temperature (500°C) with 1x10^{13} cm^{-2} and annealed at 1550 °C, 1650 °C, and 1750 °C for 30 min in Ar.

ion	dose (cm^{-2})	anneal temp T_a (°C)	acceptor sheet concentration N_A (10^{13} cm^{-2})	Activation energy E_A (meV)	electrical activity D
Al	1x10^{13} (500°C)	1550	19 ± 5	280.1 ± 5	19
Al	1x10^{13} (500°C)	1650	18 ± 4	258 ± 7	18
Al	1x10^{13} (500°C)	1750	6.2 ± 1.1	245 ± 8	6.2

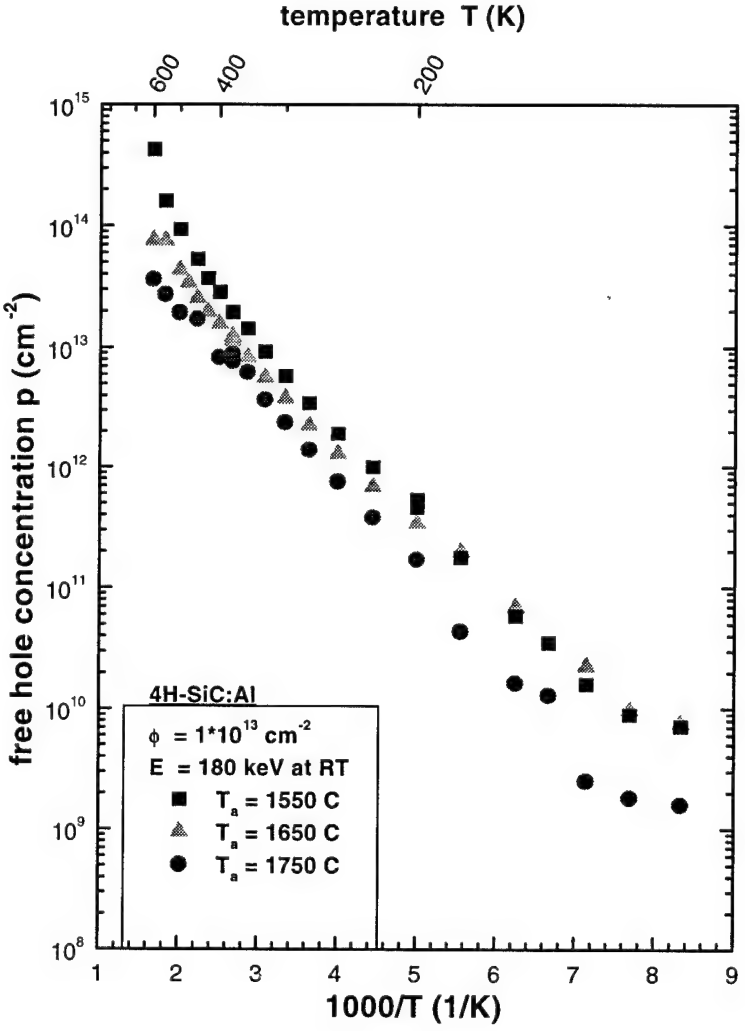

Figure VII-35. Free hole concentration measurements on Al implanted 4H-SiC samples at high temperature (500°C) with 1x10^{13} cm^{-2} and annealed at 1550 °C, 1650 °C, and 1750 °C for 30 min in Ar.

ion	dose (cm^{-2})	anneal temp T_a (°C)	Acceptor sheet concentration N_A (10^{13} cm^{-2})	activation energy E_A (meV)	electrical activity D
Al	1x10^{13} (RT)	1550	35 ± 9	265 ± 7	35.0
Al	1x10^{13} (RT)	1650	13 ± 3	265 ± 9	12.9
Al	1x10^{13} (RT)	1750	6.0 ± 2.0	260 ± 10	6.0

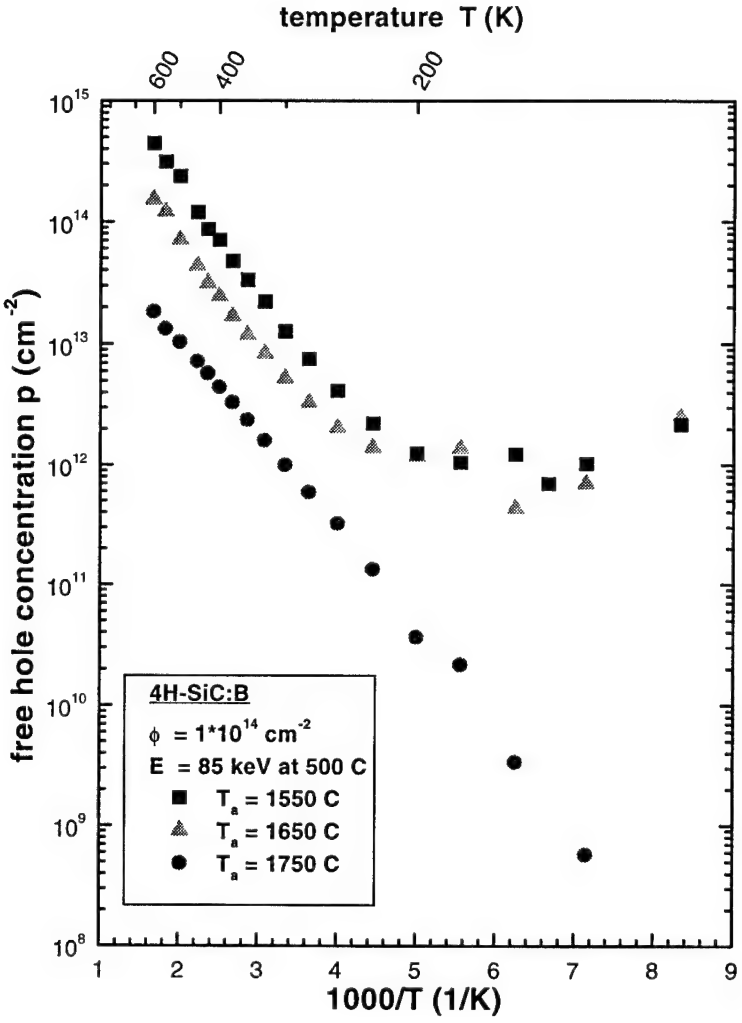

Figure VII-36. Free hole concentration measurements on B implanted 4H-SiC samples at high temperature (500°C) with 1x10^{14} cm^{-2} and annealed at 1550 °C, 1650 °C, and 1750 °C for 30 min in Ar.

ion	dose (cm^{-2})	anneal temp T_a (°C)	Acceptor sheet concentration N_A (10^{14} cm^{-2})	Activation energy E_A (meV)	electrical activity D
B	1x10^{14} (500°C)	1550	49 ± 7	293 ± 10	49
B	1x10^{14} (500°C)	1650	7.3 ± 1.6	298 ± 4	7.3
B	1x10^{14} (500°C)	1750	.25 ± .03	295 ± 5	.2

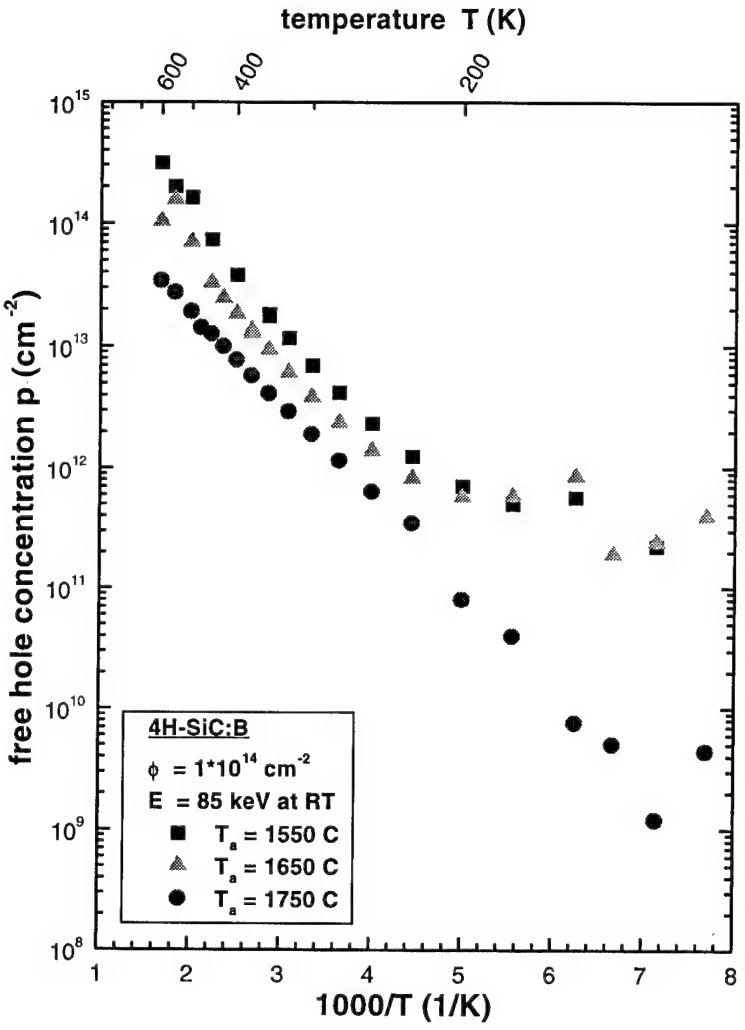

Figure VII- 37. Free hole concentration measurements on B implanted 4H-SiC samples at room temperature with 1x10^{14} cm^{-2} and annealed at 1550 °C, 1650 °C, and 1750 °C for 30 min in Ar.

ion	dose (cm^{-2})	anneal temp T_a (°C)	Acceptor sheet concentration N_A (10^{14} cm^{-2})	activation energy E_A (meV)	electrical activity D
B	1x10^{14} (RT)	1550	12 ± 4	281 ± 7	12
B	1x10^{14} (RT)	1650	3.2 ± .6	287 ± 9	3.2
B	1x10^{14} (RT)	1750	.53 ± .09	281 ± 7	.53

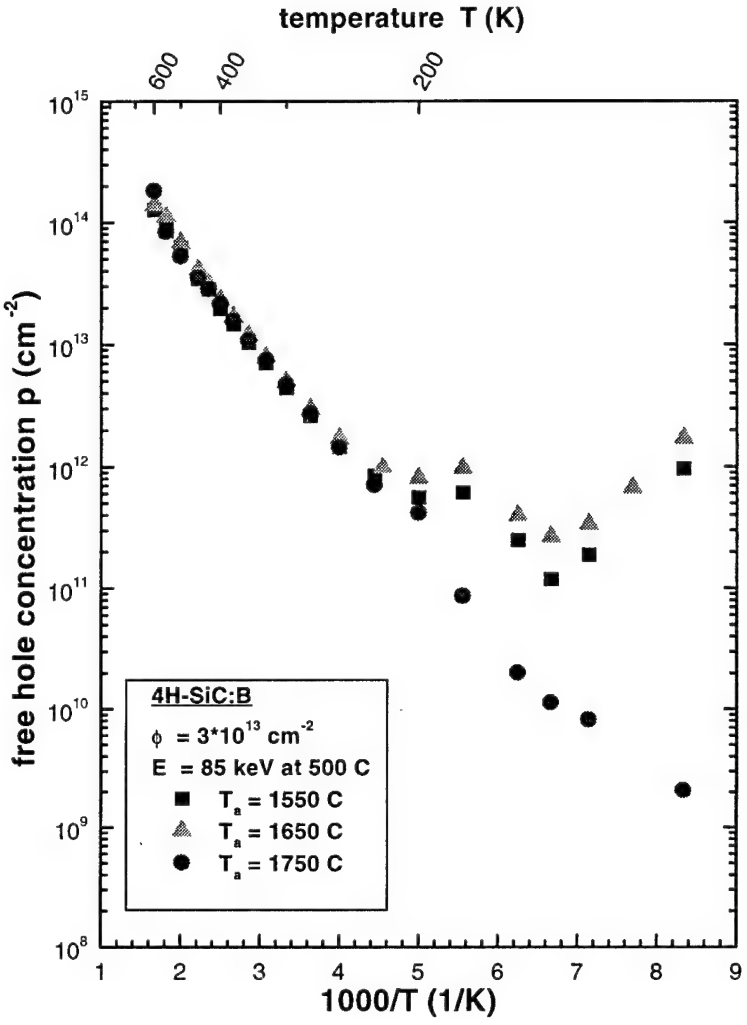

Figure VII-38. Free hole concentration measurements on B implanted 4H-SiC samples at high temperature (500°C) with 3x10^{13} cm^{-2} and annealed at 1550 °C, 1650 °C, and 1750 °C for 30 min in Ar.

ion	dose (cm^{-2})	Anneal temp T_a (°C)	acceptor sheet concentration N_A (10^{13} cm^{-2})	Activation energy E_A (meV)	electrical activity D
B	3x10^{13} (500°C)	1550	21 ± 7	270 ± 7	6.9
B	3x10^{13} (500°C)	1650	47 ± 3	285 ± 5	16
B	3x10^{13} (500°C)	1750	28 ± 5	300 ± 5	9.3

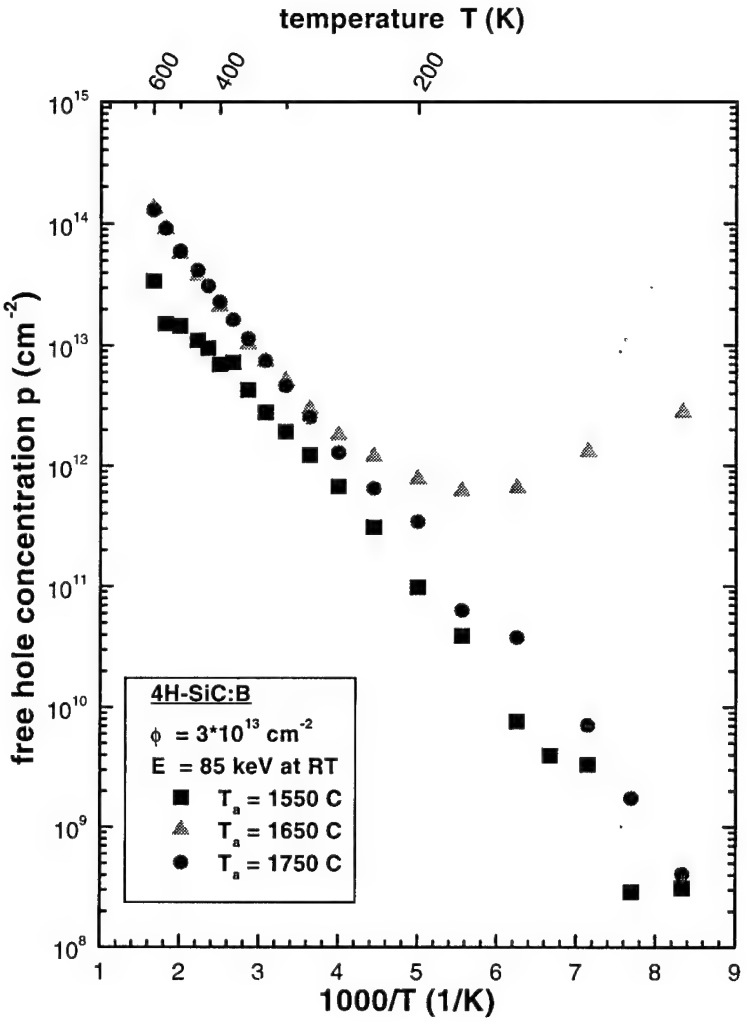

Figure VII- 39. Free hole concentration measurements on B implanted 4H-SiC samples at room temperature with 3x10^{13} cm^{-2} and annealed at 1550 °C, 1650 °C, and 1750 °C for 30 min in Ar.

ion	dose (cm^{-2})	anneal temp T_a (°C)	Acceptor sheet concentration N_A (10^{13} cm^{-2})	activation energy E_A (meV)	electrical activity D
B	3x10^{13} (RT)	1550	2.8 ± .3	265 ± 6	.84
B	3x10^{13} (RT)	1650	34 ± 7	279 ± 13	11
B	3x10^{13} (RT)	1750	66 ± 10	300 ± 5	22

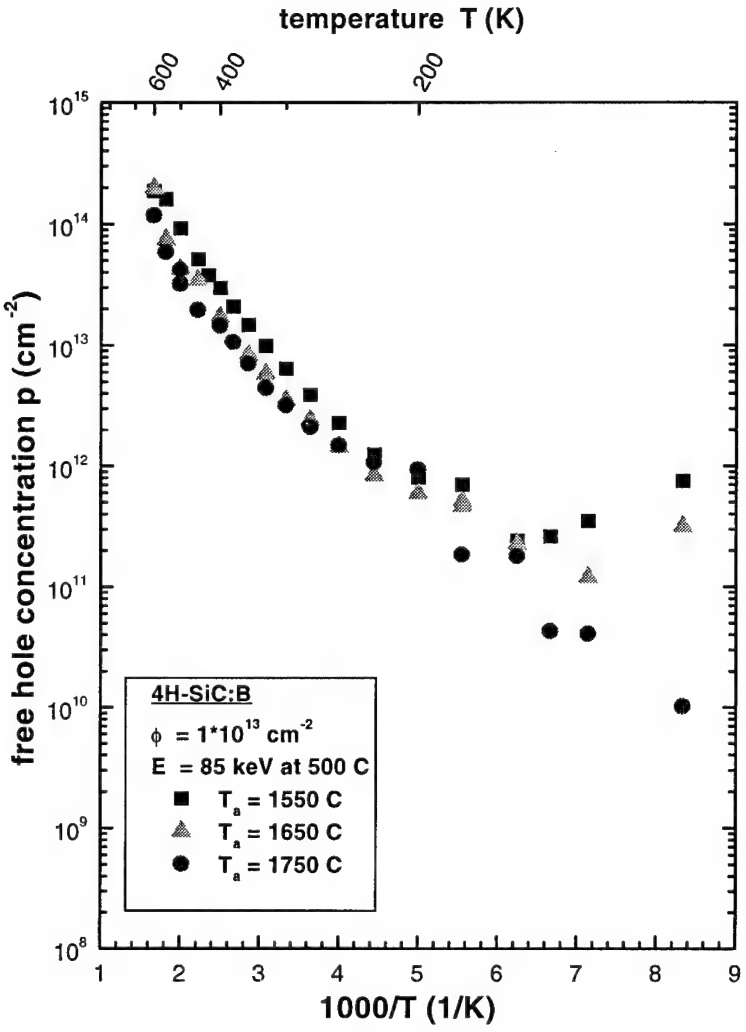

Figure VII- 40. Free hole concentration measurements on B implanted 4H-SiC samples at high temperature (500°C) with $1x10^{13}$ cm^{-2} and annealed at 1550 °C, 1650 °C, and 1750 °C for 30 min in Ar.

ion	dose (cm^{-2})	anneal temp T_a (°C)	acceptor sheet concentration N_A (10^{13} cm^{-2})	Activation energy E_A (meV)	electrical activity D
B	$1x10^{13}$ (500°C)	1550	77 ± 14	285 ± 8	77
B	$1x10^{13}$ (500°C)	1650	23 ± 2	282 ± 3	23
B	$1x10^{13}$ (500°C)	1750	23 ± 1	298± 20	23

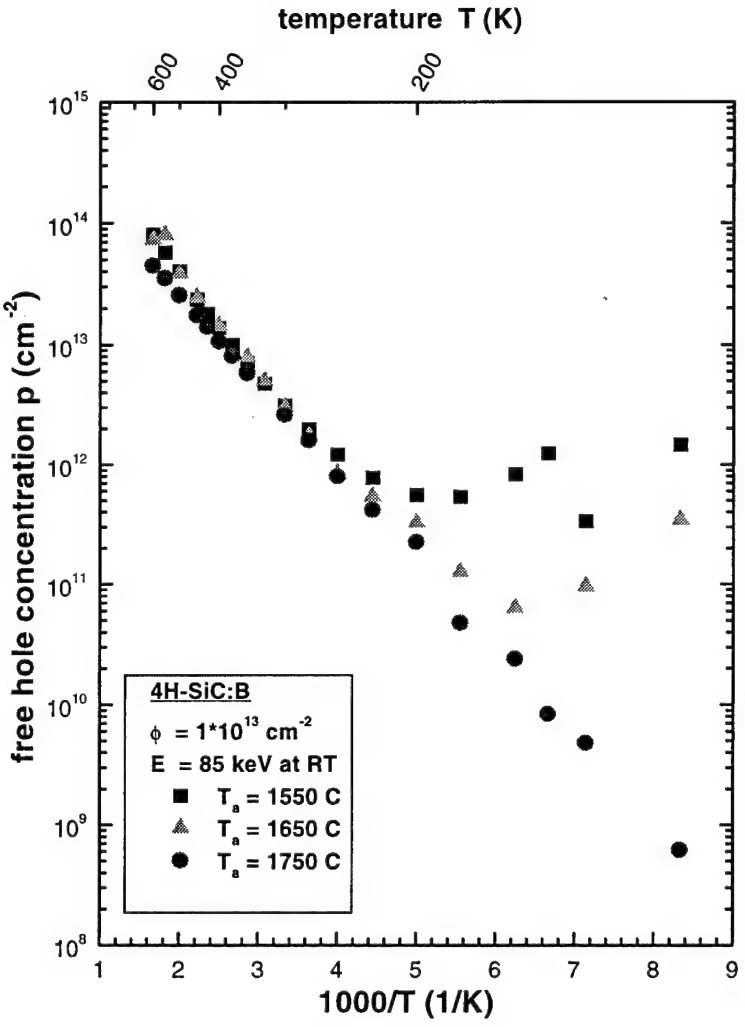

Figure VII-41. Free hole concentration measurements on B implanted 4H-SiC samples at room temperature with 1x10^{13} cm^{-2} and annealed at 1550 °C, 1650 °C, and 1750 °C for 30 min in Ar.

ion	dose (cm^{-2})	Anneal temp T_a (°C)	Acceptor sheet concentration N_A (10^{13} cm^{-2})	activation energy E_A (meV)	electrical activity D
B	1x10^{13} (RT)	1550	19 ± 8	293 ± 6	19
B	1x10^{13} (RT)	1650	26 ± 4	297 ± 4	26
B	1x10^{13} (RT)	1750	8.0 ± 1	273 ± 6	8.0

VIII. Appendix B: Conductivity Results

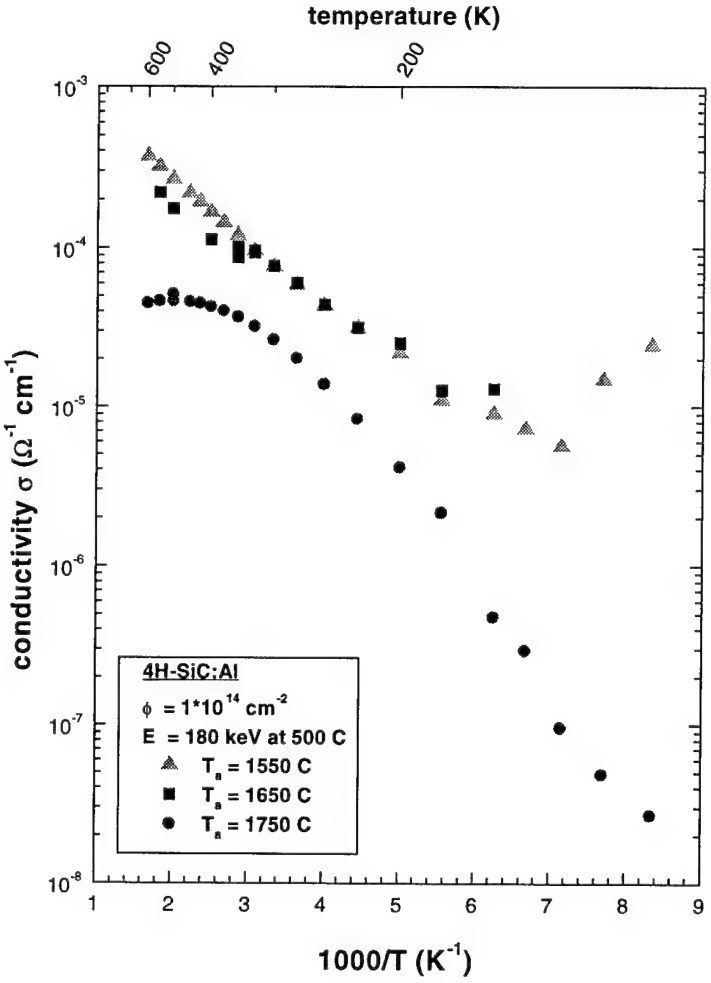

Figure VIII-1. Conductivity measurements on Al implanted 4H-SiC samples at high temperature (500 °C) with $1x10^{14}$ cm^{-2} and annealed at 1550 °C, 1650 °C, and 1750 °C for 30 min in Ar.

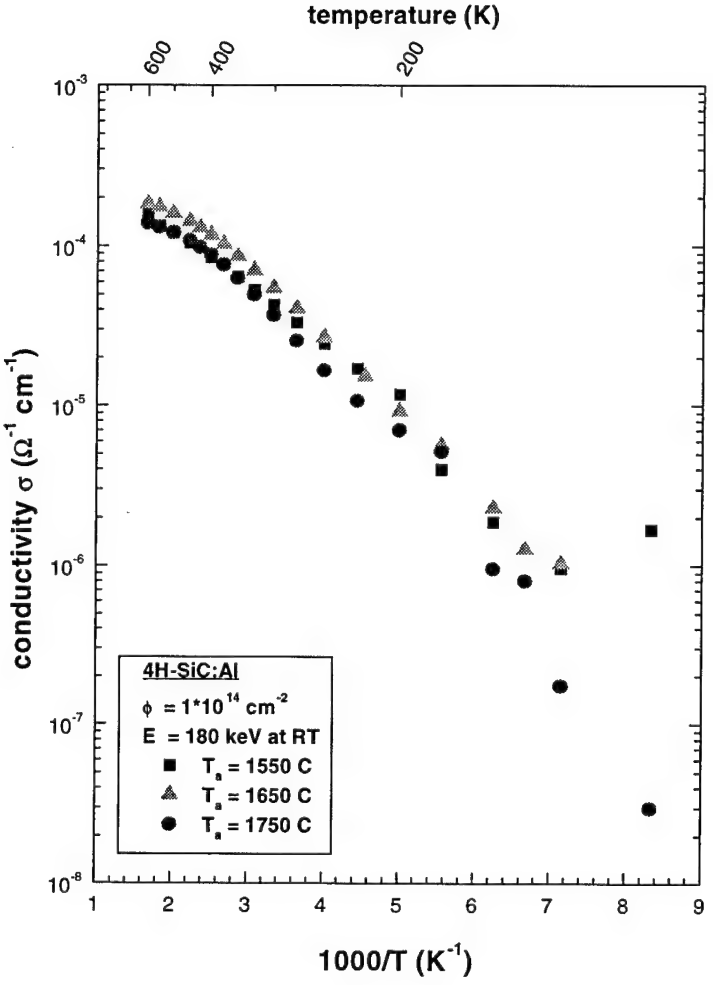

Figure VIII-2. Conductivity measurements on Al implanted 4H-SiC samples at room temperature with $1x10^{14}$ cm^{-2} and annealed at 1550 °C, 1650 °C, and 1750 °C for 30 min in Ar.

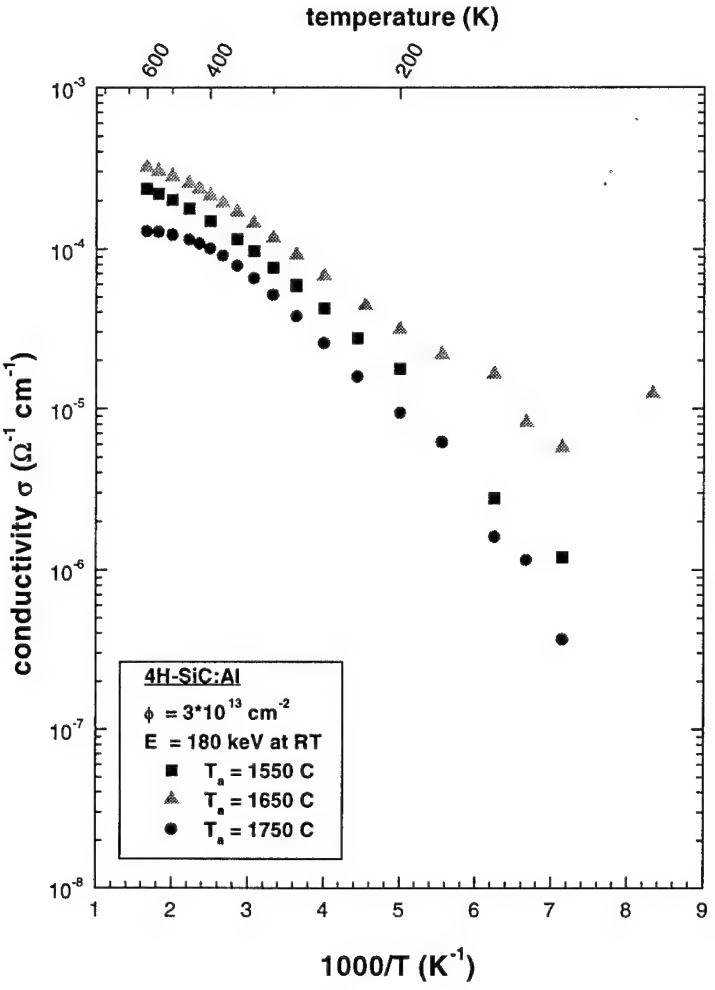

Figure VIII-3. Conductivity measurements on Al implanted 4H-SiC samples at room temperature with $3x10^{13}$ cm^{-2} and annealed at 1550 °C, 1650 °C, and 1750 °C for 30 min in Ar.

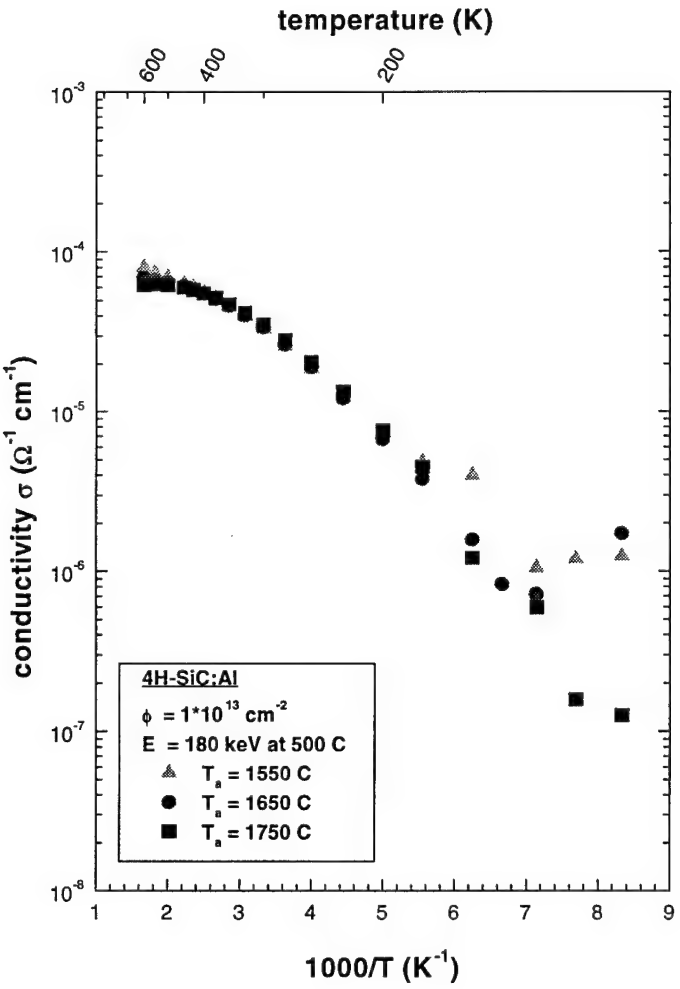

Figure VIII-4. Conductivity measurements on Al implanted 4H-SiC samples at high temperature (500 °C) with $1x10^{13}$ cm^{-2} and annealed at 1550 °C, 1650 °C, and 1750 °C for 30 min in Ar.

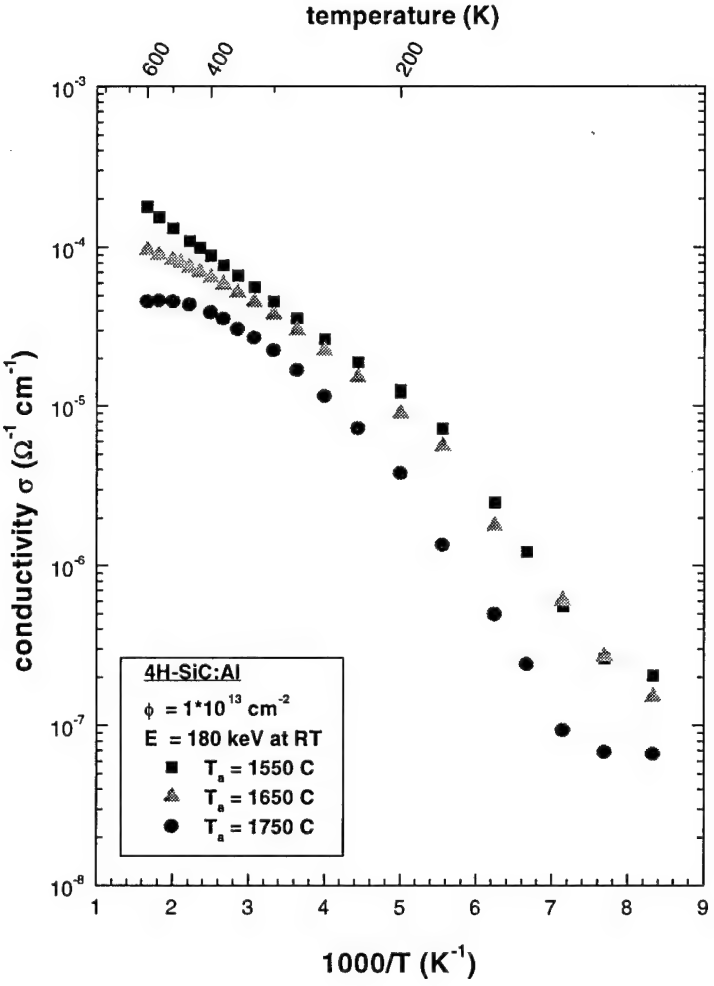

Figure VIII-5. Conductivity measurements on Al implanted 4H-SiC samples at room temperature with $1x10^{13}$ cm^{-2} and annealed at 1550 °C, 1650 °C, and 1750 °C for 30 min in Ar.

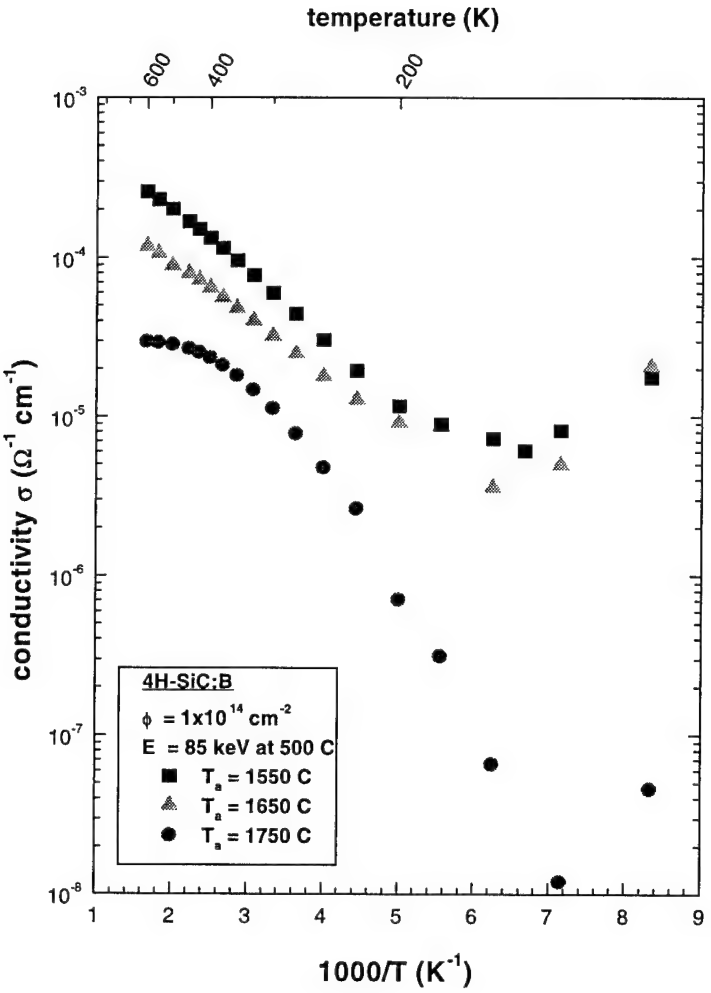

Figure VIII-6. Conductivity measurements on B implanted 4H-SiC samples at high temperature (500°C) with $1x10^{14}$ cm^{-2} and annealed at 1550 °C, 1650 °C, and 1750 °C for 30 min in Ar.

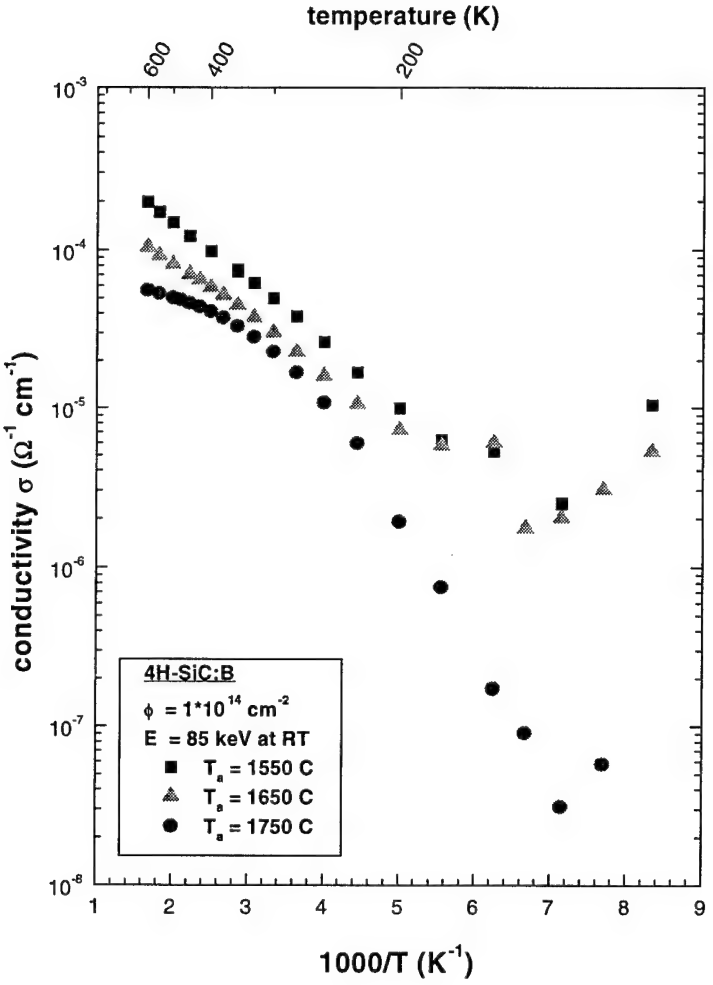

Figure VIII-7. Conductivity measurements on B implanted 4H-SiC samples at room temperature with $1x10^{14}$ cm^{-2} and annealed at 1550 °C, 1650 °C, and 1750 °C for 30 min in Ar.

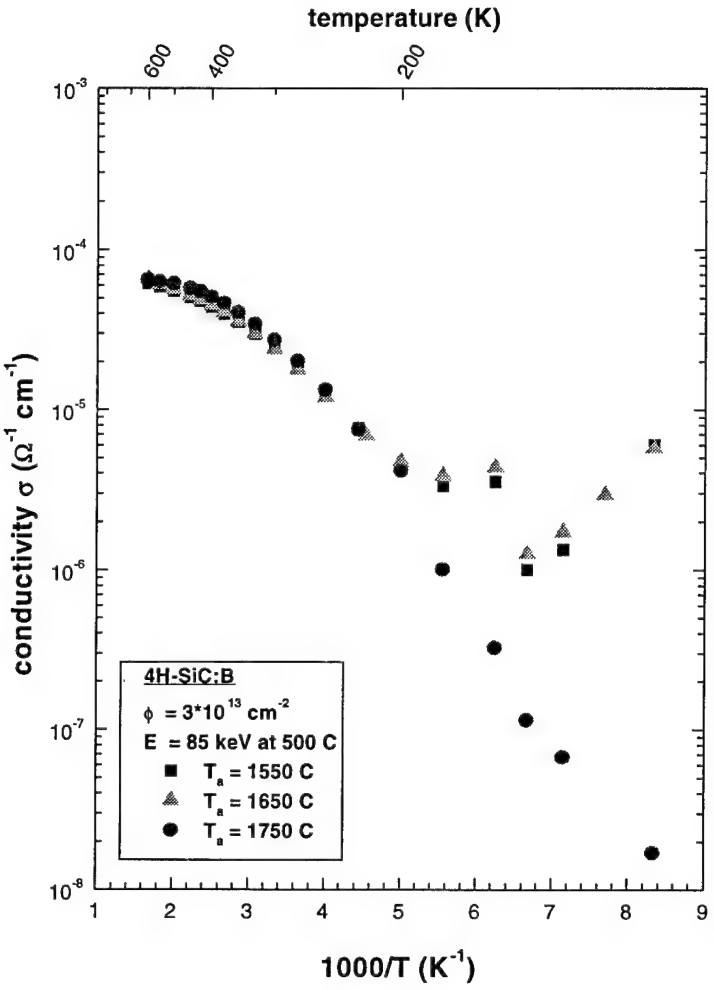

Figure VIII-8. Conductivity measurements on B implanted 4H-SiC samples at room temperature with $3x10^{13}$ cm^{-2} and annealed at 1550 °C, 1650 °C, and 1750 °C for 30 min in Ar.

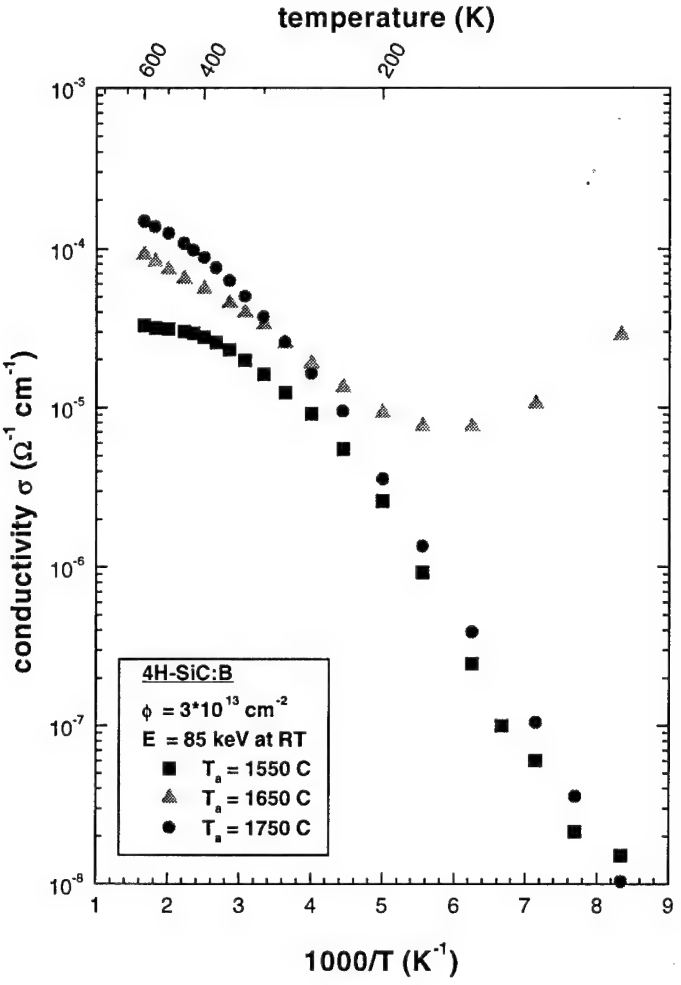

Figure VIII-9. Conductivity measurements on B implanted 4H-SiC samples at room temperature with $3x10^{13}$ cm^{-2} and annealed at 1550 °C, 1650 °C, and 1750 °C for 30 min in Ar.

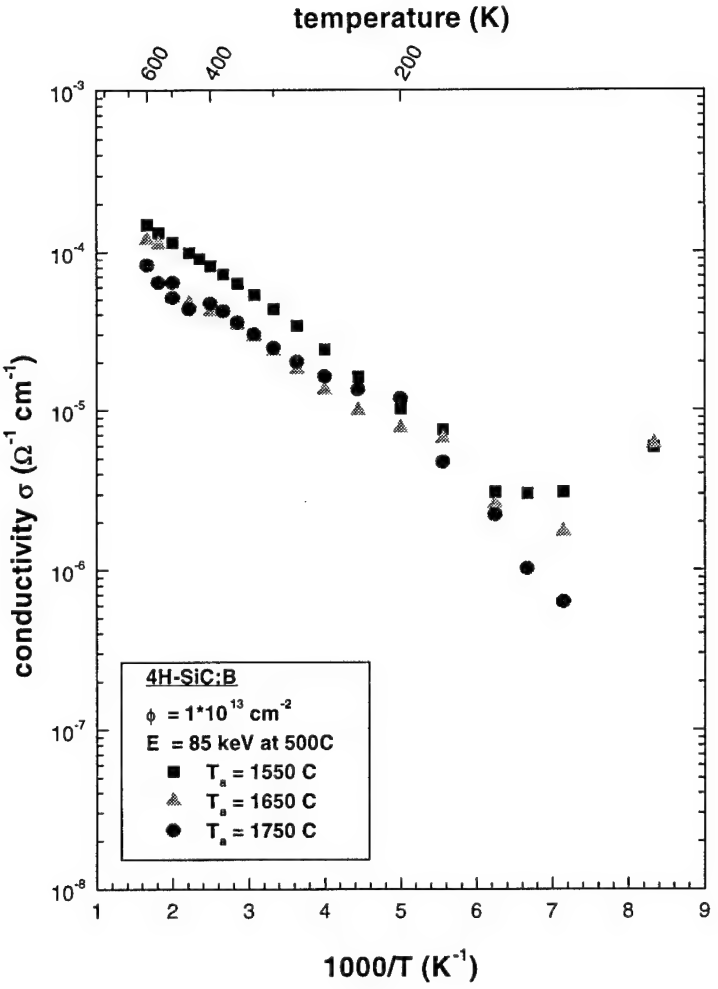

Figure VIII-10. Conductivity measurements on B implanted 4H-SiC samples at high temperature (500°C) with $1x10^{13}$ cm^{-2} and annealed at 1550 °C, 1650 °C, and 1750 °C for 30 min in Ar.

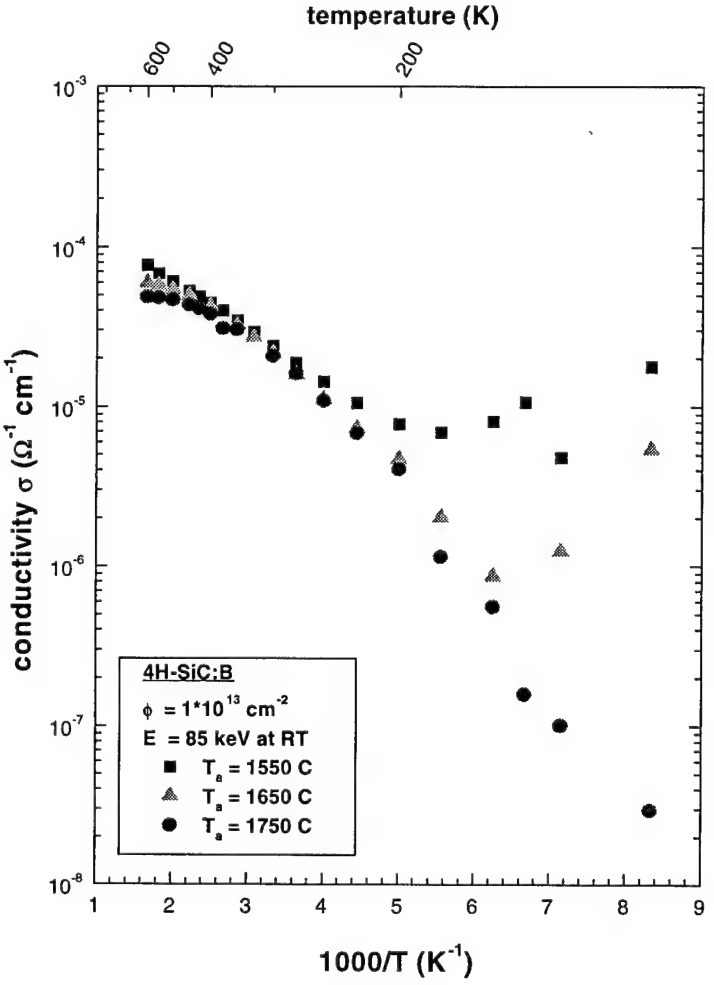

Figure VIII-11. Conductivity measurements on B implanted 4H-SiC samples at room temperature with $1x10^{13}$ cm^{-2} and annealed at 1550 °C, 1650 °C, and 1750 °C for 30 min in Ar.

IX. Appendix C: Hall Mobility Results

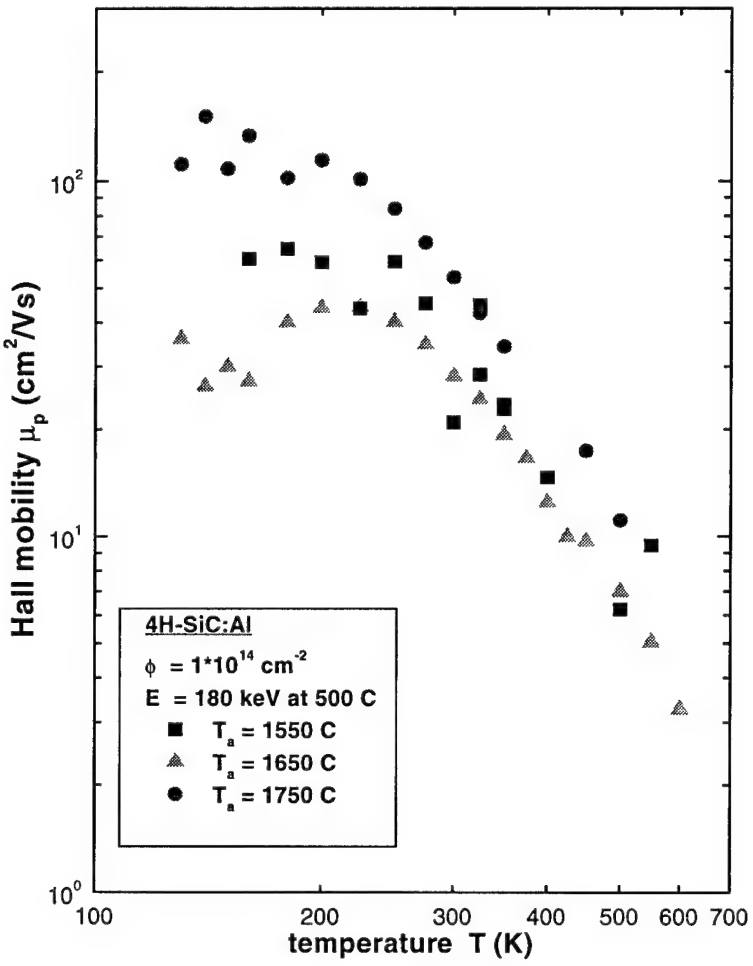

Figure IX-1. Hall mobility measurements on Al implanted 4H-SiC samples at high temperature (500°C) with 1x10^{14} cm^{-2} and annealed at 1550 °C, 1650 °C, and 1750 °C for 30 min in Ar.

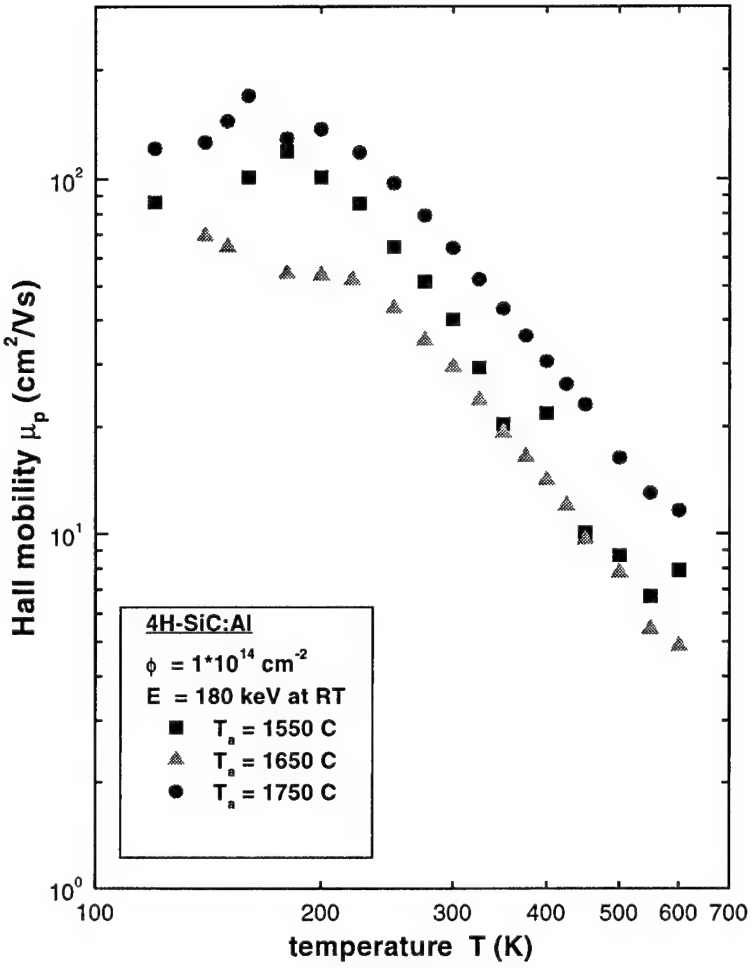

Figure IX-2. Hall mobility measurements on Al implanted 4H-SiC samples at room temperature with 1x10^{14} cm^{-2} and annealed at 1550 °C, 1650 °C, and 1750 °C for 30 min in Ar.

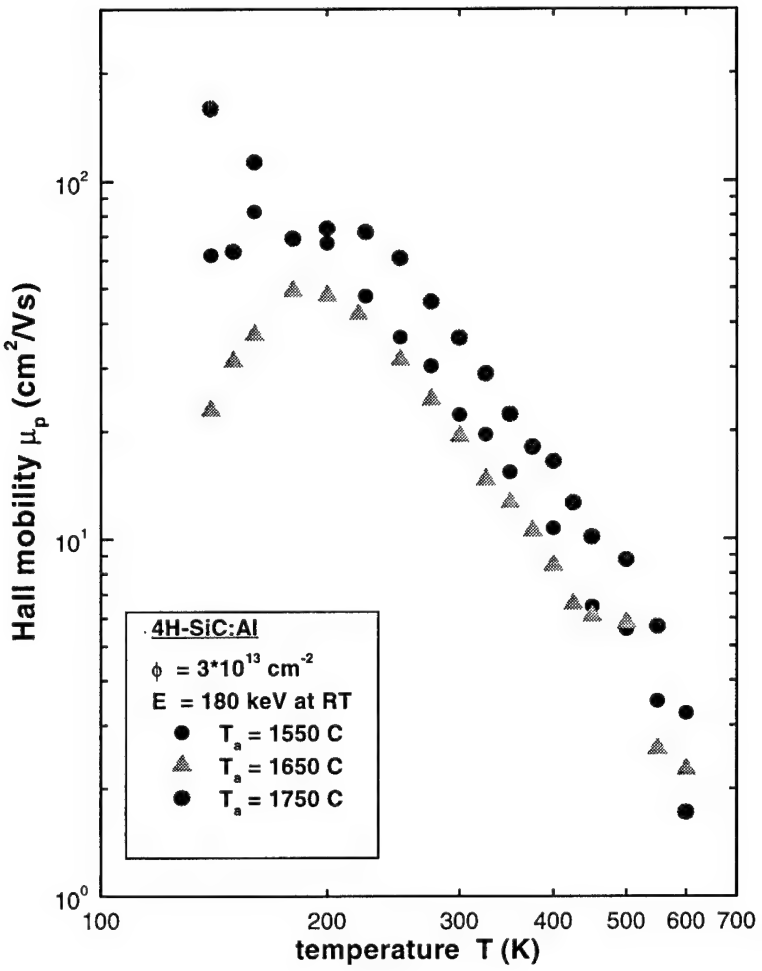

Figure IX-3. Hall mobility measurements on Al implanted 4H-SiC samples at room temperature with $3x10^{13}$ cm^{-2} and annealed at 1550 °C, 1650 °C, and 1750 °C for 30 min in Ar.

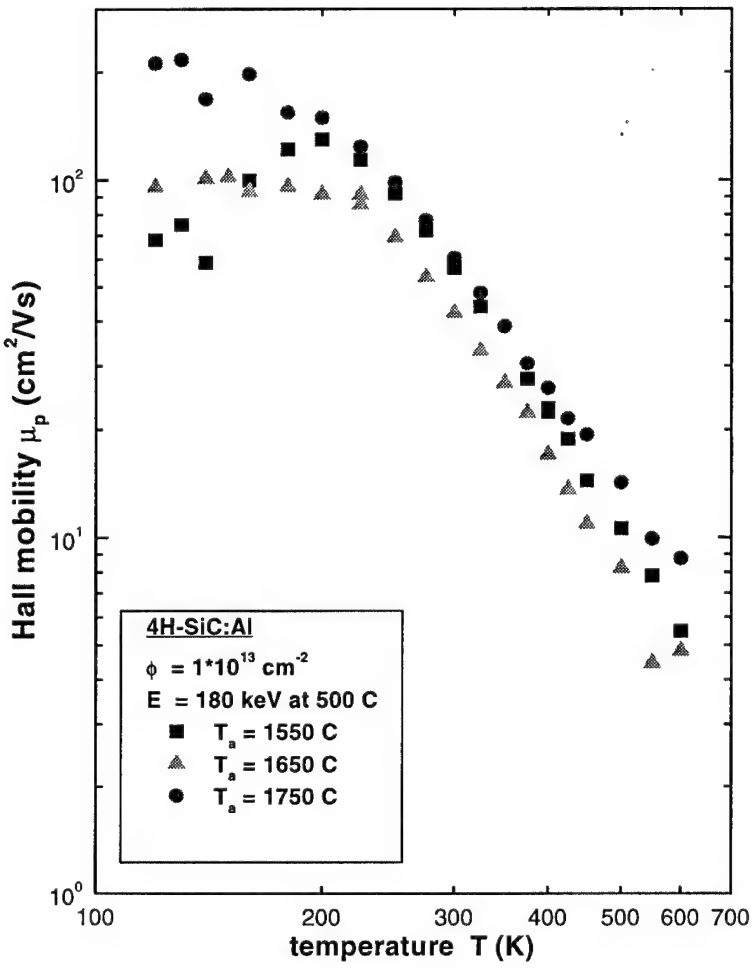

Figure IX-4. Hall mobility measurements on Al implanted 4H-SiC samples at high temperature (500°C) with 1x10^{13} cm^{-2} and annealed at 1550 °C, 1650 °C, and 1750 °C for 30 min in Ar.

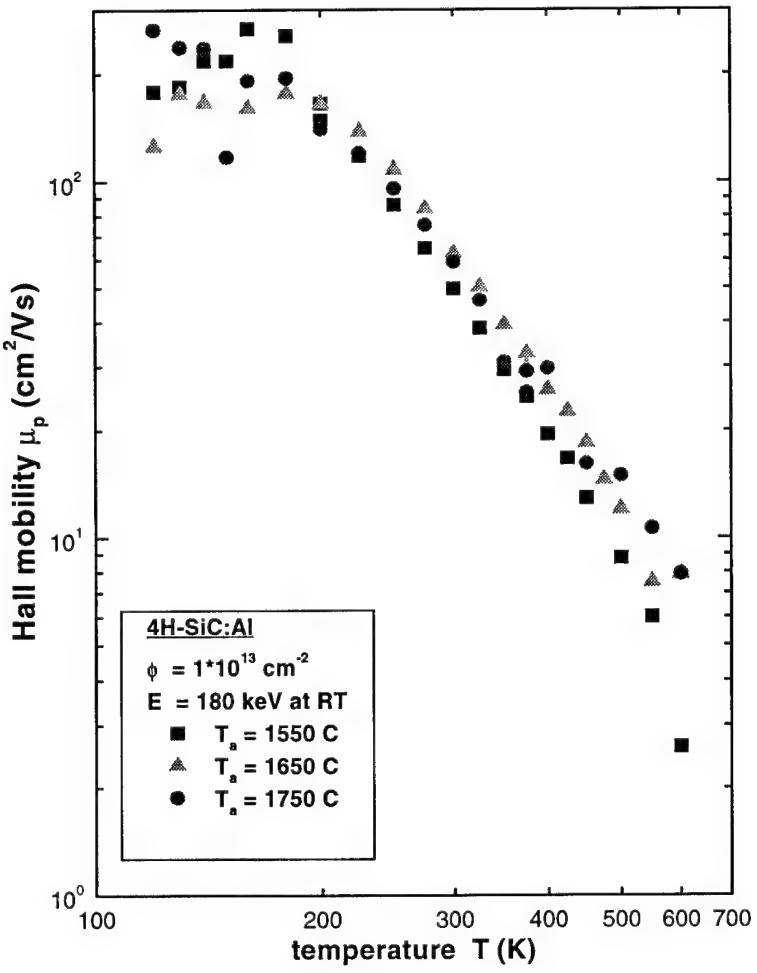

Figure IX-5. Hall mobility measurements on Al implanted 4H-SiC samples at room temperature with 1x10^{13} cm^{-2} and annealed at 1550 °C, 1650 °C, and 1750 °C for 30 min in Ar.

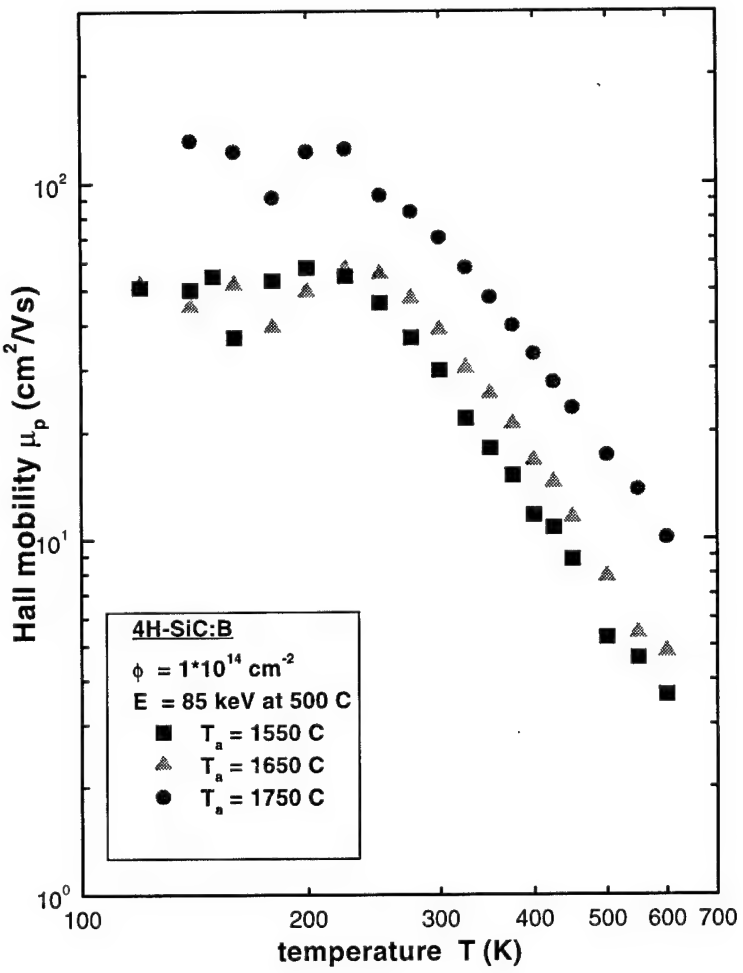

Figure IX-6. Hall mobility measurements on B implanted 4H-SiC samples at high temperature (500°C) with 1x10^{14} cm^{-2} and annealed at 1550 °C, 1650 °C, and 1750 °C for 30 min in Ar.

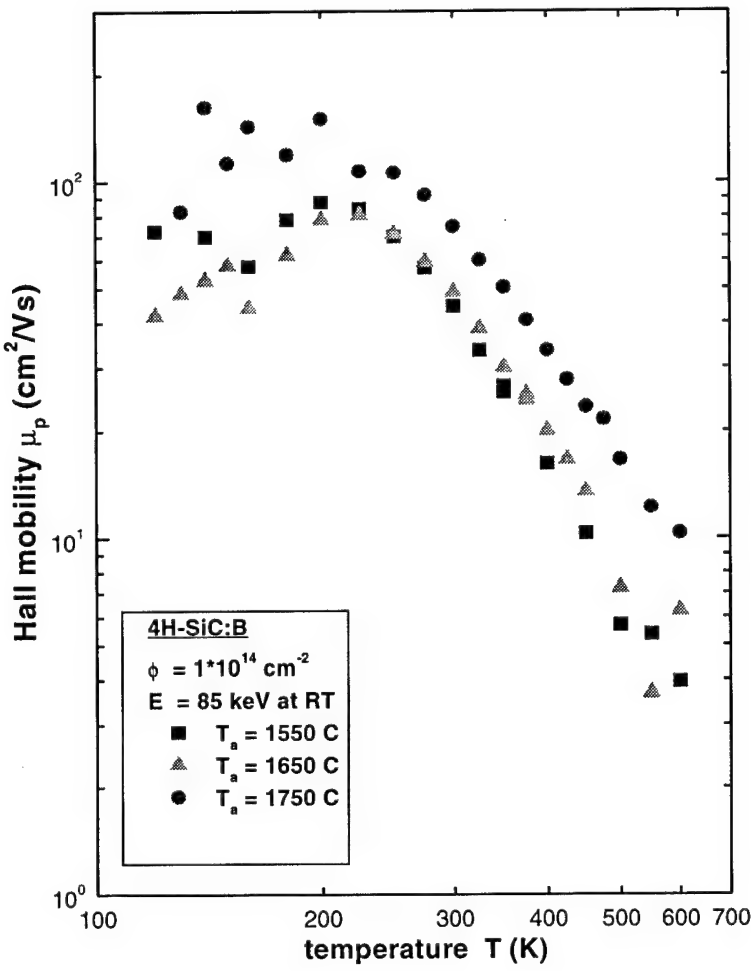

Figure IX-7. Hall mobility measurements on B implanted 4H-SiC samples at room temperature with 1x10^{14} cm^{-2} and annealed at 1550 °C, 1650 °C, and 1750 °C for 30 min in Ar.

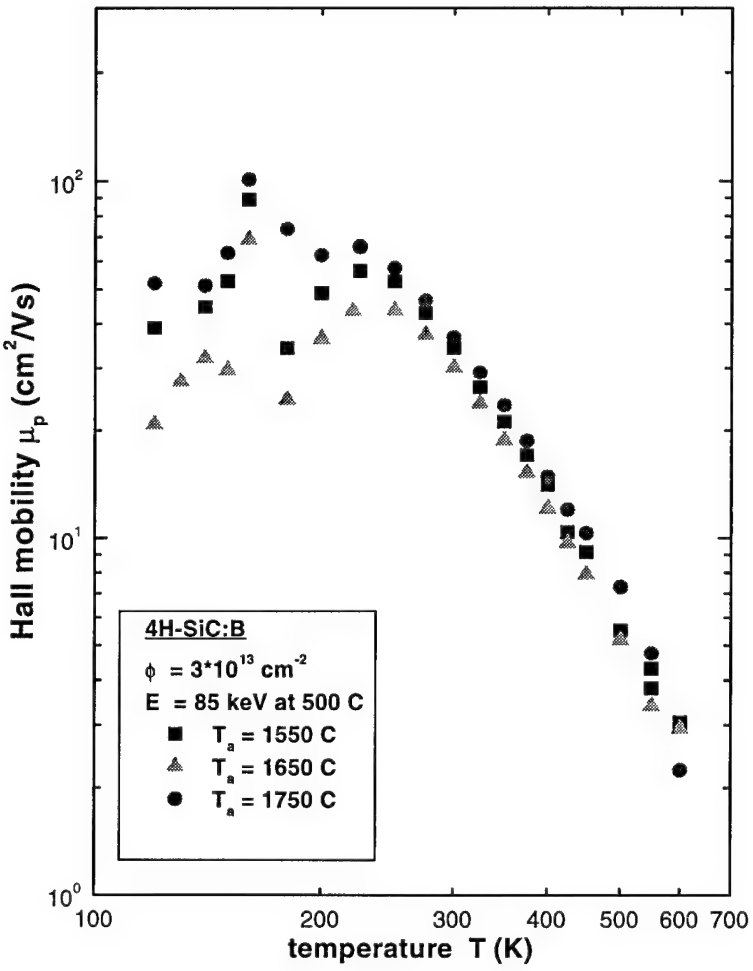

Figure IX-8. Hall mobility measurements on B implanted 4H-SiC samples at high temperature (500°C) with 3x10^{13} cm^{-2} and annealed at 1550 °C, 1650 °C, and 1750 °C for 30 min in Ar.

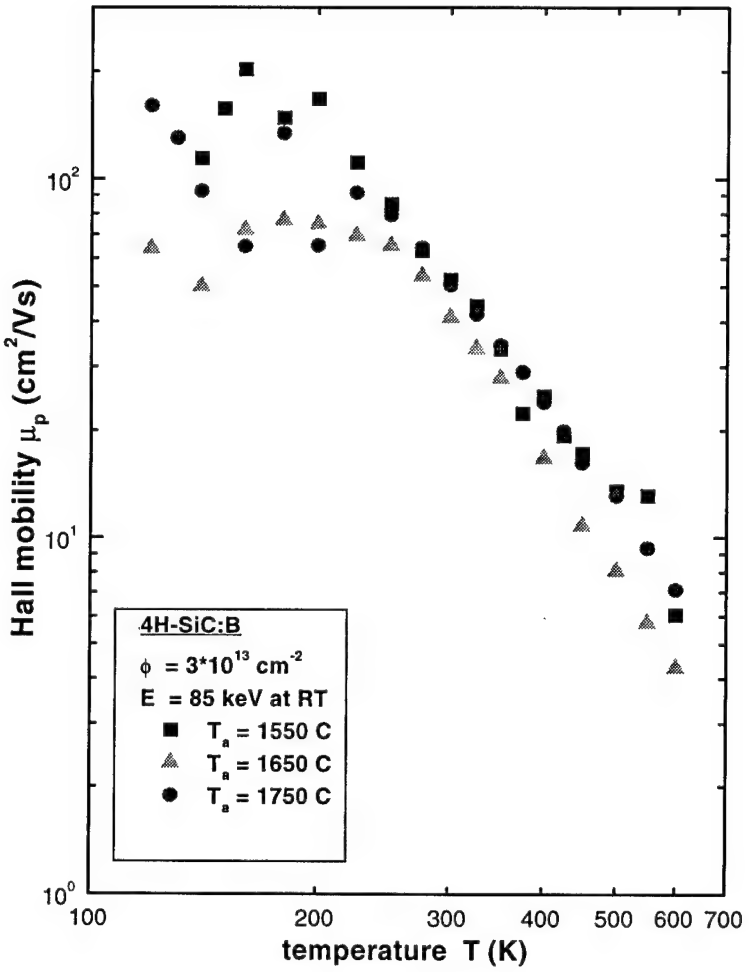

Figure IX-9. Hall mobility measurements on B implanted 4H-SiC samples at room temperature with $3x10^{13}$ cm^{-2} and annealed at 1550 °C, 1650 °C, and 1750 °C for 30 min in Ar.

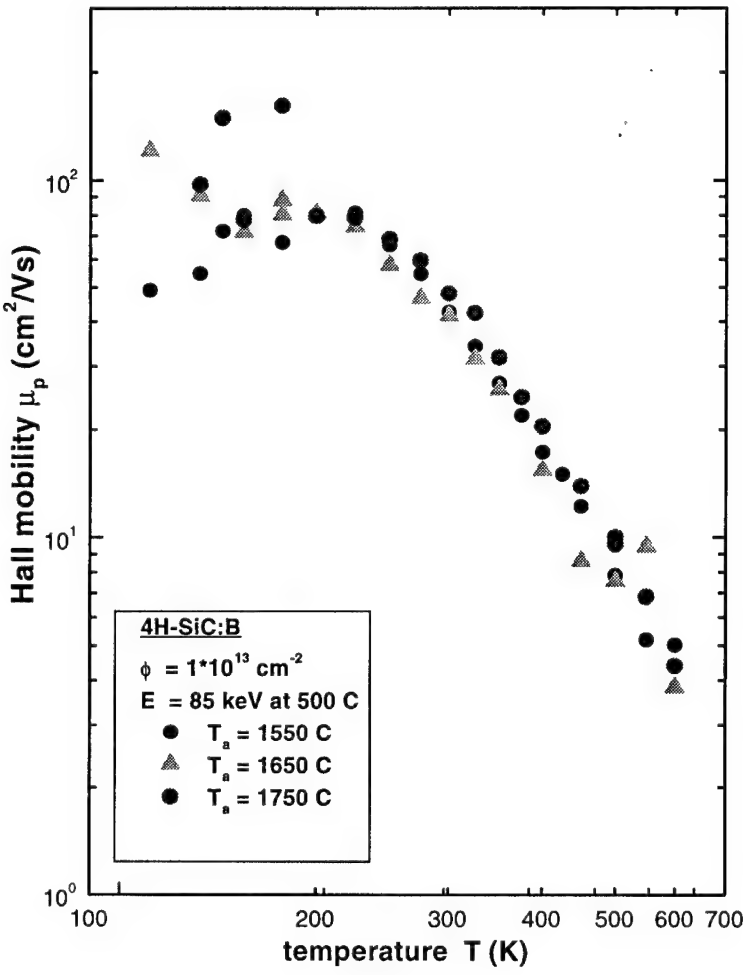

Figure IX-10. Hall mobility measurements on B implanted 4H-SiC samples at high temperature (500°C) with 1x10^{13} cm^{-2} and annealed at 1550 °C, 1650 °C, and 1750 °C for 30 min in Ar.

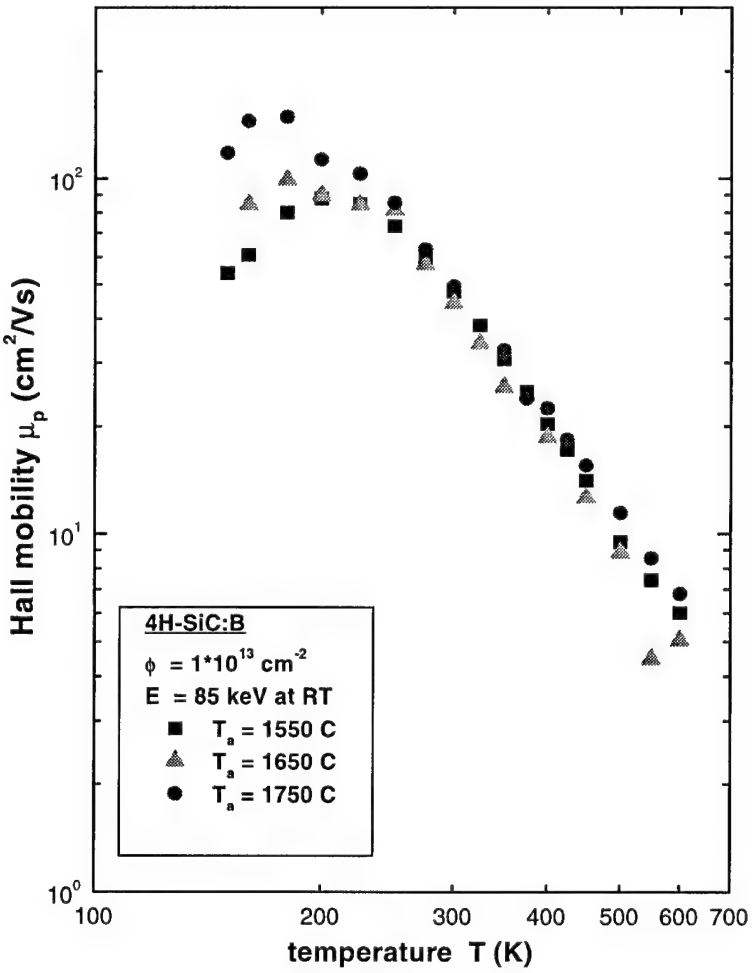

Figure IX-11. Hall mobility measurements on B implanted 4H-SiC samples at room temperature with 1x10^{13} cm^{-2} and annealed at 1550 °C, 1650 °C, and 1750 °C for 30 min in Ar.

Vita

Christian Paul Morath was born on 18 May 1975 in Englewood, NJ. He was the middle child in a family of three boys and two committed parents. His family resided in Wyckoff, NJ his entire adolescent life. He graduated from Ramapo Regional High School on 26 Jun 1993, which left him approximately 4 days to prepare himself before leaving for the US Air Force Academy in Colorado Springs, CO. He graduated from the Air Force Academy in June 1997 with Bachelor of Science in Physics and after receiving a reserve commission in the USAF was assigned to the Air Force Institute of Technology Graduate School of Engineering to work towards a Masters of Science in Engineering Physics. As of writing this, he does not know exactly what he will be doing upon graduation, but hopefully it will be some inspiring research in a part of the country that receives large snowfalls in the winter time.

Christian fondest memories are of his time at the Academy and in Colorado. The Academy taught him to motivate himself to work hard and Colorado gave him a taste for the deep and dry snow of the Rocky Mountains. Some of his favorite memories are the wild times that were shared with friends ripping up the bowls at Vail. In Colorado, he was also fortunate to meet a beautiful, young lady named Stephanie, who was attending The Colorado College. They are still seeing each other, and he hopes to continue that for a long time.

Permanent Address: 7003 N Milliron Rd
Cheyenne WY 82009

Bibliography

1. Faraday, M. *Experimental Researches in Electricity Vol. I.* London: Bernard Quaritch, 1839.

2. Braun F., "Uber die Stromleitung durch Schwefelmetalle," *Ann. Physik. Chem. 153*(4):556 (1874).

3. Schuster A., "On unilateral conductivity," *Phil. Mag. 48*: 251 (1874).

4. Bardeen, J. and W. Brattain. "The transistor: a semiconductor triode," *Phys. Rev., 74*:230 (1948).

5. Brattain, W. and J. Bardeen. "The nature of the forward current in germanimum point contacts," *Phys. Rev.,* 74:232 (1948).

6. Shockley,W. and G. Pearson. "Modulation of conductance of thin films of semiconductors by surface charges," *Phys. Rev., 74*:233 (1948).

7. Wilson A.H., *Proc. Roy. Soc. A 133*:458 (1931).

8 . Acheson, E., "On carborundum," *Chem. News 68*:179 (1893).

9. Melloch, M. and J. Cooper, "Fundamentals of SiC-based device processing," *MRS Bulletin.*:42 (March 1997).

10. Casady, J.B. and R.W. Johnson., "Status of silicon carbide (SiC) as a wide-bandgap semiconductor for high temperature applications: a review," *Soldid-State Elec. 39(10)*:1409 (February 1996).

11. Thome, F. and D. King. "High temperature electronics survey," Internal Memo, Sandia National Laboratory, Albuquerque, NM 1998.

12. Neudeck, P.G. and C. Fazi. "High-field fast-risetime pulse failures in 4H- and 6H-SiC pn junction diodes," preprint of accepted article, *J. Appl. Phys.* (tbp July 1996).

13. Trew, R.J., Yan, J-B. and Mock, *P.M. Proc.IEEE 79(5)*:598 (1991).

14. Reinhardt, K.C, Scofield, J.D. and Mitchell, W., "Directions in Air Force high temperature power electronics," Unpublished Report, Propulsion and Power Directorate, Wright Laboratory, Wright-Patterson AFB OH, 1995.

15. Eike, D. et al. "Advanced secondary power system study," Final report, USAF Contract F33657-84-C-0247, CDRL 3402, 1992, General Dynamics, Forth Worth Division, 76101.

16. Shah, N. and K. Rohr. "More electric F-18 cost benefits study," WL-TR-91-2093, 1992, Northrop Corporation, Aircraft Division, 90250.

17. Scofield, J. D. *Electrical Characterization of Intrinsic and Induced Deep Level Defects in Hexagonal SiC*. Ph.D. dissertation. Graduate School of Engineering, AFIT (AU), Wright-Patterson AFB OH, November 1996.

18. McKelvey, J.P. *Solid State Physics for Engineering and Materials Science*. Florida: Krieger Publishing Company, 1993.

19. Wellenoffer, G. and U. Rossler. "Global band structure and near-band-edge states." *Phys. Stat. Sol. (b), 202*:107-123 (January 1997).

20. Ashcroft, Neil W. and N. David Mermin. *Solid State Physics*. Philadelphia: Saunders College, 1976.

21. Look, David C. *Electrical Characterization of GaAs Materials and Devices*. New York: John Wiley & Sons, 1989.

22. Morokoc, H. et. al. "Large-band-gap SiC, III-V nitride, and II-VI Zn-Se-based semiconductor device technologies," *J. Appl. Phys. 76(3)*:1365 (August1994).

23. Choyke, W.J. and G. Pensl. "Physical properties of SiC," *MRS Bulletin*:25 (March 1997).

24. Ramsdell, L. "Studies on silicon carbide," *Am. Mineralogist 32*:64 (1947).

25. Elsaesser, D. W. *Excitation and De-excitation mechanisms of Er-doped GaAs and AlGaAs*. Ph.D. dissertation. Graduate School of Engineering, AFIT (AU), Wright-Patterson AFB OH, December 1992.

26. Glass, R.C. et al. "SiC-Seeded Crystal Growth," *MRS Bulletin*:30 (March 1997).

27. Neudeck, P.G. and J.A. Powell., "Performance limiting micropipe defects in SiC wafers," *IEEE Electron Dev. Lett. 15*:2 (February 1994).

28 . Crofton, J. et al. "The physics of ohmic contacts to SiC," *Phys. Stat. Sol. (b) 202*:581 – 603 (1997).

29. Bozack, M.J. "Surface studies on SiC as Related to Contacts," *Phys. Stat. Sol. (b) 202*:549 – 580 (1997).

30. Spiess, L. et al. "Aluminum implantation of p-SiC for ohmic contacts," *Diamond and Related Materials 6*:1414-1419 (1997).

31. Kimoto, T. et al. "Conductivity control of SiC by in-situ doping and ion implantation," *Materials Science Forum Vols. 264-268*:675-680 (1998)

32. Seshadri, S., Eldridge, G.W., and A.K. Agarwal. "Comparison of the annealing behavior of high-dose nitrogen-, aluminum-, and boron-implanted 4H-SiC," *Appl. Phys. Let. 72(16)*:2026-2028 (April 1998).

33. Troffer, T. et. al. "Doping of SiC by Implantation of Boron and Aluminum," *Phys. Stat. Sol. (a) 162*:277-298 (1997).

34. Rao, M.V. et al., *J. Appl. Phys. 77*: 2479 (1995).

35. Pensl, G. and W. J. Choyke. "Electrical and optical characterization of SiC," *Physica B 185*:264-283 (1993).

36. Williams, J.M., McHargue, C.J. and B. R. Appleton., *Nucl. Instrum. Methods. Phys. Res. 209-210*:317 (1983).

37. Violin, E.E. "Restoration of the structure of silicon carbide layers after ion implantation," *Sov. Phys. Solid State 26(5)*: 960-961 (May 1984).

38. Ryu, J.S. et al. *Proc. Mat. Res. Soc. Symp. 52*:233 (1986).

39. Scott, M.B., Yeo, Y.K, and R.L. Hengehold. "High temperature (500°C) implantation study of P and N implanted epitaxial n-type 4H-SiC," to be published in the proceedings of the ISCS 98 Conference.

40. Lang, J.E. and P.N. Hemenger. *Computer-assisted Analysis of Electronic Transport Data*. AFWAL-TR-85-4101. Materials Laboratory. AF Wright Aeronautical Laboratories. (August 1985).

41. Schroder, D.K. *Semiconductor Material and Device Characterization*. New York: John Wiley and Sons, 1990.

42. Porter, L. M. and R. F. Davis. "Critical review of ohmic and rectifying contacts for silicon carbide," *Mat. Sci. & Eng. B:Sol. Stat. Mat. for Adv. Tech. B34(2-3)*:83-105 (Nov 1995).

43. Lundberg, N. and M. Ostling. "Thermally stable low ohmic contacts to p-type 6H-SiC using cobalt silicides," *Solid-State Electronics 39(11)*:1559-1565 (1996).

44. Casey, H.C. "Variation of electrical properties with Zn concentration in GaP," *J. Appl. Phys. 40(7)*: 2945-2957 (June 1969) .

45. Schoner, A., Rottner, K., and N. Nordell, Mat. *Res. Soc. Symp. Proc. 423*:661 (1996).

REPORT DOCUMENTATION PAGE	Form Approved OMB No. 0704-0188

1. AGENCY USE ONLY *(Leave blank)*	2. REPORT DATE	3. REPORT TYPE AND DATES COVERED
	March 1999	Master's Thesis

4. TITLE AND SUBTITLE
ELECTRICAL CHARACTERIZATION OF ION-IMPLANTED 4H-SILICON CARBIDE

5. FUNDING NUMBERS

6. AUTHOR(S)
CHRISTIAN P. MORATH

7. PERFORMING ORGANIZATION NAME(S) AND ADDRESS(ES)
AIR FORCE INSTITUTE OF TECHNOLOGY
2950 P STREET
WPAFB OH 45433-7765

8. PERFORMING ORGANIZATION REPORT NUMBER
AFIT/GAP/ENP/99M-05

9. SPONSORING/MONITORING AGENCY NAME(S) AND ADDRESS(ES)
Dr. William Mitchel
AFRL/MLPO, Building 651
3005 P Street, Suite 6
Wright-Patterson AFB, OH 45433-7707

10. SPONSORING/MONITORING AGENCY REPORT NUMBER

11. SUPPLEMENTARY NOTES
Yunk K. Yeo, Professor of Engineering Physics, ENP

12a. DISTRIBUTION AVAILABILITY STATEMENT
Approved for public release; distribution unlimited.

12b. DISTRIBUTION CODE

13. ABSTRACT *(Maximum 200 words)*
Electrical characterization has been performed on ion-implanted p-type 4H-SiC to assess the activation efficiency and implantation-related damage recrystallization with the intention of developing an implantation/annealing scheme. Low doped (Na - Nd = 5x10^15 cm^-3) epitaxial p-type layers grown by MOCVD were implanted with Al or B at doses ranging from 1x10^13 to 1x10^14 cm^-2 at room temperature or 500 deg. C. The electrical technique of Temperature Dependent Hall Effect (TDHE) indicated that Al and B act as shallow acceptors in 4H-SiC with ionization energies of ~252 and ~285 meV, respectively The highest activation efficiency for Al and B implanted samples was found to occur at anneal temperatures of ~1650 deg. C and ~1550 deg. C, respectively. The implantation dose resulting in the highest concentration for Al and B implantation was found to be 3x10^13 cm^-2. An average peak mobility of ~200 cm^2 / V s was found for an Al implanted sample; this is considerably higher than the average peak mobility for the B implanted samples, ~100 cm^2/ V s. No significant gains in activation efficiency or mobility were evident with high temperature implantation compared to the room temperature implantation. Overall, Al implantation of 4H-SiC appears superior with regard to these properties compared to B implantation.

14. SUBJECT TERMS	15. NUMBER OF PAGES
Silicon Carbide, Ion-Implantation, Temperature Dependent Hall Effect, Thermal Annealing, 4H-SiC, Ohmic Contacts	165
	16. PRICE CODE

17. SECURITY CLASSIFICATION OF REPORT	18. SECURITY CLASSIFICATION OF THIS PAGE	19. SECURITY CLASSIFICATION OF ABSTRACT	20. LIMITATION OF ABSTRACT
UNCLASSIFIED	UNCLASSIFIED	UNCLASSIFIED	UL

Standard Form 298 (Rev. 2-89) (EG)
Prescribed by ANSI Std. 239.18
Designed using Perform Pro, WHS/DIOR, Oct 94